MOLTEN MICRODROP
DEPOSITION AND SOLIDIFICATION PROCESSES

by

FUQUAN GAO

B.S. Eng., Shanghai Jiao Tong University, 1982
M.S. Eng., Shanghai Jiao Tong University, 1984

M.S.M.E., Massachusetts Institute of Technology, 1990

Submitted to the Department of Mechanical Engineering
in Partial Fulfillment of the Requirements
for the Degree of

Doctor of Philosophy
in Mechanical Engineering

at the

MASSACHUSETTS INSTITUTE OF TECHNOLOGY

May 1994

Signature of Author ______________________________
Department of Mechanical Engineering

Certified by ______________________
Ain A. Sonin
Professor, Mechanical Engineering
Thesis Supervisor

Accepted by ______________________________
Ain A. Sonin
Chairman, Departmental Committee on Graduate Studies
Department of Mechanical Engineering

MOLTEN MICRODROP
DEPOSITION AND SOLIDIFICATION PROCESSES

by

FUQUAN GAO

Submitted to the Department of Mechanical Engineering
on May 16, 1994 in partial fulfillment of the
requirements for the Degree of Doctor of Philosophy in
Mechanical Engineering

ABSTRACT

Objects may be fabricated by precisely controlled deposition and solidification of molten microdrops. This provides a means of "digital microfabrication," that is, fabrication of objects microdrop by microdrop under complete computer control. To understand the physical phenomena associated with basic deposition modes, extensive experiments have been carried out with a drop-on-demand droplet generator (deposition frequencies ranging from 0 to 15 kHz). The conditions required for controlled deposition and solidification are discussed, and experimental results and theoretical analyses are given for the basic deposition modes which include dropwise (low frequency) columnar deposition, continuous (high frequency) columnar deposition, sweep deposition of continuous beads on flat surfaces, and repeated sweep deposition. The experiments were done with molten wax droplets (50 μm in diameter), but the analysis provides a means of generalizing the results to other materials (e.g. metals) and to droplets of different size. An important parameter in modeling microscale melt deposition is the solidification angle which determines the shapes formed. It is found that under certain conditions this angle appears to be a property of the melt material, the target material, and the characteristic temperatures involved, but independent of the spreading process.

Thesis Supervisor: Dr. Ain A. Sonin

Title: Professor of Mechanical Engineering

ACKNOWLEDGMENTS

I would like to express my deepest thanks to my thesis supervisor, Professor Ain A Sonin, for his expert guidance, his keen intellectual insight, and his availability and steady support. It has been a challenge, a unique learning experience, and a great pleasure to work with him. Without his help and guidance I would never have been able to complete this work. This thesis draws heavily from the paper co-authored with him, "Precise Deposition of Molten Microdrops: the Physics of Digital Microfabrication" (*Proc. R. Soc. Lond.* A (1994) **444**, 533-554) and Chapter 4 is a part of the paper. I am also very grateful for his help, personal advice, and concern throughout my studies at MIT.

I thank my thesis committee, Professors Ronald F. Probstein, Jung-Hoon Chun, and Thomas W. Eagar, for their valuable suggestions. I would also like to thank Professors Sonin and Probstein for their great lectures on fluid mechanics from which I benefited greatly.

I am very grateful to Dr. Ge Yao Chu and the Chu Fellowship Committee at MIT for offering me a Chu Fellowship during my first three years at MIT. The annual gatherings of the Chu fellows were very enjoyable, and I am extremely appreciative of Dr. and Mrs. Chu's hospitality and kindness.

I would like to thank Leslie Regan for her help and friendliness. She has an amazing ability to get things accomplished at MIT.

I would like to thank Gregg Duthaler and Stefano Schiaffino for their help and friendship. I have enjoyed sharing the research area and discussing challenging issues with them. I appreciate Stefano Schiaffino's help in proofreading the manuscript.

I thank Claire Sasahara and Dick Fenner for their help. I would also like to thank the members of the Fluid Mechanics Laboratory who made my time there very pleasant: Dave Otis, Frank Espinosa, Mariano Gurfinkel, Edwin Ozawa, Steve Brown, Athur Sit, Chunhai Wang, Chris Atkinson, Jian Shen, James Shin, Naomi Chesler, Manuel Cruz, Barbara Hamer, and Serhat Yesilyurt.

I would like to thank my friends outside the lab for all of their help.

I would like to thank Professor Hongzhong Gu, who supervised my Master's Thesis at Shanghai Jiao Tong University, for his encouragement. Without his help I would not have been able to attend MIT.

I would like to thank my sisters and brother for their encouragement, love, and support.

I would like to thank my wife, Hong, and my daughter, Jia Jia, for their support, patience, and love.

This work was supported by the National Science Foundation under Grant -9122123, and initiated with the aid of grants from the Charles E. Reed Faculty Initiative Fund and Hewlett-Packard Company.

TABLE OF CONTENTS

Appendixes

LIST OF FIGURES

LIST OF TABLES

Chapter 1

INTRODUCTION

1.1 Background

It is well known that the key to competitiveness in manufacturing lies in cutting product development cycles. The time to develop new products depends strongly on the time required to fabricate prototypes. Many researchers and manufacturers are working on various methods of rapid prototyping to accelerate product development (e.g. see Ashley 1991; Aronson 1993; Marcus *et al.* 1993). The method of dropwise melt deposition is based on an idea derived from ink-jet printing technology. Instead of dropwise deposition of liquid ink on paper, however, the idea is to generate and deposit molten microdrops on a target where they solidify. Thus, arbitrary 3D objects can be fabricated by precise dropwise deposition of melts under complete computer control similar to 2D hard copy printing.

Figure 1.1 illustrates this dropwise melt deposition process. The droplet generator is a drop-on-demand system. When a voltage pulse is applied to the generator, it generates a single molten droplet. (More about the droplet generator will be given in Section 2.3.) The droplets lose heat during flight and after impact on the target, where they solidify. If the

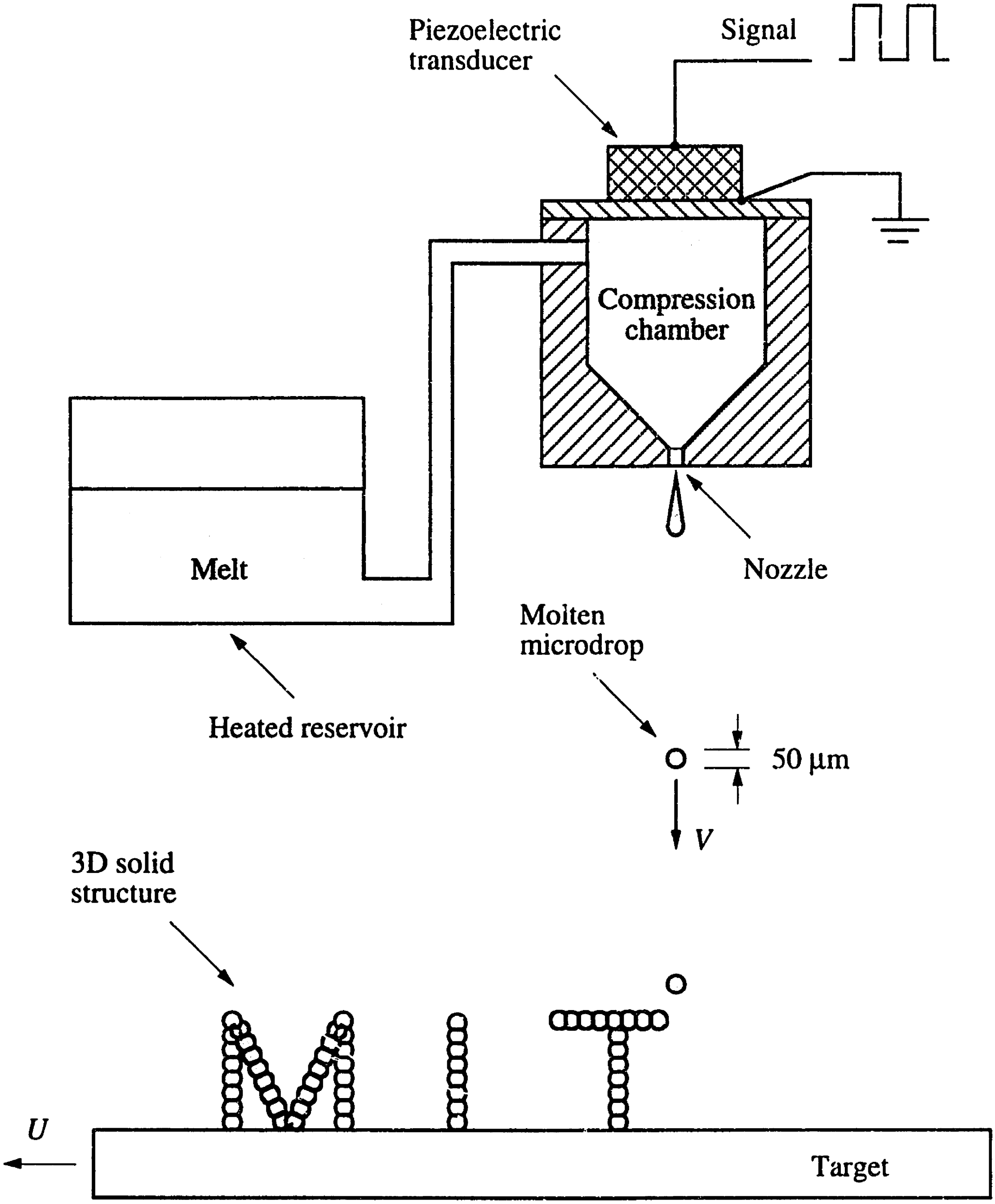

Figure 1.1. Molten microdrop deposition process.

droplet generator can be moved relative to the target under computer control, objects of almost arbitrary shapes can, in principle, be built.

Figures 1.2 and 1.3 give some examples of solid structures formed by precise dropwise deposition. In Figure 1.2, the letters "MIT" are about 300 µm tall and stand upright from a plastic surface. They are fabricated by precise deposition of molten wax droplets from above at low frequency, each droplet solidifying by heat transfer to the ambient air before the next one arrives. In Figure 1.3, the structure is composed of three elements: a sphere, a pillar, and a hemisphere. Each element is composed of 20 individual droplets, but created by dropwise deposition at different frequencies. At sufficiently high frequency, there is not enough time between droplets for solidification, so the 20 droplets

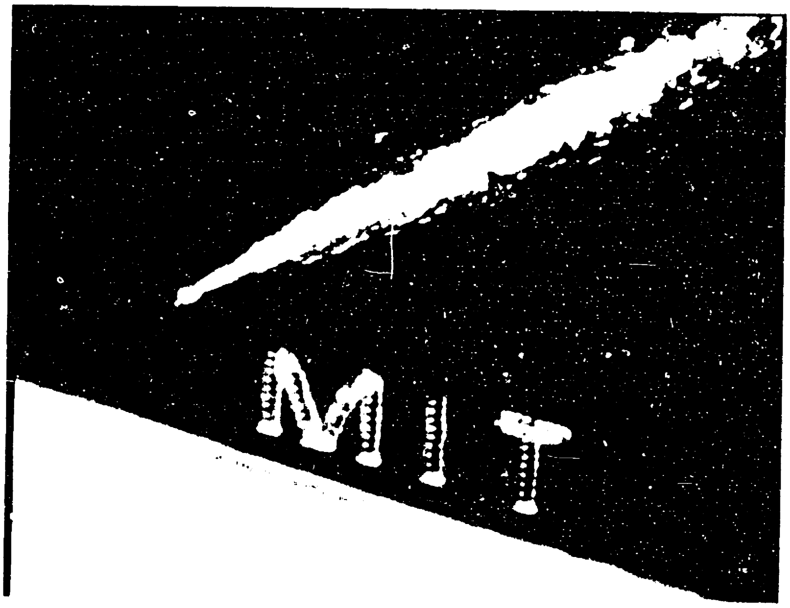

Figure 1.2. 300 µm tall letters produced by dropwise deposition of molten wax microdrops. The conical object is the tip of a common pin; the rectangle measures 200 µm x 600 µm.

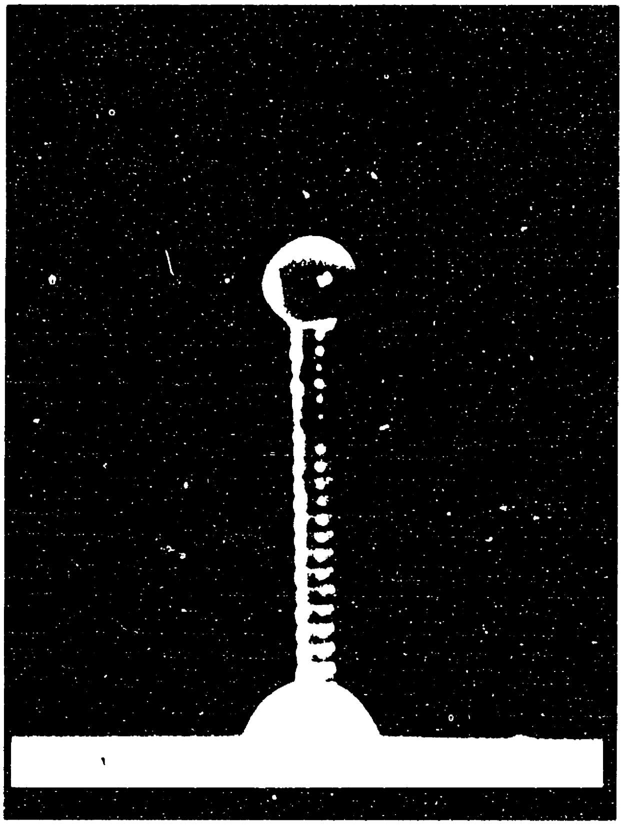

Figure 1.3. Structure formed by depositing molten wax microdrops at different frequencies. The rectangle measures 100 μm x 300 μm.

coalesce into a liquid sphere at the tip of the pillar or a spherical-cap liquid drop on the target (surface tension dominates at these scales). At low frequency, the previous droplet has solidified before the next one lands, so a vertical pillar of solidified droplets is formed.

When a molten microdrop is deposited on a subcooled solid surface, it spreads at first like a liquid drop, then its moving contact line freezes or stops moving as it reaches a mechanical equilibrium state, and finally the whole droplet solidifies due to heat transfer from the melt to the solid substrate as well as the ambient air. We know that the spreading process of a single liquid drop on a solid surface is complicated (e.g. see Hoffman 1975;

Tanner 1979; Dussan 1979; de Gennes 1985 and 1990; de Gennes *et al.* 1990; Adamson 1990; Hocking 1991). The spreading process of a molten drop is, however, even more complicated since it involves both flow and solidification. Most solidification problems are complex even if no flow is involved or if the flow is simple (e.g. see Crank 1985; Yao & Prusa 1989; Pru'homme *et al.* 1989; Riley *et al.* 1974).

1.2 Potential Applications of Molten Microdrop Deposition

Dropwise melt deposition has a number of potential applications and the following are some of them (Sonin 1991).

Rapid Prototyping and Free-Form Fabrication

As mentioned in the previous section, one of the methods of rapid prototyping is molten microdrop deposition. It may in principle offer significant improvements in rapid prototyping. If objects are built by precise deposition of molten microdrops under complete computer control, it may be possible to improve precision, eliminate material waste, and achieve a completely automated fabrication process. One may envision such systems as the basis for stereoxerography.

Dropwise deposition may also be used for direct free-form fabrication. The key will be whether it can be used with interesting materials.

Electronics Packaging

In electronics manufacturing, the dropwise melt deposition process can in principle be used to directly fabricate electric circuits or components; for example, fine conductors in 3D space or resistors for microdevices might be made with different metal melts.

The molten droplet deposition may also be used for a ballistic delivery of solder in precisely controlled amounts and at precise locations with metered superheat. This will provide a novel method for the surface mount technology which allows very high density circuits. With dropwise deposition technology, the cost and time required to fabricate electronic circuits may be significantly reduced.

Materials Processing

The dropwise deposition is a basic component in several materials processing methods. Both plasma spraying and spray forming, for example, rely on dropwise melt deposition. These processes can be used for laying down protective coatings or for net-shape fabrication. The individual melt droplet impact and solidification processes, which control the metallurgical properties of the deposit, are the same as those in our work. The droplet diameter and impact velocity are of the same order. Thus, an understanding of the physical phenomena associated with our melt droplet deposition and solidification processes can also be applied to the spray processes.

Dropwise melt deposition may also provide a method for growing pure or even single-crystal metal fibers or wires (see the continuous columnar deposition mode described in Section 4.4). Metals like tungsten and molybdenum, for example, are ordinarily produced in polycrystalline form and are brittle at room temperature. In single-crystal form, however, their ductile-brittle transition temperature is well below room temperature, and the material would have high ductility as well as high strength.

1.3 Objectives

In the present work, we focus on the fundamental phenomena and deal with the dynamic and thermal aspects of molten microdrop deposition and solidification processes. The purposes of the present work are to gain a basic understanding of the physical phenomena associated with molten droplet deposition and solidification processes, to identify the conditions required for controlled deposition, to provide theoretical analyses for the basic deposition modes, and to predict the shapes of the formed structures.

As mentioned in Section 1.1, the dropwise melt deposition process is very complicated. Our approach to this complex problem is to break it into its basic, simplified parts and to develop an understanding of each critical subprocess, based on experimental investigation and modeling and analysis.

This thesis draws heavily from the paper, "Precise Deposition of Molten Microdrops: the Physics of Digital Microfabrication" (*Proc. R. Soc. Lond.* A (1994) **444**, 533-554) by Fuquan Gao and Ain A. Sonin and Chapter 4 is a part of the paper.

Chapter 2

EXPERIMENTAL APPARATUS

2.1 Introduction

The experimental apparatus for precise deposition of molten microdrops should meet the following two basic requirements:

(a) the droplet can be generated and delivered to a specified target location under controlled conditions;

(b) the whole deposition process can be visualized and recorded.

To achieve precision, the diameter of molten droplets should be small, thus the nozzle diameter of the droplet generator should also be small. In our experiments, the diameters of droplets and nozzles are about 50 μm. We use the existing ink-jet printing technology, that is, use an adapted ink-jet print head as the droplet generator (see Section 2.3 for more details). Since the droplets are so small, in order to observe and record the deposition process we use a video system which is designed for use with a microscope. In the following, we first describe the whole experimental set-up, then the droplet generator, and finally the melt materials used in our experiments.

2.2 Experimental Apparatus

Figure 2.1 is a schematic diagram of the experimental apparatus used in this study. The individual molten droplets are ejected on demand from the nozzle of the droplet generator and delivered ballistically to a target location, where they impact and solidify. The whole process can be visualized, recorded, and printed out with a microscope-video monitor system. It consists of a micro-tube with objective lenses of different power and a magnification extender (2:1), a CCD video camera, a multifunctional VCR, a monitor, a crosshair generator, and a video copy processor.

The heated droplet generator is an adapted ink-jet print head which is a drop-on-demand system. Each pulse, which is generated by a pulse generator and applied to the transducer of the droplet generator, will produce one droplet. The pulse generator is a Hewlett-Packard Model 214B and its output pulse can be delayed or advanced with respect to the trigger output. With the help of a stroboscope (flash duration ranging from 0.8 μs to 3.0 μs) which is triggered by the trigger output of the pulse generator, flying droplets can be frozen at any position by adjusting the delay. There are two heaters inside the droplet generator and melt temperature is controlled by the power supply.

The crosshair generator is used for the determination of droplet dimensions and is also used for the measurement of droplet velocities. The droplet velocity V at different locations can be determined by changing the delay time between the pulse (connected to the droplet generatcr) and the trigger output (connected to the stroboscope). For example, if the frozen image of the flying droplets on the screen moves a real distance of Δl as the delay time changes Δt, the average velocity within this distance is equal to $\Delta l/\Delta t$.

The target, which was typically made of plexiglas, aluminum, or the same materials as the melts (candelilla wax and microcrystalline wax in this case), can be either stationary

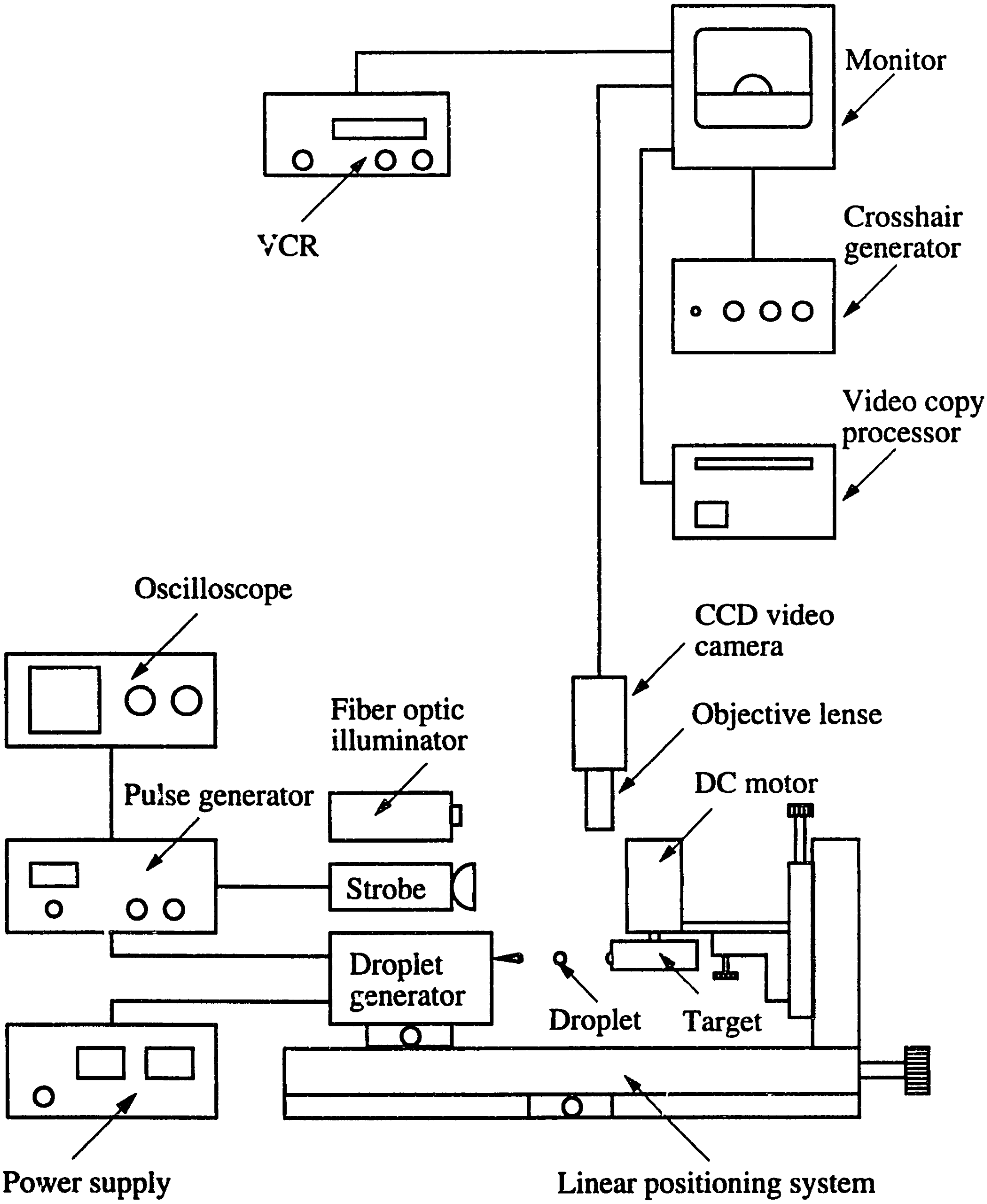

Figure 2.1. Schematic diagram of experimental apparatus.

or moving relative to the nozzle, depending on the purpose of the deposition. In the moving case, the target was a disk which was attached to a small DC motor. The molten droplets were deposited on the outer rim of the disk. Since the diameter of the disk is much larger than that of droplets, the outer surface of the disk can be considered flat. The linear velocity of the target is proportional to the diameter and the angular velocity of the disk. In our experiments, the diameter of the disk was about 45 mm and the angular velocity ranged from less than 1 rpm to about 260 rpm. This wide range of the angular velocity was obtained with several different small DC motors.

The DC motor with the target was attached to a square mount which had two fine-resolution angular adjustment screws. These two adjustment screws allowed the target surface to be tilted precisely relative to the microscope or the droplet generator.

The linear positioning stages had micrometer drives which allowed the droplet generator to be moved relative to the target so that the droplets could be precisely delivered to designated locations. They also allowed both the target and the droplet generator to be moved relative to the microscope. With the micrometer drive and the crosshair, we could also measure the dimension of drops, formed structures, etc.

2.3 Droplet Generator

As mentioned above, the droplet generator was an adapted ink-jet print head in our experiments. There are two main types of systems which are used in ink-jet printing (Heinzl & Hertz 1985): (a) continuous-jet systems; and (b) drop-on-demand (DOD) systems.

In continuous-jet systems, an ink jet emerges continually from a nozzle under high pressure and then disintegrates into a stream of droplets usually by the forced mechanical vibration. (Note that without this mechanical vibration, the ink jet will also break up into a stream of droplets due to the instability of the jet. The purpose of applying the mechanical vibration is to obtain uniform droplets.) The droplets are charged at the moment they are formed. An electric field is then used to separate the charged droplets from the stream and to discard them, while the others (uncharged droplets) are allowed to pass through the electric field undisturbed.

In drop-on-demand systems, individual droplets are ejected at will from a nozzle by pressure pulses in the compression chamber which feeds the nozzle. The droplets then travel to their destination by free flight. After a droplet is ejected, the compression chamber will be refilled with ink by capillary forces. The pressure pulses, which are controlled by the electrical signals, can be generated by two different methods. One is piezo-driven and the other evaporative-bubble driven. In piezo-driven systems, the generation of a pressure wave is achieved by applying a voltage pulse to a piezoelectric transducer. In evaporative-bubble driven systems, the pressure wave is caused by a heat induced evaporative bubble which is generated by applying a voltage pulse to a thermal resistor.

The drop-on-demand systems are inherently *digital*. In this study, the droplet generator is an adapted ink-jet print head which is manufactured by Dataproducts Corporation (see Figure 2.2). It is a piezo-driven drop-on-demand system with 32 nozzles. The nozzle diameters are about 50 μm. Figure 2.3 shows a nozzle piece and one of the nozzles. The principle of the droplet generator is shown in Figure 2.4. The solid materials, waxes in this case, are melted in the reservoir and fed to the compression chamber by capillary forces. When the piezoelectric transducer is given a voltage pulse, it functions like a piston to squeeze a molten droplet out of the nozzle. After the droplet is ejected, the compression chamber is refilled by capillary forces, and the pressure in the compression chamber resumes to slightly below atmospheric pressure, so that a concave meniscus forms in the nozzle.

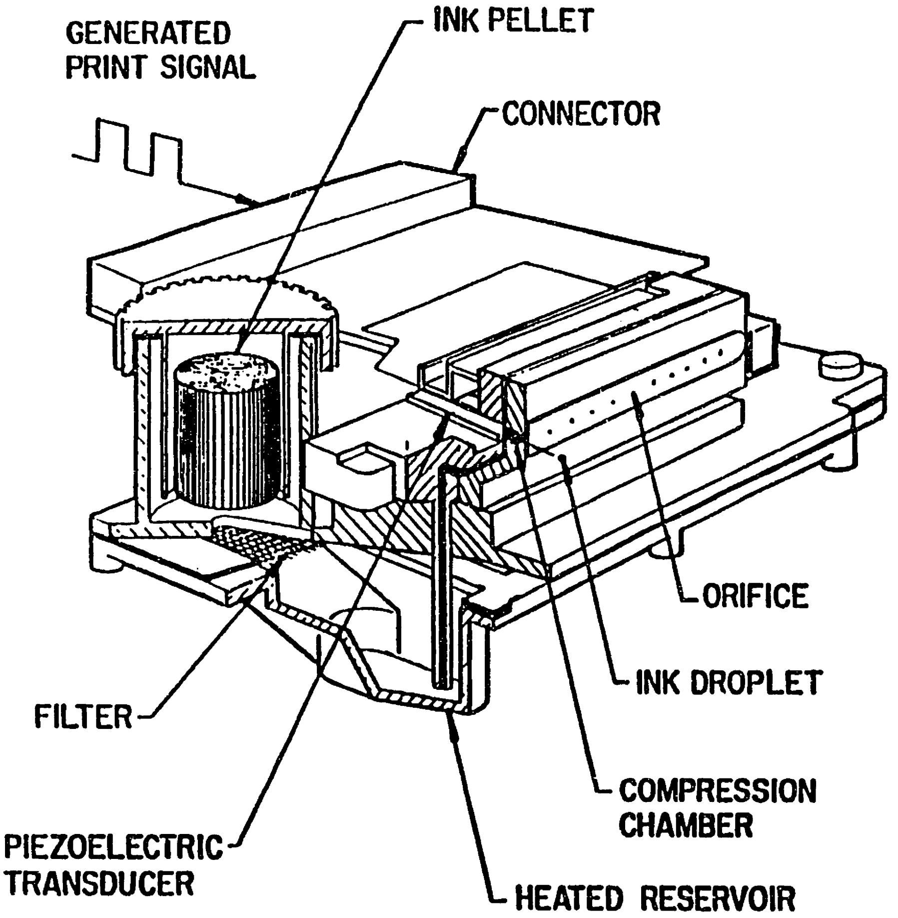

From Lin

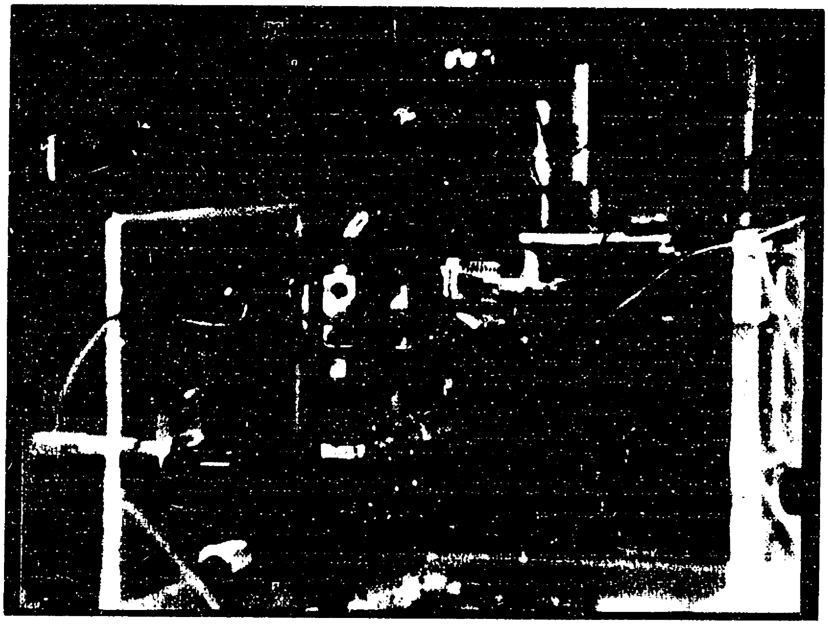

Figure 2.2. Droplet generator.

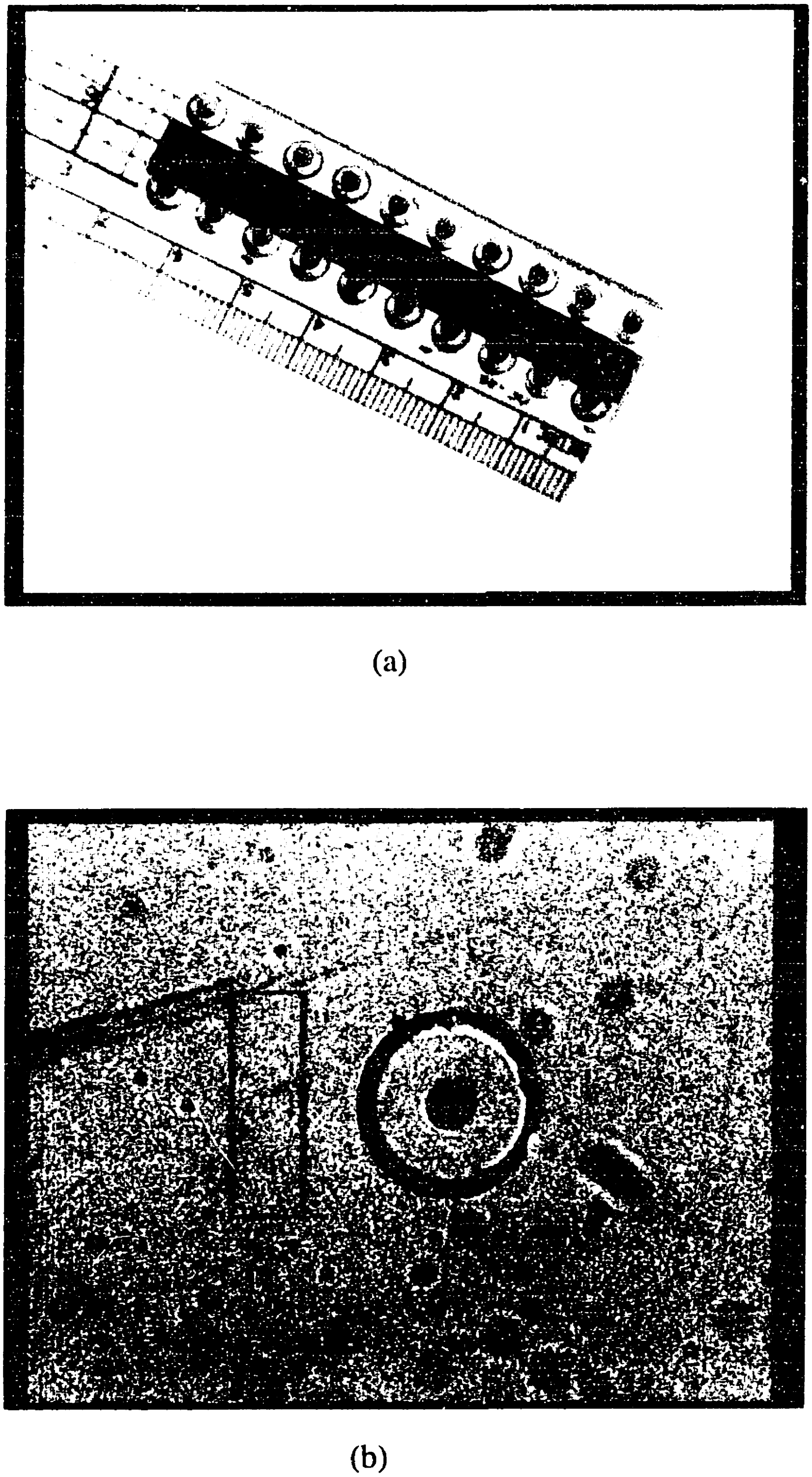

Figure 2.3. (a) Nozzle piece with 32 nozzles. (b) One of the nozzles. Rectangle: 100 μm x 300 μm.

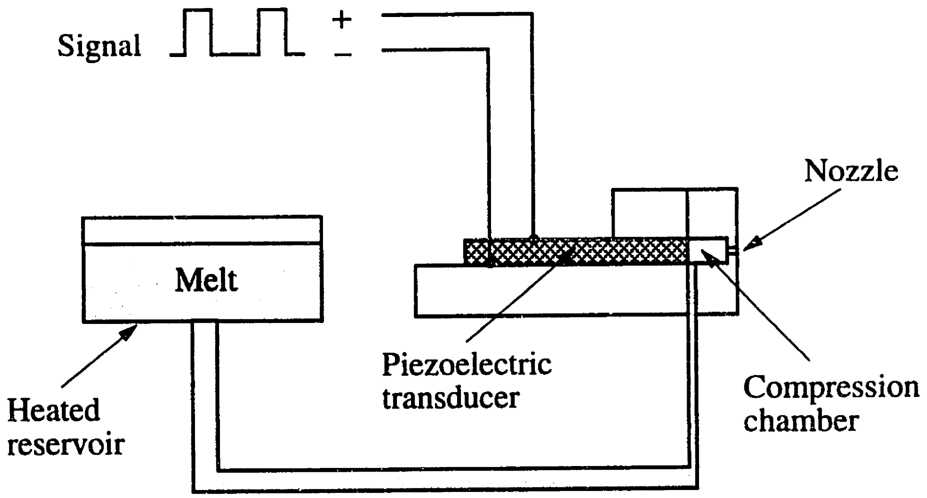

Figure 2.4. Principle of a piezo-driven drop-on-demand system.

2.4 Melt Materials

Two types of waxes were used in our experiments. One was candelilla wax with a melting point of 70°C, and the other was a microcrystalline wax (Reed 6882) with a melting point of 91°C. For purposes of calculations we used the properties listed in Table 2.1. In the analyses it is assumed that the liquid and solid phases of the melt material have approximately the same thermal properties, and that the melt has a single well-defined fusion temperature. The values of the wax properties in Table 2.1 are those of the solid phase and are based on figures provided by several suppliers for the types of waxes we used, as well as on data from Warth (1956). The latent heat of candelilla was taken from Powers *et al.* (1969).

Table 2.1. *Thermal properties*

Substance	T_f ^{o}C	ρ kg m^{-3}	c J kg^{-1} K^{-1}	L J kg^{-1}	k W m^{-1} K^{-1}
Candelilla wax	70	$0.98\text{x}10^3$	$1.7\text{x}10^3$	$1.7\text{x}10^5$	0.17
Microcrystalline wax	91	$0.93\text{x}10^3$	$2.1\text{x}10^3$	$1.5\text{x}10^5$	0.2
Aluminum	659	$2.71\text{x}10^3$	$8.96\text{x}10^2$	$3.96\text{x}10^5$	204
Tin	232	$7.30\text{x}10^3$	$2.27\text{x}10^2$	$6.03\text{x}10^4$	64
Plexiglas	-	$1.19\text{x}10^3$	$1.29\text{x}10^3$	-	0.153
Air	-	1.18	$1.00\text{x}10^3$	-	0.0261

Candelilla wax is a complex mixture and does not have a single well-defined melting point. When a piece of this wax was slowly heated, its surface began to "sweat" at 62^{o}C, and became completely molten at its nominal melting point of 70^{o}C. Figure 2.5 shows the pictures of this process. There were no changes in the surface texture of candelilla wax when the temperature was increased from 26.5^{o}C to 60^{o}C. At 62^{o}C, however, many small liquid spots occurred, they became much larger at 62.5^{o}C, and quickly covered the whole surface.

The surface texture of microcrystalline wax (Reed 6882) was also examined in the same way (see Figure 2.6). There were no changes as the temperature increased from 24^{o}C to 79^{o}C and slight changes at 83^{o}C. The wax began to melt at 88^{o}C and became liquid at 91^{o}C. This wax retained a uniform surface texture as the temperature rose.

The kinematic viscosity of both waxes is about $1.7\text{x}10^{-5}$ m^2 s^{-1} at 100^{o}C (Warth 1956; Reed Wax). The surface tension for both waxes was taken nominally as $\sigma = 0.025$ N m-1. We measured this quantity for candelilla wax using the ring method in a temperature-controlled oven and found σ was 0.0263 N m-1 at 100^{o}C and decreased linearly with temperature to 0.0231 N m-1 at 140^{o}C. The details about the surface tension measurement are given in Appendix A.

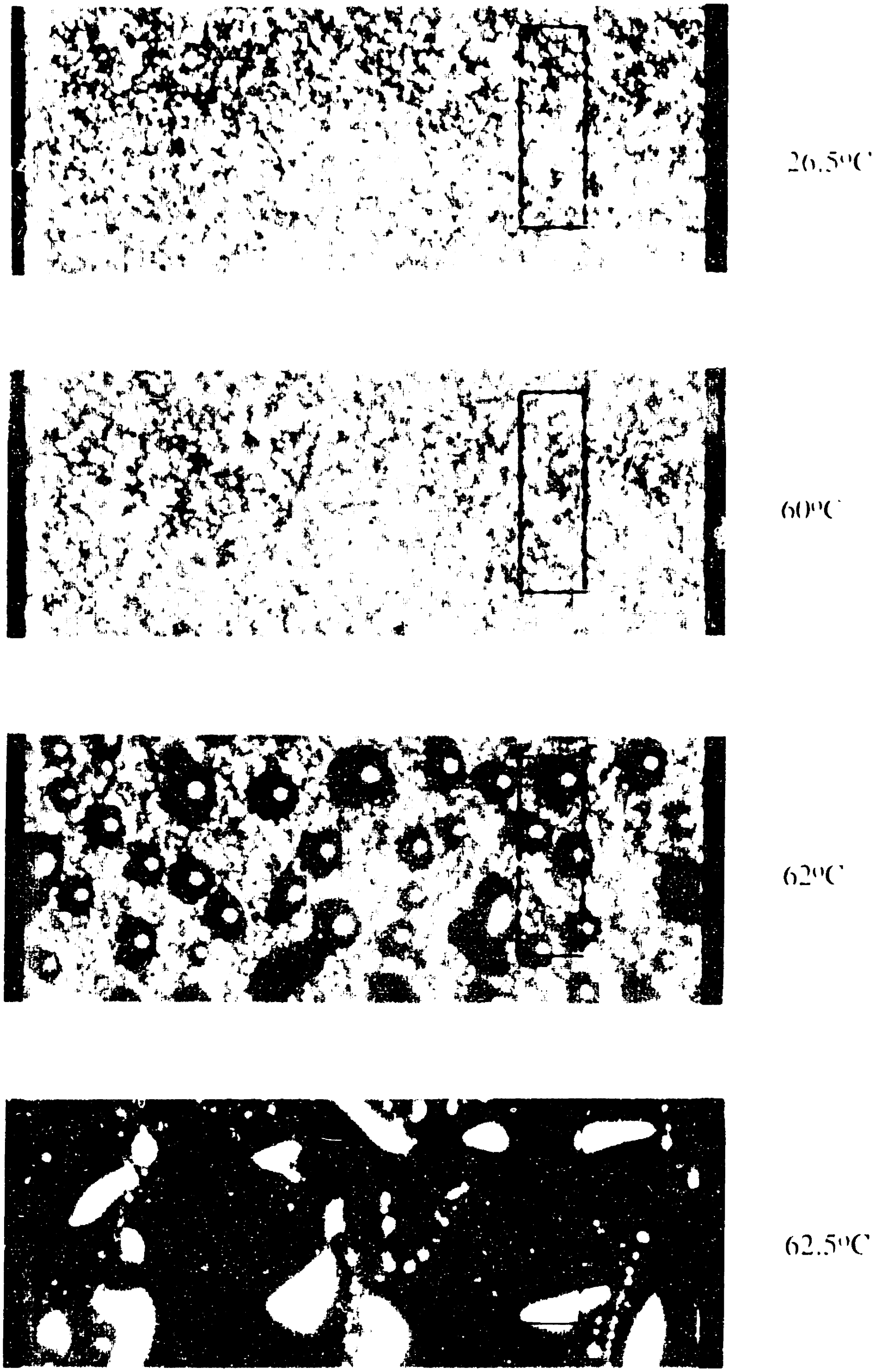

Figure 2.5. Surface texture of candelilla wax at various temperatures. Rectangle: 200 μm x 600 μm.

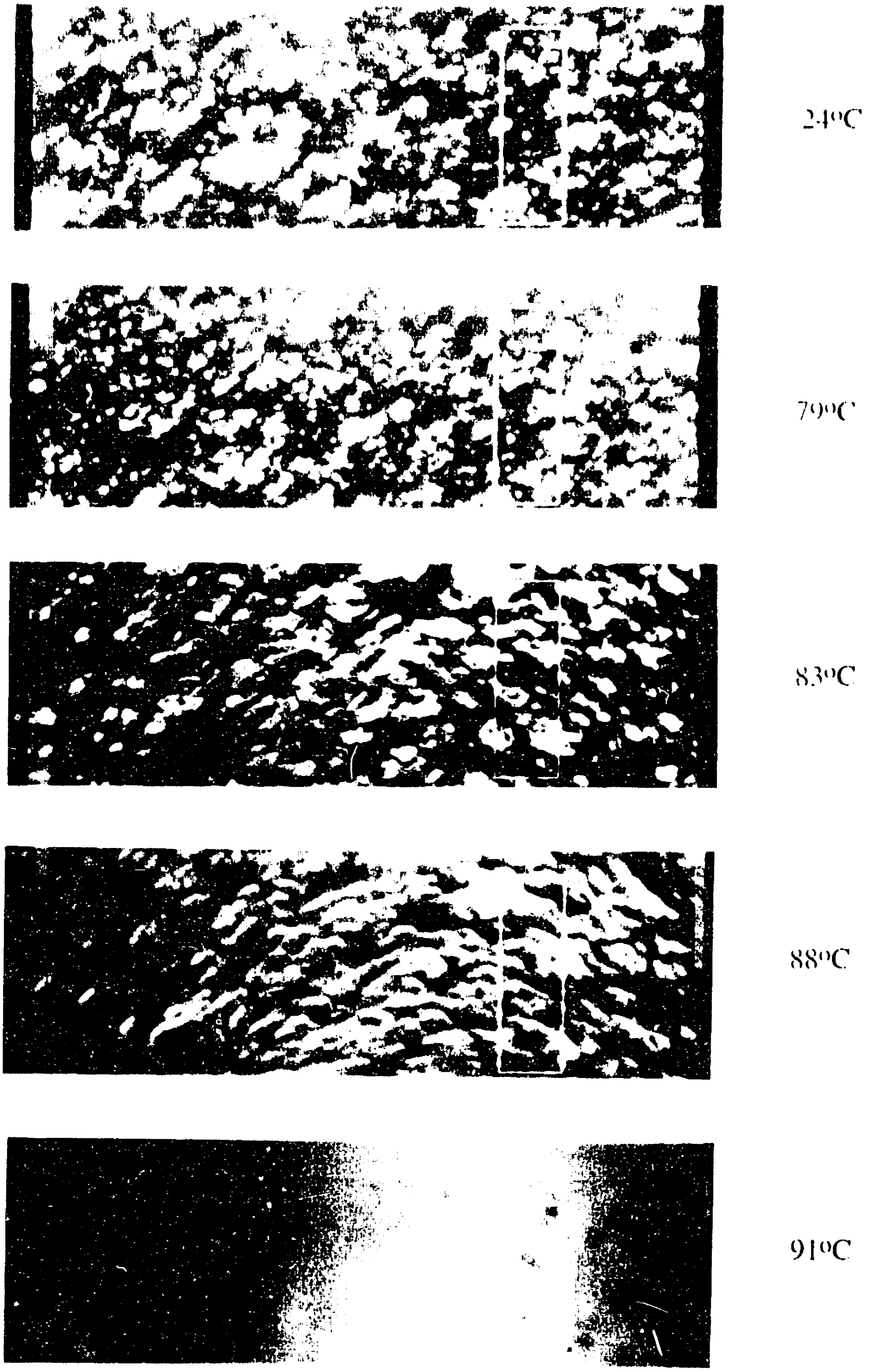

Figure 2.6. Surface texture of microcrystalline wax at various temperatures. Rectangle: 100 μm x 300 μm.

Chapter 3

DROPLETS TRAVELING THROUGH AIR

3.1 Experimental Conditions

We are concerned with systems in which individual molten droplets are dispensed on demand and delivered ballistically to a target location where they impact and solidify. To avoid droplet breakup or splattering, and thus set the stage for precise control over the deposition process, we seek conditions where surface tension forces dominate over inertial effects during impact. This requires that, roughly,

$$We = \frac{\rho V^2 a}{\sigma} < 10, \tag{3.1}$$

where We is the Weber number based on the droplet density ρ, impact speed V, droplet radius a and surface tension σ. However, a droplet will be able to overcome surface tension forces and disengage from the generator nozzle only if the Weber number based on ejection speed is of the order of 10 or larger. Since ballistic accuracy can be maintained only if the droplet does not lose too large a fraction of its speed, this implies that the Weber

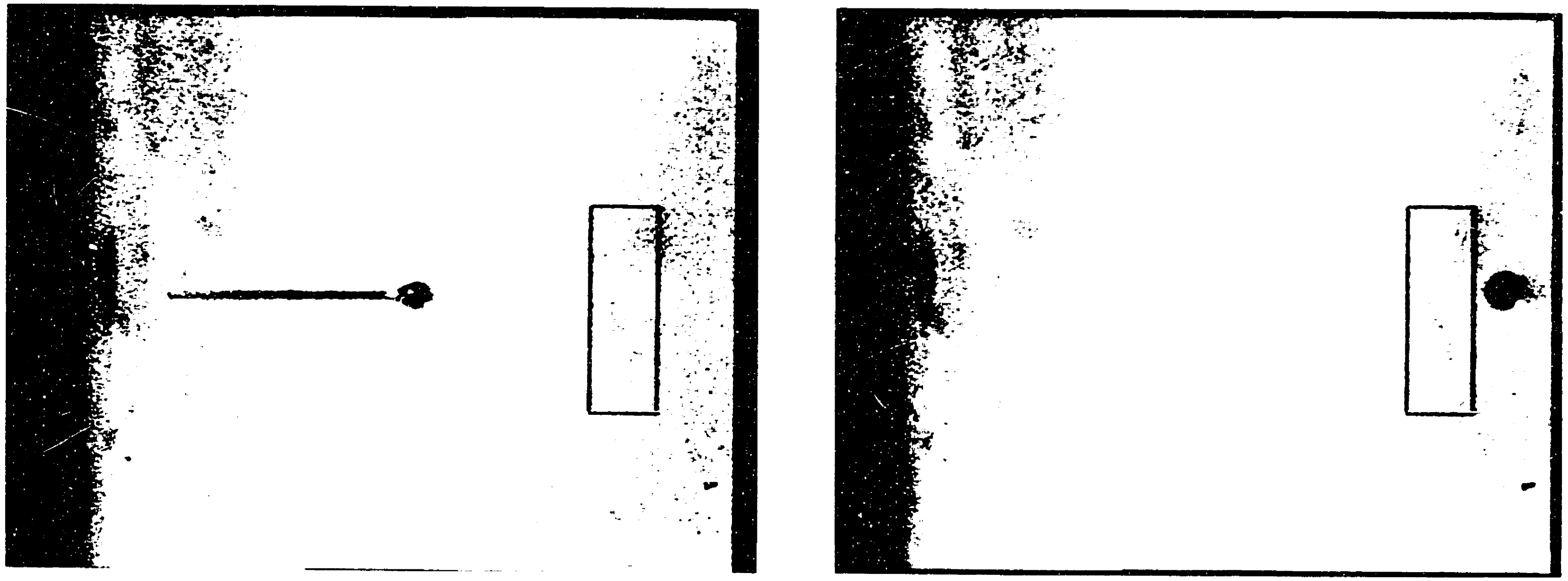

Figure 3.1. A microdrop of molten candelilla wax ejected from a generator nozzle. $T_o = 90^oC$. $f = 1.000$ Hz. Rectangle: 100 μm x 300 μm.

number at impact will typically be in a fairly narrow range, 1-10, say, neither small nor too large.

If the Weber number based on droplet density is in the range 1-10, the Weber number based on *air* density will be very small ($We << 1$), which means that the droplet will assume a spherical shape during flight. The ambient gas was air in all the tests reported here. Figure 3.1 shows a droplet which has just disengaged from a nozzle of the droplet generator and travels through air. As the droplet disengages from the nozzle it has a long tail (Figure 3.1a). The length of the tail decreases as the traveling distance (or time) increases. The tail is completely pulled in the droplet at some distance (about 0.84 mm

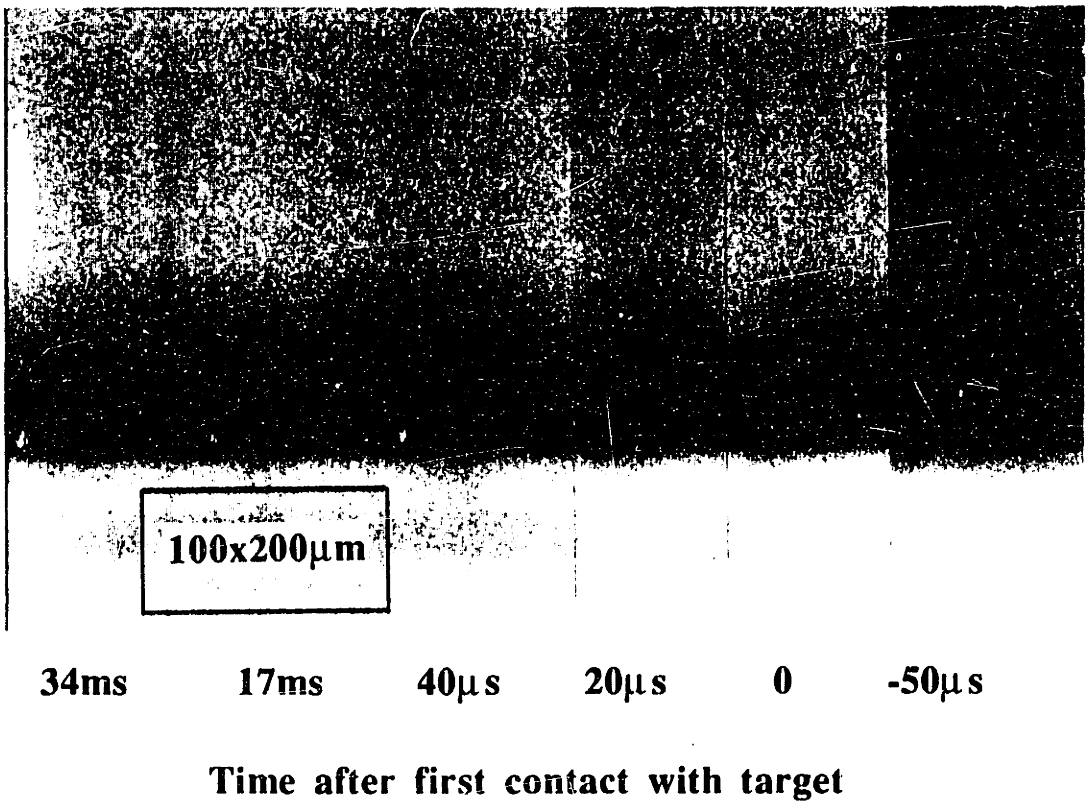

Figure 3.2. Impact of a single microdrop of candelilla wax on a plexiglas target. T_o = 90°C, T_a = 30°C, V = 2.6 m/s.

in this case) due to surface tension and the droplet assumes a spherical shape (Figure 3.1b).

Figure 3.2 shows the impact of a single melt droplet, candelilla wax in this case, on a plexiglas surface. We can see that the droplet has assumed a spherical shape by the time it approaches the target. It only shows slight inertial distortion during impact and quickly assumes a spherical-cap shape under the action of capillary forces. Further discussion about Figure 3.2 will be given in Section 4.1. Figures 3.1 and 3.2 were recorded with the aid of strobe lighting.

3.2 Droplet Deceleration and Stopping Distance

In our experiments individual droplets of molten wax with diameter $2a \approx 50$ μm were ejected at controlled frequencies in the range 0-15 kHz from a heated drop-on-demand generator and directed to a target located typically 2-5 mm away, where they impacted at a speed V of the order of 3 m/s.

The distance between the nozzle of the generator and the target must be significantly smaller than the droplet's stopping distance l_s in the ambient air or other gas to ensure that the droplet's velocity remains sufficiently high to maintain ballistic accuracy. The stopping distance is the distance the droplet travels before it is brought to a halt by viscous drag. It can be estimated by modeling the droplet's in-flight drag coefficient as (Bird *et al.* 1960; Probstein & Fassio 1970)

$$\begin{aligned} C_D &= 24\, Re^{-1} && Re < 1, \\ C_D &= 24\, Re^{-3/5} && 1 < Re < 10^3, \end{aligned} \tag{3.2}$$

where $Re = \rho_g V(2a)/\mu_g$ is the droplet's Reynolds number in the air or other ambient gas through which it travels, ρ_g and μ_g being the gas density and viscosity, respectively. Using this information in a droplet's equation of motion one obtains

$$\begin{aligned} l_s &= \frac{5a\rho}{27\rho_g}\left(\left(\frac{\rho_g V_o 2a}{\mu_g}\right)^{3/5} - \frac{2}{5}\right) && 1 < Re_o < 10^3, \\ &= \frac{2a^2\rho V_o}{9\mu_g} && Re_o < 1, \end{aligned} \tag{3.3}$$

where ρ is the droplet density and l_s is measured from the point where the droplet has a velocity V_o (this point can strictly speaking not be taken at the droplet generator since the

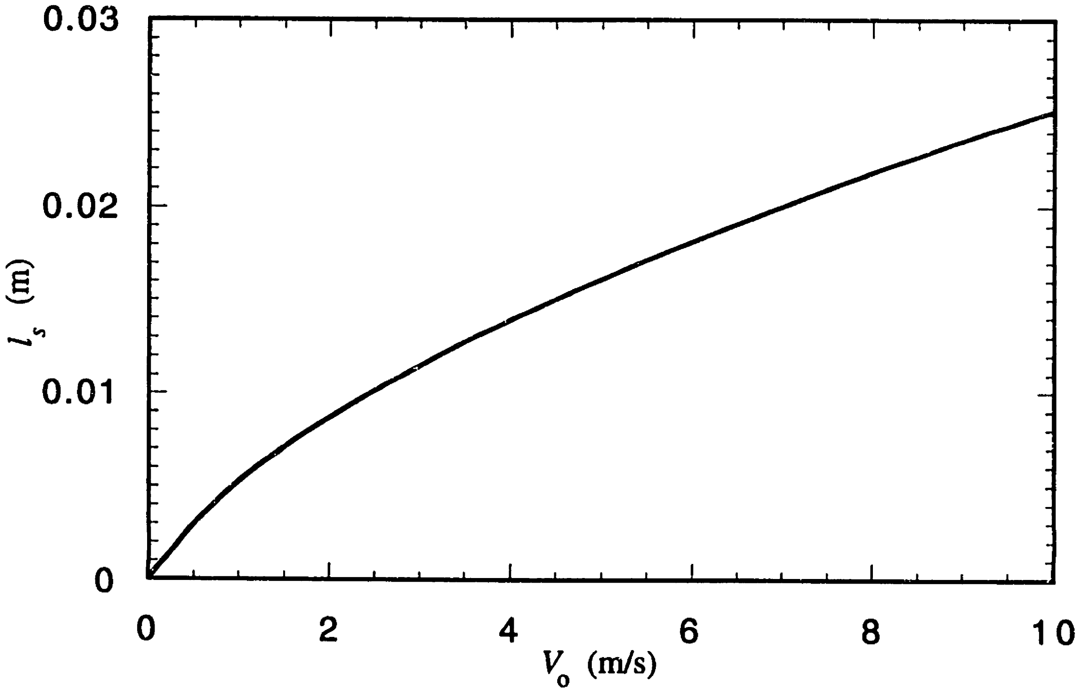

Figure 3.3. Stopping distance l_s as a function of ejection velocity V_o (Equation 3.3).

ejected liquid disengages from the generator nozzle and forms a droplet some distance downstream of it, say 0.5 mm in our experiments). $Re_0 = \rho_g V_0(2a)/\mu_g$ is the Reynolds number based on the ejection velocity V_0. Figure 3.3 shows the curve obtained from Equation (3.3) for the case of candelilla wax at temperature $T_0 = 100^oC$ and ambient air at temperature $T_a = 50^oC$. If V_0 is 3 m/s, from the curve we will have $l_s = 11.5$ mm, which is in good agreement with our observations. In our experiments l_s was 1-2 cm, and the target distance typically 2-5 mm.

The ambient air and the target were maintained at a temperature below the melt's solidification point. In-flight cooling of the droplets was typically insignificant, and they arrived at the target in superheated liquid form at essentially the temperature they had at the generator (see below).

3.3 Cooling and Solidification of Droplets

Fairly simple approximate estimates of the droplet cooling and solidification timescales can be obtained by considering a spherical molten droplet with thermal conductivity k and diffusivity α in an infinite ambient material with thermal conductivity k_a and diffusivity α_a. For the moment let the ambient material be static. At $t = 0$, the droplet is at a temperature $T_0 \geq T_f$, where T_f is the fusion temperature (which we assume to be distinct), and the ambient material with which it is in contact is at a temperature $T_a < T_f$.

The characteristic times τ associated with the thermal transient can be estimated relatively simply for the special case where they are much longer than the thermal diffusion timescales inside the droplet as well as outside, that is,

$$\tau >> \frac{a^2}{\alpha}, \frac{a^2}{\alpha_a}. \tag{3.4}$$

We shall see that these conditions are indeed satisfied in many, though not all, microdrop deposition processes. Equation (3.4) implies that the temperature inside the molten part of the droplet is essentially uniform, that is, only a function of time, as the droplet cools, and that the temperature distribution outside the droplet is quasi-steady. There are three important thermal times: (i) the time τ_l for removing the droplet's superheat and bringing the liquid down from T_0 to T_f; (ii) the additional time τ_2 for the droplet to lose all its latent heat of fusion and completely solidify; and (iii) the further time τ_3 for it to complete its cooldown to the ambient temperature T_a. One obtains

$$\tau_l = \frac{a^2}{3\alpha}\frac{k}{k_a}\ln\left(\frac{T_0 - T_a}{T_f - T_a}\right), \tag{3.5}$$

$$\tau_2 = \frac{a^2}{3\alpha}\frac{k}{k_a}\left(1 + \frac{k_a}{2k}\right)\frac{L}{c(T_f - T_a)}, \tag{3.6}$$

$$\tau_3 = 2.30\frac{a^2}{3\alpha}\frac{k}{k_a}, \tag{3.7}$$

where L is the latent heat of fusion and c is the melt's specific heat. Note that the approach to T_a in the third stage is an exponential decay from T_f, and τ_3 has been taken as the time required for the temperature difference between the droplet and T_a to be reduced to $0.1(T_f - T_a)$.

The simplifying assumption Equation (3.4) on which Equations (3.5)-(3.7) depend is valid provided $k >> k_a$ and provided $L/c(T_f - T_a)$ is not small, which is often the case. Equation (3.6) actually applies for *arbitrary* k_a/k as long as $L/c(T_f - T_a) >> 1$ (c.f. Hill & Kucera 1983). In what follows we will at times apply Equations (3.5)-(3.7) to the case $k \sim k_a$ (e.g. the case where the subcooled material to which the heat is transferred is the same as that of the droplet). In this case Equation (3.6) predicts τ_2 adequately provided $L/c(T_s - T_a)$ is large, but Equations (3.5) and (3.7) serve only as order-of-magnitude estimates for τ_1 and τ_3. The total cooldown time $\tau_1 + \tau_2 + \tau_3$ will, however, be dominated by τ_2 (see Figure 3.4).

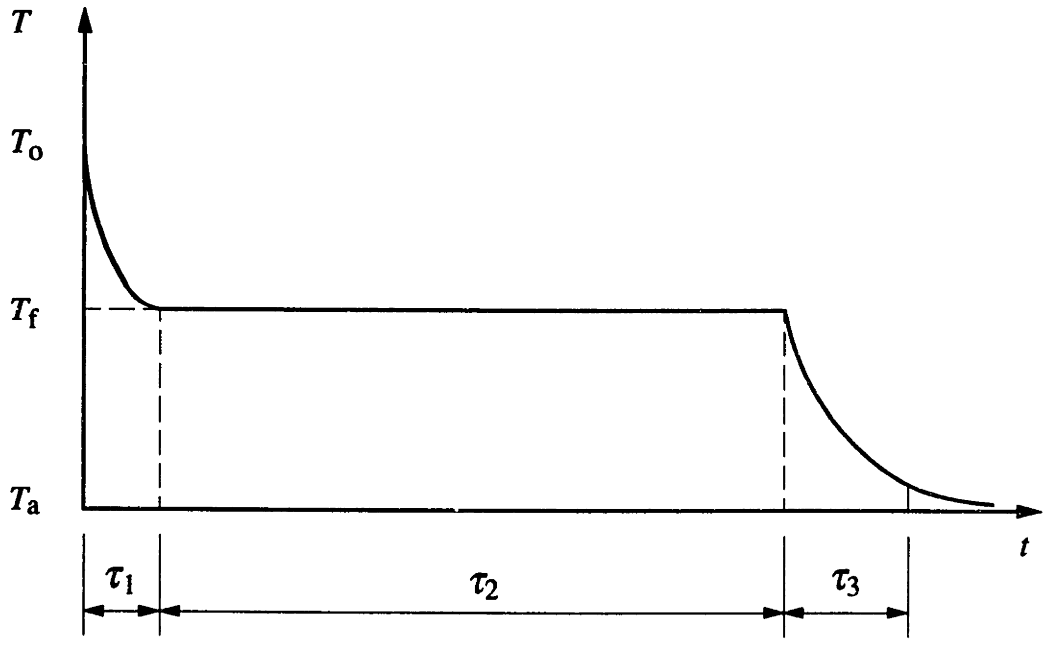

Figure 3.4. Typical thermal times.

Equations (3.5)-(3.7) can also be adapted to droplets moving through an ambient gas (e.g. traveling through air) by replacing k_a with $k_g Nu$, where k_g is the thermal conductivity of the gas and $Nu = qa/[k_a(T - T_a)]$ is the Nusselt number, q being the heat flux from the droplet and T the instantaneous droplet temperature. The Nusselt number is available as a function of the droplet Reynolds number $Re = \rho_g V(2a)/\mu_g$ and gas Prandtl number (e.g. Whitaker 1972). If $Re < 1$, $Nu \approx 1$ for gases and Equations (3.5)-(3.7) are recovered. The equations can also be adapted to sessile (post-impact) drops with a few simple approximations, as described in Chapter 4.

Chapter 4

DEPOSITION AND SOLIDIFICATION OF MOLTEN DROPLETS

This chapter is a part of the paper, "Precise Deposition of Molten Microdrops: the Physics of Digital Microfabrication" (*Proc. R. Soc. Lond.* A (1994) **444**, 533-554)
by Fuquan Gao and Ain A. Sonin.

4.1 Deposition of Single Droplets on a Flat Target

In Section 3.1, we showed the impact of a single melt droplet on a plexiglas surface (see Figure 3.1). In this Section, we will further discuss this case. On its way to the target the droplet typically cools down by only a few ^{o}C (this can be shown using the analysis which leads to Equation (3.5)) and thus impacts with essentially its source temperature T_0.

The impact occurs in this case with $We = 6$. The droplet touches the surface, wets it, showing some inertial distortion about 20 μs after impact, but quickly assumes a spherical-cap shape under the action of capillary forces, reaching what appears to be a state of mechanical equilibrium with finite contact angle long before it solidifies. The entire spreading process takes only about 40 μs in this case, while the solidification timescale is about 17 ms, three orders of magnitude longer than the spreading time (see below). The spreading time of 40 μs is roughly consistent with both the kinematic collision timescale $2a/V$ and the capillarity-driven, inertially resisted spreading timescale $(\rho a^3/\sigma)^{1/2}$; these are of the same order because $We \sim O(1\text{-}10)$. Actually, the Reynolds number $\rho V(2a)/\mu$ based on melt properties at impact is typically of the order of 10, which implies that viscous effects tend to be smaller than inertial effects during impact, but by no means negligible. Gravitational effects are, however, completely insignificant, the Bond number $\rho g a^2/\sigma$ being very small at this scale.

The post-impact solidification time τ_s can be estimated from Equations (3.5) and (3.6) as $2(\tau_1 + \tau_2)$ with k_a set equal to the thermal conductivity of the target material k_t, which in the case of Figure 3.1 is almost 6 times that of air. The factor 2 is applied because the heat transfer area to the target material is reduced from $4\pi a^2$ by about a factor of two, while the heat transfer to the air side is negligible. This gives

$$\tau_s \approx \frac{2a^2}{3\alpha}\frac{k}{k_t}\left(\ln\left(\frac{T_0 - T_a}{T_f - T_a}\right) + \left(1 + \frac{k_t}{2k}\right)\frac{L}{c(T_f - T_a)}\right) \tag{4.1}$$

and a solidification time of about 17 ms for Figure 3.1.

Note that the contact angle which the drop assumes before solidifying is not an equilibrium property. The droplet spreading occurs in Figure 3.1 under thermal nonequilibrium conditions, with the bulk of the liquid superheated and the target surface subcooled. We have observed, however, that under certain conditions the melt behaves as if it possesses an *apparent static contact angle* which is, at least approximately, a property of the melt material, the target material, and the characteristic temperatures involved, but independent of the spreading process. If the impact and spreading occur in a time short compared with the solidification time, as in Figure 3.1, the droplet will end up with a quasi-equilibrium shape with this contact angle, having apparently attained a mechanical but not thermal equilibrium, and will then freeze on a much longer timescale. The *solidification angle* is in such cases essentially equal to the apparent static contact angle of the melt before solidification, and thus, like that angle, a property of the melt material, the target material, and the characteristic temperatures, and independent of the spreading process. More about the apparent static contact angle of melt droplets will be discussed in Chapter 5.

A droplet's post-deposition shape on a flat surface can be computed straightforwardly. If a droplet with (solidified) volume $4\pi a^3/3$ is deposited as a spherical cap with solidification angle θ, mass conservation requires that its base radius r_b and cap radius of curvature R_c (Figure 4.1) be given by

$$\frac{r_b}{a} = \left(\frac{4\sin^3\theta}{(1 - \cos\theta)^2(2 + \cos\theta)}\right)^{1/3} \tag{4.2}$$

and

$$\frac{R_c}{a} = \left(\frac{4}{(1 - \cos\theta)^2(2 + \cos\theta)}\right)^{1/3} . \tag{4.3}$$

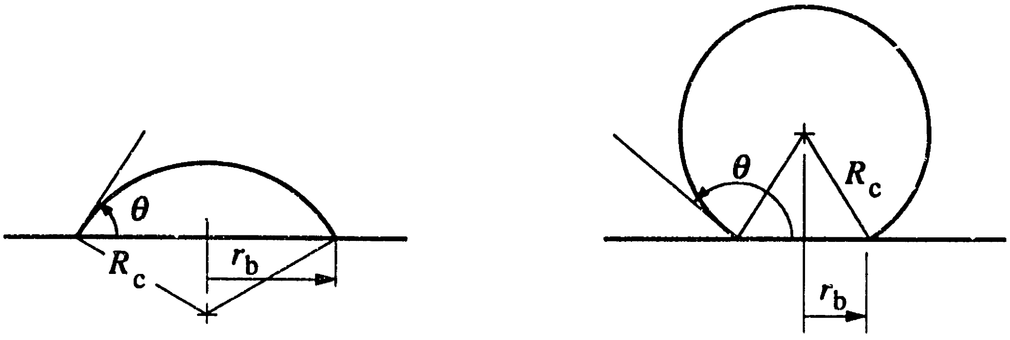

$\theta < \pi/2$ $\theta > \pi/2$

Figure 4.1. Shape parameters of solidified sessile droplets.

4.2 Columnar Deposition Modes

Figures 4.2 and 4.3 show solid structures formed by depositing 25 consecutive droplets on top of each other at various frequencies ranging from 0 to 10 kHz. At sufficiently low frequencies — below about 10 Hz in this case — a distinct *dropwise solidification* takes place where identical, vertical pillars of solidified droplets are formed independent of frequency. The slight irregularity which is observed in the pillars at low frequency is the result of the droplets being deflected from their intended path by random air currents due to the buoyancy-induced flow past the heated generator. Such irregularities can be easily avoided by using baffles to reduce the air flow.

A transition away from dropwise solidification occurs as the frequency increases, and there is insufficient time for the previous droplet to completely solidify and cool down to ambient temperature before the next one arrives. As a result the next droplet hits a "target" with higher than ambient temperature. This reduces the solidification angle between the arriving droplet and the previous droplet, and the 25-drop pillar becomes shorter and stouter. The effect increases as the frequency rises, until successive droplets begin to melt together.

At frequencies greater than about 50 Hz, there is insufficient time for solidification before the next drop arrives. The impinging droplets coalesce into a hemispherical liquid tip, and solidification takes place from the shoulder down. If the deposition is continued instead of being curtailed after 25 drops, there results a continuous growth mode where the liquid tip moves upward as the new drops arrive, leaving behind a solid rod with diameter larger than the individual droplets (Figure 4.4). At still higher frequencies — above 200 Hz, say, in Figure 4.2 — the whole burst of 25 droplet coalesces into a spherical drop which solidifies only after the salvo stops. The droplet delivery rate affects the base radius of the large drop: the base radius increases (solidification angle decreases) as the liquid

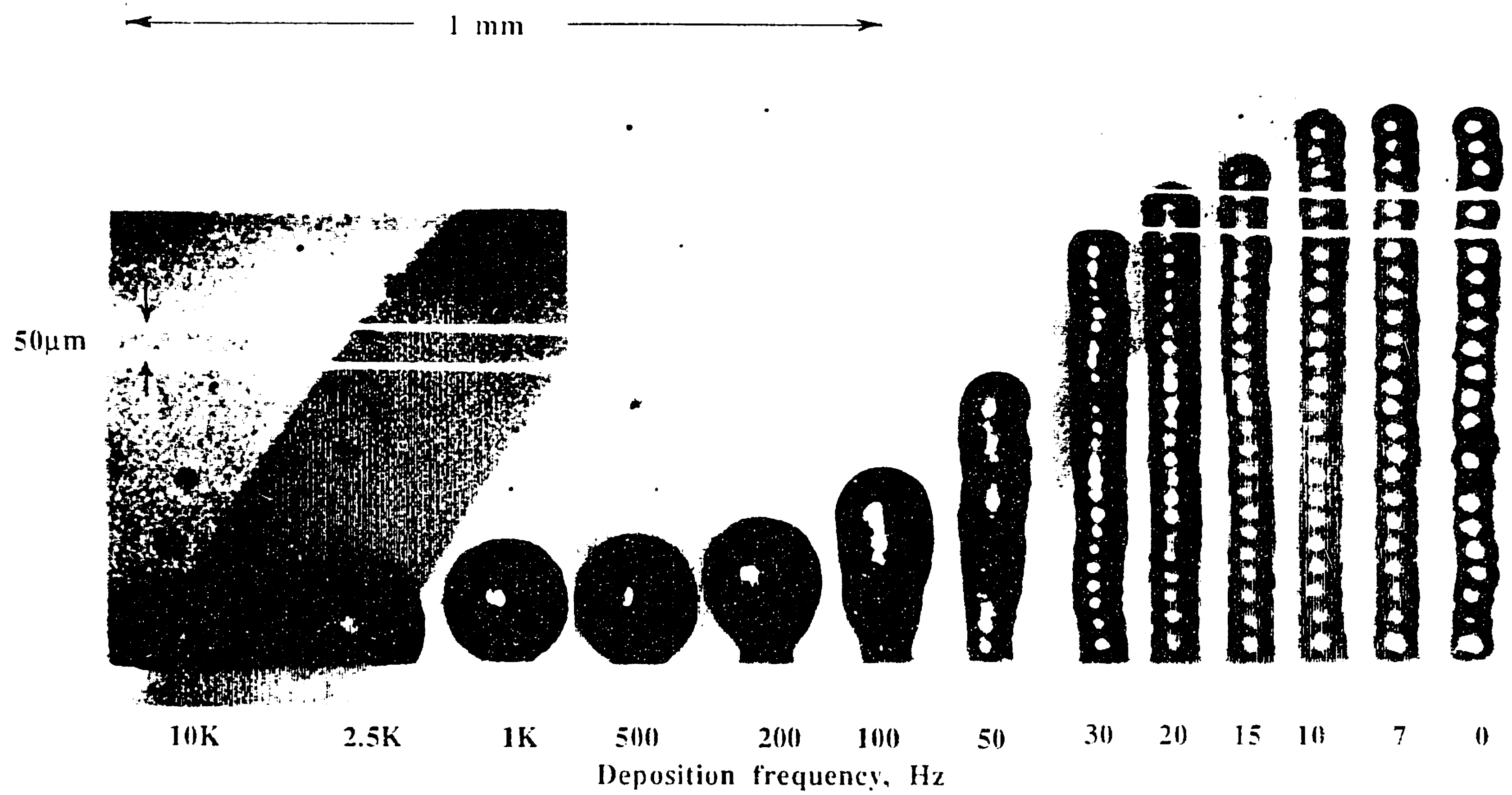

Figure 4.2. Structures produced by depositing 25 microdrops on top of each other at various frequencies. Candelilla wax, T_0 = 100°C, T_a = 38°C.

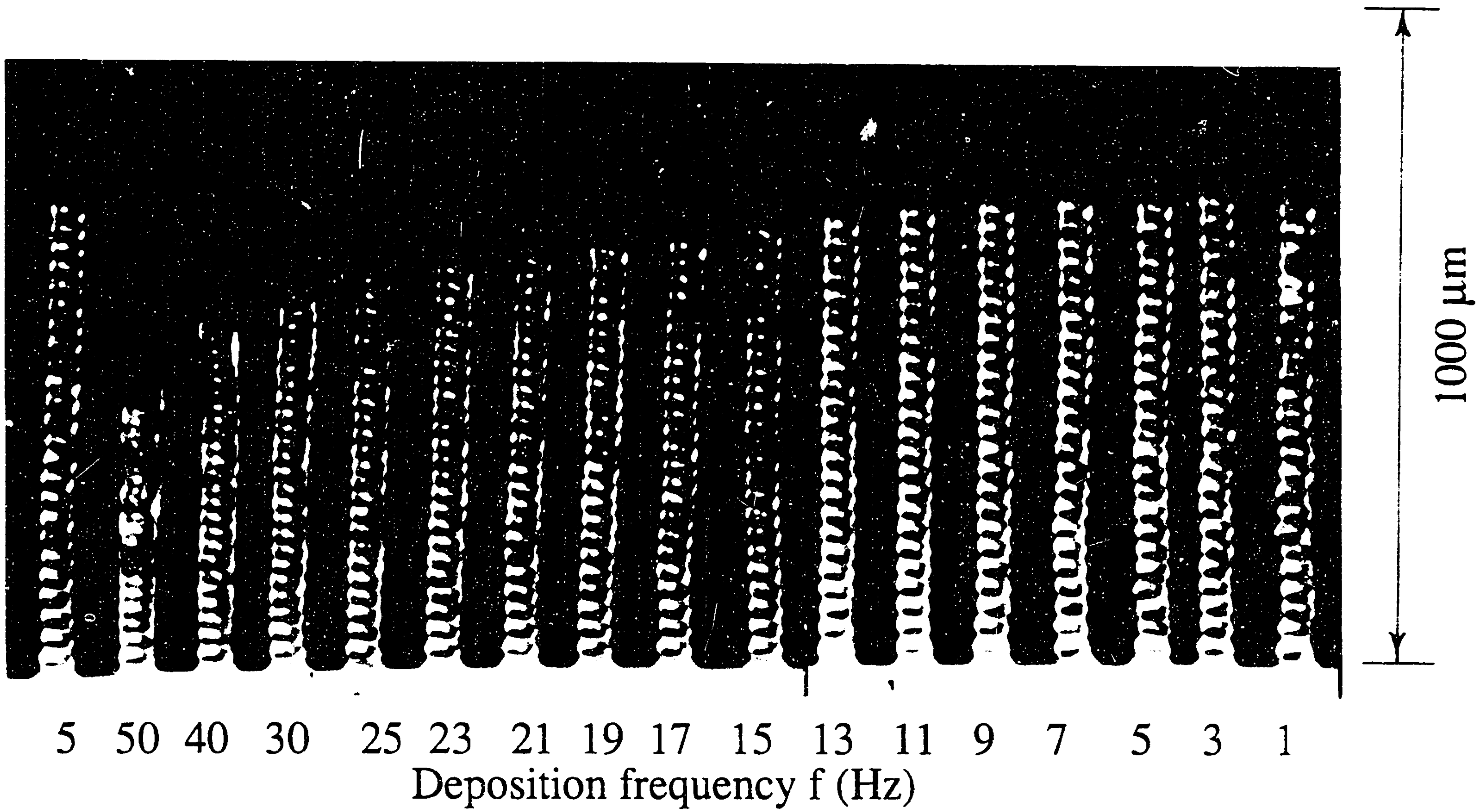

Figure 4.3. Effect of deposition frequency at the low end. 25-drop pillars of microcrystalline wax, $T_0 = 100^{\circ}C$, $T_a = 46^{\circ}C$.

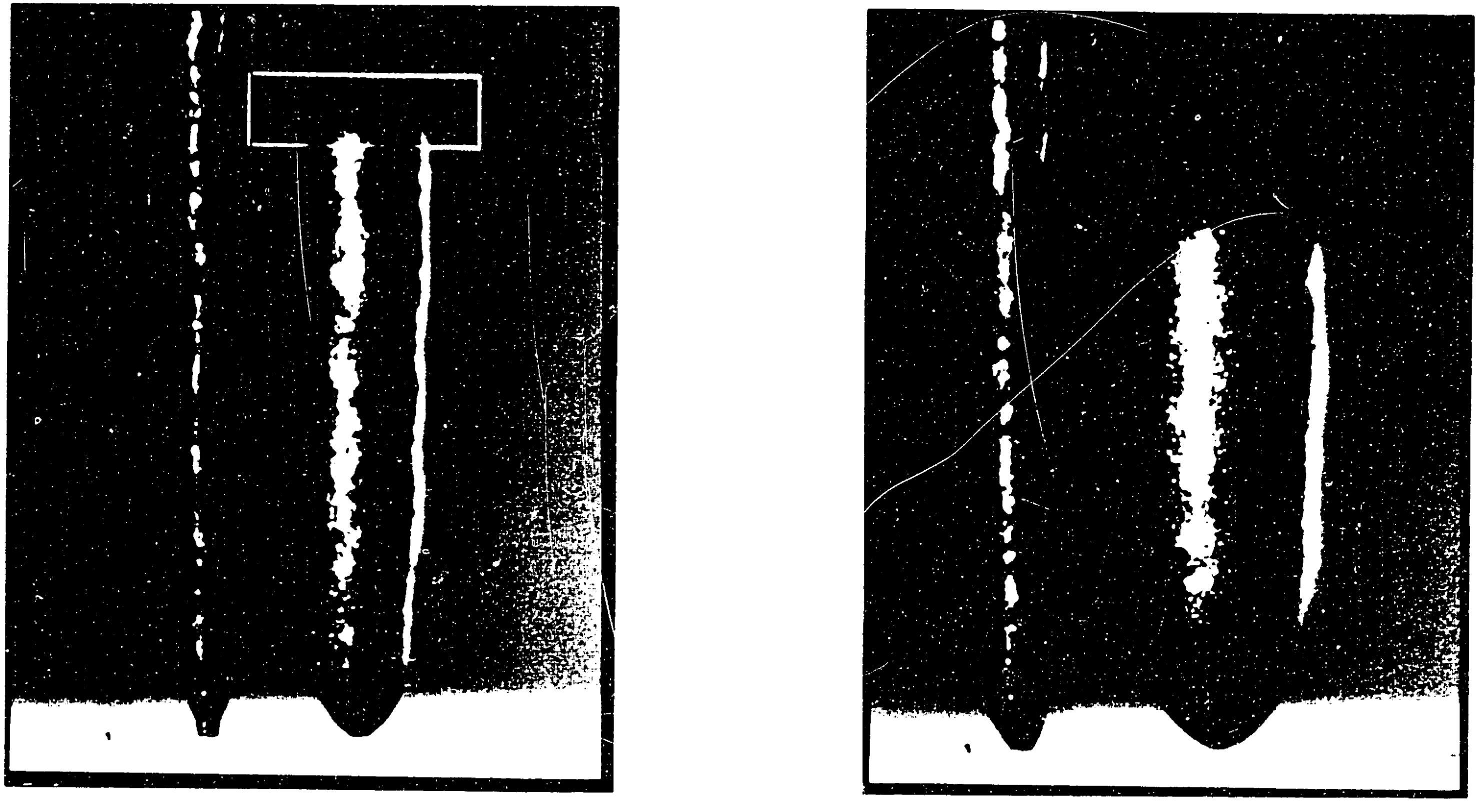

Figure 4.4. The continuos solidification mode. Candelilla wax, $T_0 = 90^oC$, $T_a = 33^oC$. Frequency, from left: 100, 500, 200, and 1,000 Hz. Rectangle: 200 µm x 600 µm.

delivery rate increases. This can be attributed to the fact that the delivery time of the 25-droplet liquid volume is in this case long compared with the solidification time, and the contact line freezes and becomes arrested on its way outward before it can attain the quasi-equilibrium contact angle as in Figure 3.1. Note that all the large drops formed by high frequency deposition would in fact grow into solid rods as in Figure 4.4 if droplet deposition were continued.

4.3 Dropwise (Low Frequency) Columnar Deposition

Three parameters characterize a "vertical" pillar produced in the low-frequency regime: (i) the radius r measured at the maximum point (Figure 4.5); (ii) the length h which is added to the pillar by each deposited droplet; and (iii) the maximum frequency at which the deposition is frequency-independent. The word "vertical" here implies only "in line with the ballistic trajectory of the incoming droplets". Gravitational effects are negligible at this scale.

Mass conservation allows the first two of these quantities to be derived straightforwardly in terms of the incoming droplet radius a and the solidification angle θ of the droplet after impact on the subcooled solid material of its own kind:

$$\frac{r}{a}=\left(\frac{2}{\sin\frac{\theta}{2}\left(3-\sin^2\frac{\theta}{2}\right)}\right)^{1/3}, \tag{4.4}$$

$$\frac{h}{a} = 2\left(\frac{2\sin^2\frac{\theta}{2}}{3 - \sin^2\frac{\theta}{2}}\right)^{1/3} . \qquad (4.5)$$

Equations (4.4) and (4.5) reduce the problem of the geometry of dropwise columnar solidification to that of establishing the solidification angle θ of the droplets: the smaller the contact angle, the shorter and stouter the column. The solidification angle will depend on

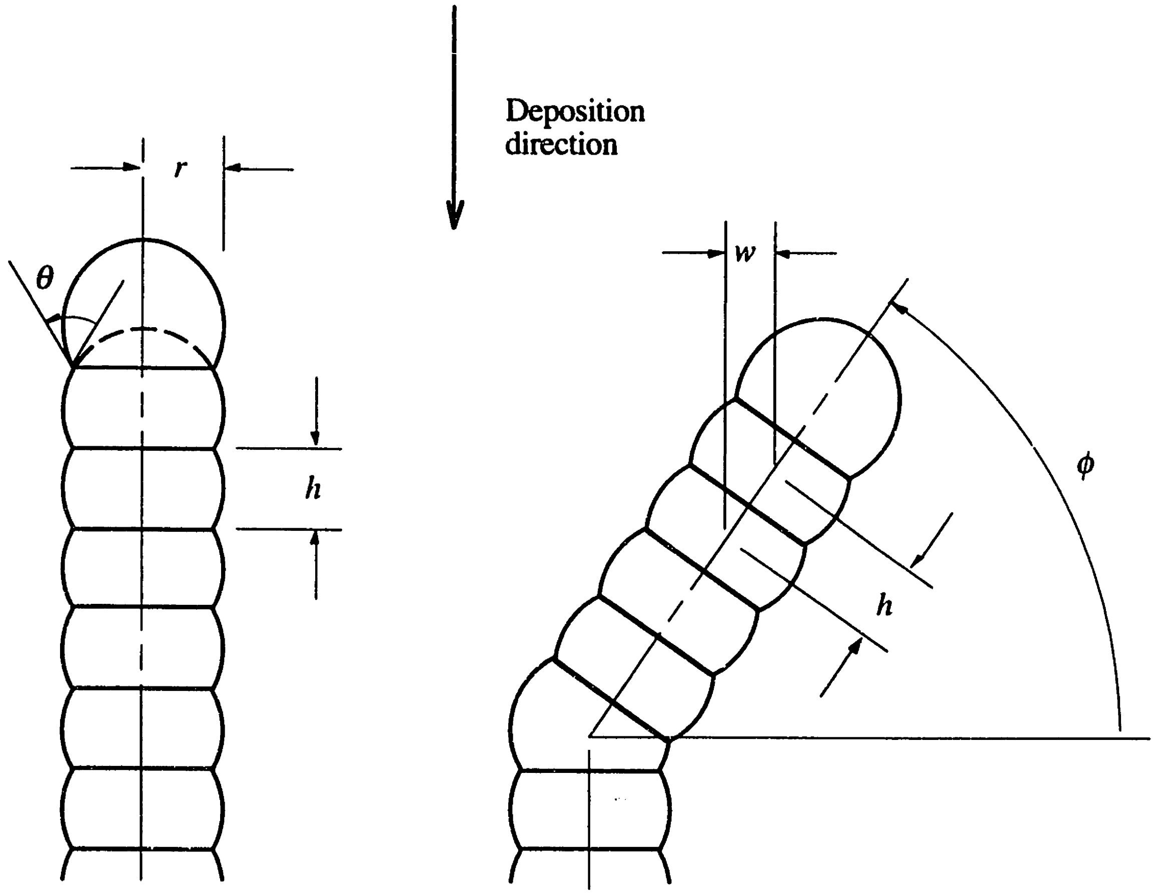

Figure 4.5. Parameters of vertical and inclined pillars produced by low-frequency dropwise deposition from above.

the properties of the melt material and the temperatures of the incoming droplet and the previously solidified material on which it lands.

The maximum frequency f_{max} at which dropwise deposition is independent of frequency can be estimated from the time required for the tip of the pillar to cool back to ambient temperature after a droplet is deposited. A frequency dependence arises when there is insufficient time for complete solidification and cooldown to ambient temperature, and the next droplet hits a target with higher than ambient temperature. This reduces the solidification angle θ for the arriving droplet, and the pillar shortens. f_{max} is thus given by

$$f_{\mathrm{max}} = \frac{1}{\tau_{\mathrm{s}} + \tau_{\mathrm{c}}}, \tag{4.6}$$

where τ_{s} is the last droplet's solidification time and τ_{c} is the additional time for it to cool down to a temperature close enough to T_{a} for the solidification angle of the next drop to be essentially the one corresponding to a target at ambient temperature.

The time estimates of Section 3.3 are inapplicable here because in most cases of interest the ambient air or other gas will have a much lower thermal conductivity than the solidified pillar of droplets, and the pillar will act as a heat transfer fin (Figure 4.6). We assume that $k_{\mathrm{g}} << k$ and model the pillar as being a semi-infinite cylinder (more on this below) with a radius R_{p}, which is approximately equal to the incoming droplet radius, a. Before a molten droplet arrives at the pillar's tip at $x = 0$, the entire pillar is at the ambient air temperature T_{a}. At $t = 0$, a molten drop arrives. The resulting temperature transient in the solid part of the cylinder will be controlled by the fin heat transfer equation

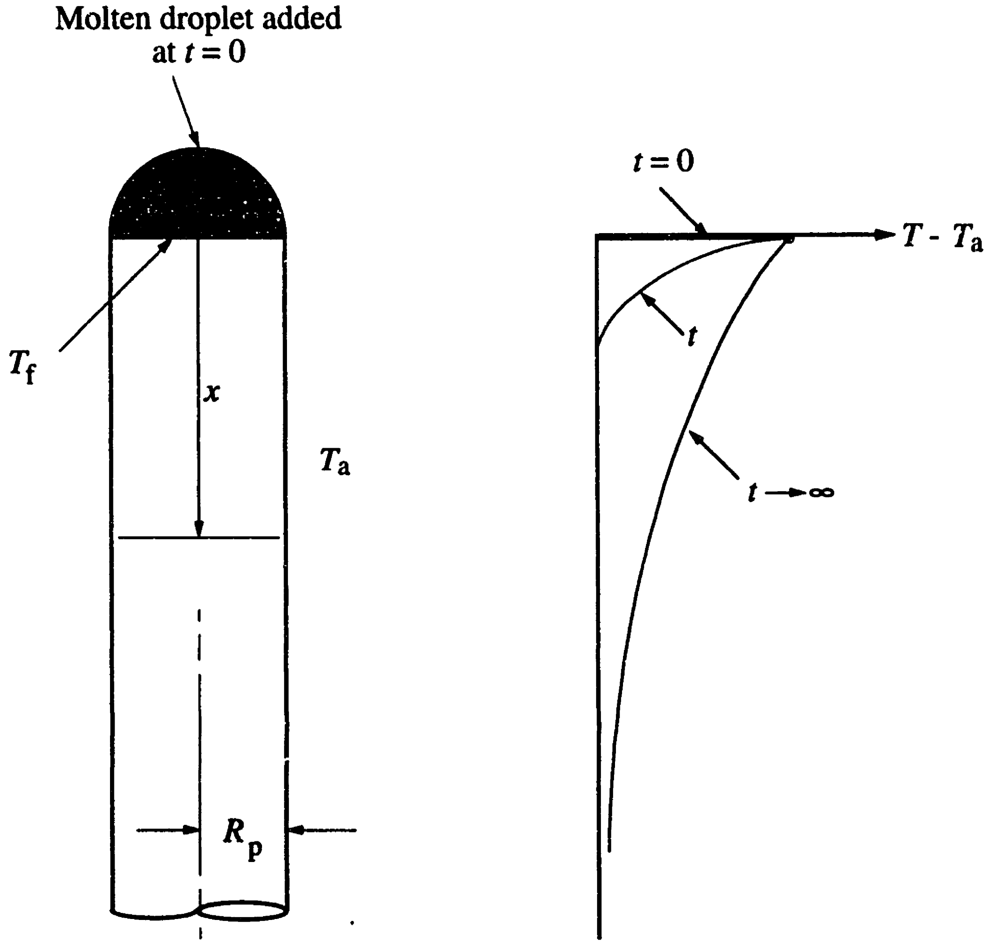

Figure 4.6. Model for solidification and cooldown times in the low-frequency dropwise deposition mode.

$$\frac{\partial \omega}{\partial t} = \alpha \left(\frac{\partial^2 \omega}{\partial x^2} - \frac{\beta \omega}{R_p{}^2} \right), \tag{4.7}$$

where

$$\omega(x,t) = \frac{T - T_a}{T_f - T_a},$$

$$\beta = \frac{2k_g Nu}{k} \tag{4.8}$$

and $Nu = qR_p/[k_g(T - T_a)]$ is the Nusselt number based on the cylinder radius and radial heat flux q from the cylinder to the air, k_g being the thermal conductivity of the ambient gas; $Nu \approx 1$ in the present application.

We assume that the dominant contribution to the solidification time τ_s is the time for the droplet to lose its latent heat of fusion. This time can be computed by solving Equation (4.7) for the temperature distribution, obtaining the heat flux $q_o(t)$ at $x = 0$, and using the energy balance

$$\rho \frac{4\pi a^3}{3} L = \pi R_p{}^2 \int_o^{\tau_s} q_o(t) \mathrm{d}t \, . \tag{4.9}$$

If furthermore $\tau_s >> a^2/\alpha$ and $L/[c(T_f - T_a)]$ is reasonably large, the fusion front can be modelled as being fixed at $x = 0$ as the thermal effects diffuse into the column, and the appropriate boundary conditions for Equation (4.7) while the droplet is solidifying taken as $\omega(0,t) = 1$ and $\omega(\infty,t) = 0$. The general solution has been worked out by Lowan (1945), but is analytically cumbersome. To get scaling laws in simpler analytic form, we piece together a solution from the small-time and large-time limiting cases of $q_o(t)$ by assuming that the transition from one to the other occurs at a time when the two give the same result. At small times the second right-hand term in Equation (4.7) is negligible and we obtain a complementary error function solution for temperature and

$$q_o(t) = \frac{k(T_f - T_a)}{\sqrt{\pi \alpha t}}. \tag{4.10}$$

The large-time solution is the final steady state with the left-hand side of Equation (4.7) zero. This gives the well-known solution which decays exponentially with x and where

$$q_o = \frac{k(T_f - T_a)}{R_p}\sqrt{\beta} \tag{4.11}$$

The patched solution for the droplet's solidification time can be summarized as

$$\begin{aligned} \tau_s &= \frac{4\pi}{9}\left(\frac{a}{R_p}\right)^4 \frac{a^2}{\alpha}\left(\frac{L'}{c(T_f - T_a)}\right)^2 & \xi < 1, \\ &= \frac{a^2}{\pi\alpha}\left(\frac{R_p}{a}\right)^2 \frac{(2\xi - 1)}{\beta} & \xi > 1, \end{aligned} \tag{4.12}$$

where

$$\xi = \frac{2\pi}{3}\left(\frac{a}{R_p}\right)^3 \frac{L'}{c(T_f - T_a)}\sqrt{\beta}\,. \tag{4.13}$$

Here, L' should strictly speaking be the latent heat, but by including in it the droplet's superheat

$$L' = L + c(T_o - T_f) \tag{4.14}$$

we include in τ_s the time for the droplet to cool from T_o to T_f (c.f. Equations (3.5) and (3.6) with $c(T_o - T_f) << L$).

Based on Equation (4.7), the post-solidification cooldown occurs exponentially with an e-folding time of $R_p^2/\alpha\beta$. If we (arbitrarily) assume that the temperature is close enough to T_a when $T - T_a$ has been reduced to 10% of $T_f - T_a$, we obtain a characteristic cooldown time of

$$\tau_c = 2.30\left(\frac{R_p}{a}\right)^2 \frac{a^2}{\beta\alpha}\,. \tag{4.15}$$

The maximum frequency f_{max} now follows directly from Equations (4.6), (4.12), and (4.15). At any frequency below this value the deposition will be dropwise and its shape parameters will be independent of frequency. For the data of Figure 4.3, Equation (4.6) with $R_p \approx a$ gives f_{max} = 12 Hz, which is in good agreement with the observations. Our model for f_{max} appears to be approximately correct.

Note that our expression for f_{max} is based on the assumption of an "infinite" column. This is valid only if the column is long compared with the characteristic distance to which the temperature profile has penetrated at time τ_s. If we define x_e as the coordinate of the point at which $T - T_a$ equals $(T_f - T_a)/2.71$ at time τ_s, we obtain from the temperature distribution associated with the small and large time solutions, respectively, that

$$\frac{x_e}{a} = 0.80\left(\frac{a}{R_p}\right)^2 \frac{L}{c(T_f - T_a)} \qquad \xi < 1,$$

$$= \frac{R_p}{a}\frac{1}{\sqrt{\beta}} \qquad \xi > 1. \qquad (4.16)$$

Equation (4.12) is intended for cases where the column's length is much larger than x_e, so that heat loss through its base can be neglected. For the data of Figures 4.2 and 4.3, for example, the distance x_e/a is only about 2, so that the infinite-column approximation does indeed apply except for the first couple of droplets deposited on the substrate. This value of x_e/a is low because wax has very low conductivity. With metals, for example, the values would be much greater.

The free-standing letters in Figure 1.2 were created in the dropwise solidification mode. Note that even a "horizontal" member can easily be made with this technique by deposition from "above", since capillary forces dominate over inertial forces at impact. The "horizontal" center-to-center separation between two consecutive droplets simply has to be adjusted so that the next drop will touch the last solidified one, grab onto it by capillarity, spread partly over it, and solidify.

By adjusting the ratio of the horizontal center-to-center drop spacing, w, to the incoming droplet radius, a, one can give a pillar of droplets any slope ϕ between 0° and 90° (Figure 4.5). The precise relationship between w/a and ϕ depends on the apparent contact angle (and possibly also somewhat on the Weber number at impact, if that number is not sufficiently small). If inertial effects are insignificant compared with capillary forces (i.e. the Weber number $\rho V^2 a/\sigma$ is not too large) one would expect that

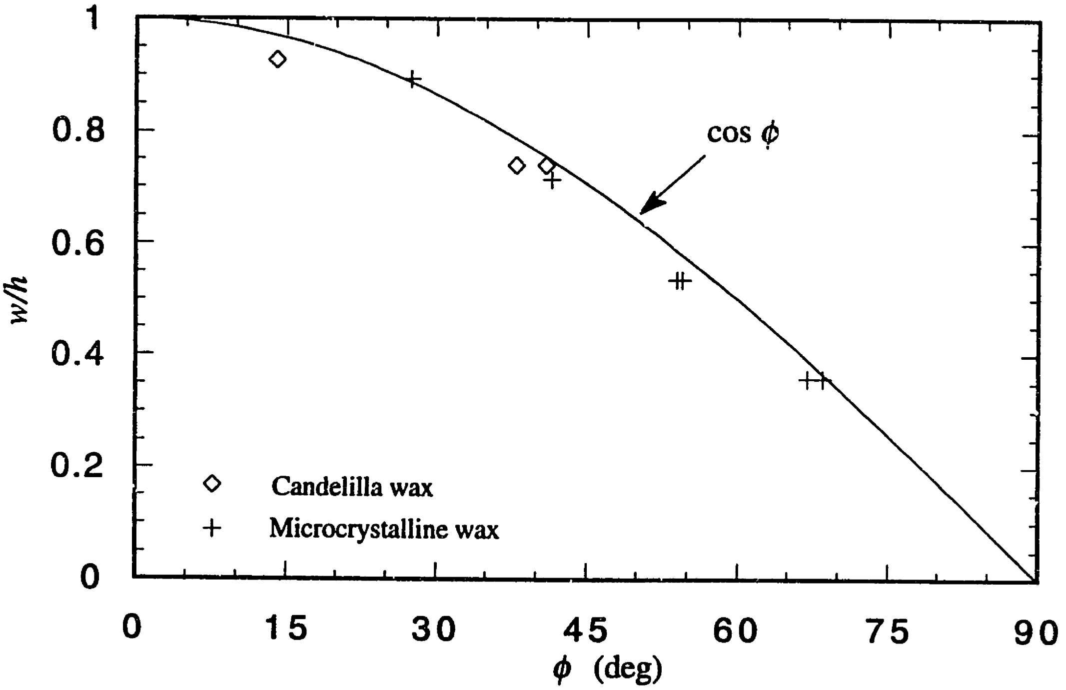

Figure 4.7. The relationship between a pillar's angle ϕ and the horizontal center-to-center deposition spacing w. The data points are for $We < 6$.

$$\frac{w(\phi)}{h} = \cos\phi\,, \tag{4.17}$$

where h is the height added to a vertical pillar by each drop and is given in terms of a and θ by Equation (4.5). Equation (4.17) is in good accord with our observations (Figure 4.7).

4.4 Continuous (High Frequency) Columnar Deposition

A gradual transition away from dropwise solidification occurs in Figures 4.2 and 4.3 as the frequency increases from about 10 Hz to 50 Hz. At sufficiently high frequencies there is insufficient time between droplets for any solidification. The first of the arriving droplets coalesce on the target surface into a larger, spherical-cap liquid drop (surface tension dominates at this scale) which spreads as more liquid arrives, maintaining at first a spherical cap shape. As this coalesced drop grows, however, its contact line advance rate over the cool target surface slows and eventually becomes so slow that solidification sets in at the contact line and arrests the spreading. The point at which this occurs depends on deposition frequency (spreading speed), material properties, and the characteristic temperatures (more on this later). After contact line arrest the large drop grows for a while more by bulging out over the frozen contact line, maintaining an approximately spherical-cap shape, but then the solidification spreads upward from the base and begins also at the sides as a result of heat loss to the ambient air. Eventually an asymptotic state results where a hemispherical liquid cap rises upward at a steady rate, fed from above by the arriving droplets and chased from below by a solidification front, leaving behind it a continuous, cylindrical solid rod of constant diameter (Figure 4.4). The diameter of the solid is controlled by the enthalpy flux associated with the melt deposition and by the heat flux from the hemispherical cap to the ambient air: a steady state is attained when interfacial solidification sets in precisely at the shoulder of the liquid cap.

This *continuous solidification mode* will invariably result if the deposition frequency is high enough and if the deposition is continued long enough to form an adequate solid base and establish a steady-state growth. This mode is, in essence, a microscale version of the Verneuil crystal growth process, and may conceivably be used for growing fine, continuous, single-crystal fibers.

A simple theory for continuous deposition can be derived by referring to Figure 4.8, which depicts the process in the steady state reference frame which moves upward with the cap. Droplets at temperature T_0 arrive from above at a mass flow rate $\rho 4\pi a^3 f/3$, where a is the droplet radius and f is the deposition frequency, and coalesce into the hemispherical liquid cap. The liquid in the cap is cooled by heat loss to the ambient air, and the cap radius R adjusts itself so that the temperature reaches the fusion point T_f precisely at the cap's base, at which point solidification starts at the column's periphery. Below the cap the solidification front grows inward as heat is lost via the sides, while the liquid in the interior maintains itself at fusion temperature.

We write the heat flux q from the cap to the air in terms of the Nusselt number Nu based on the local temperature T and the cap radius R,

$$Nu = \frac{qR}{k_g(T - T_a)}, \tag{4.18}$$

the assumption being that the heat flow resistance is primarily on the air side rather than in the melt itself, which is true if $k_g Nu << k$, k being the melt's thermal conductivity. In what

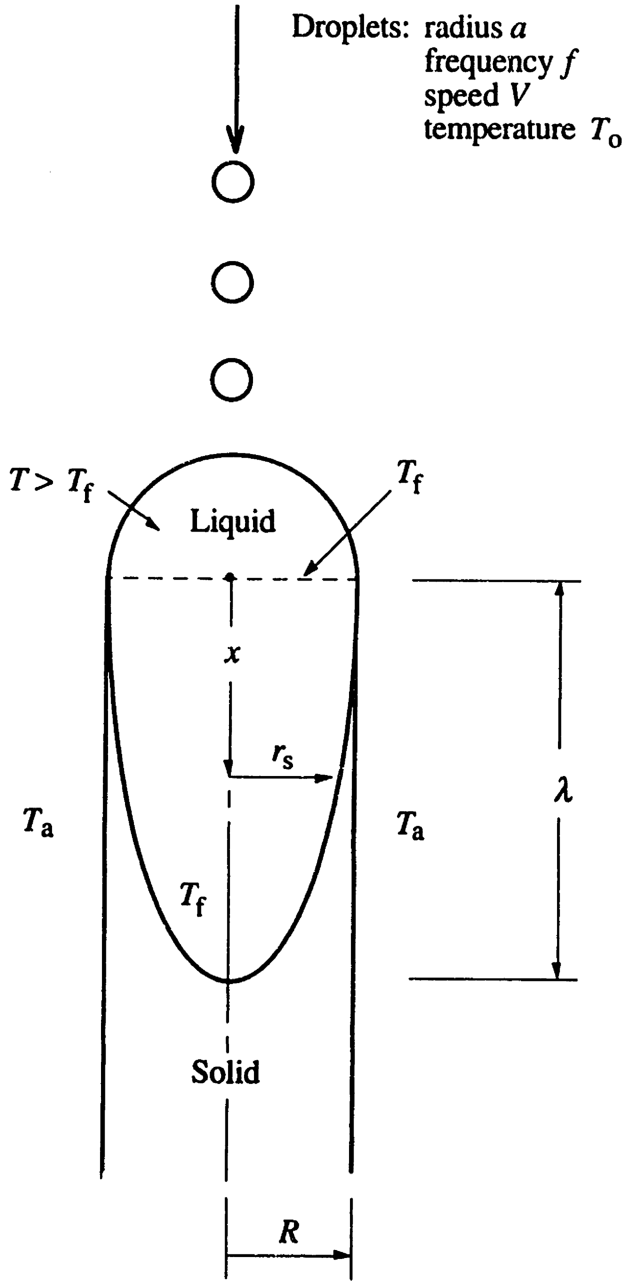

Figure 4.8. Cross section of continuously growing column in the high-frequency mode.

follows, the average value of $(T - T_a)$ over the cap is taken as the logarithmic average. The heat loss through the base is neglected, the liquid below being at fusion temperature. An expression for the column's radius R is obtained by writing down the first law of thermodynamics for a control volume comprised of the hemispherical liquid cap, setting the temperature equal to T_f in the outflow at the base. The result is

$$R = \frac{2\rho a^3 fc}{3k_g Nu} \ln\left(\frac{T_o - T_a}{T_f - T_a}\right). \tag{4.19}$$

Figure 4.9 shows some data for R obtained with two different waxes over a range of deposition frequencies, and compares them with Equation (4.19) taking $Nu \approx 1$ (rigorous for a spherical body in still air). Except at the lower frequencies, the agreement is quite good, given the simple nature of the theory. Note that our continuous growth model is based on the implicit assumption that $R >> a$.

An equally simple theory can be written for the solidification front below the cap, based again on the assumption $k_g Nu << k$, where Nu now refers to the Nusselt number associated with the sides of the cylinder somewhat below the base of the cap. (This Nu will still not differ much from unity at the scales and conditions involved here.) The radially inward progress of the solidification front at $r_s(x)$, where x is the distance down from the spherical cap's base, can be viewed as a problem in time by writing $x = Ut$, where $U = 4\pi a^3 f/(3\pi R^2)$ is the material's downward flow speed in the reference frame of Figure 4.8. At any given x (or t) the latent heat of fusion is removed from r_s laterally by heat transfer through the solidified annulus to the air. If $k_g Nu << k$, the temperature of the outer wall of the solid will differ little from T_f, and the energy equation can be written

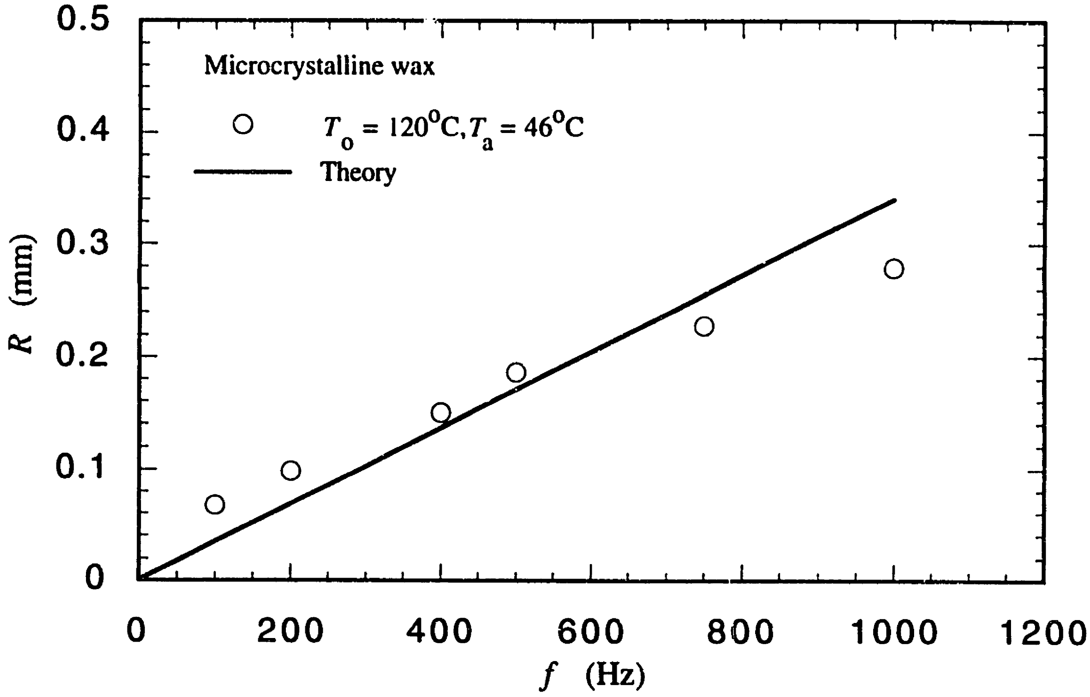

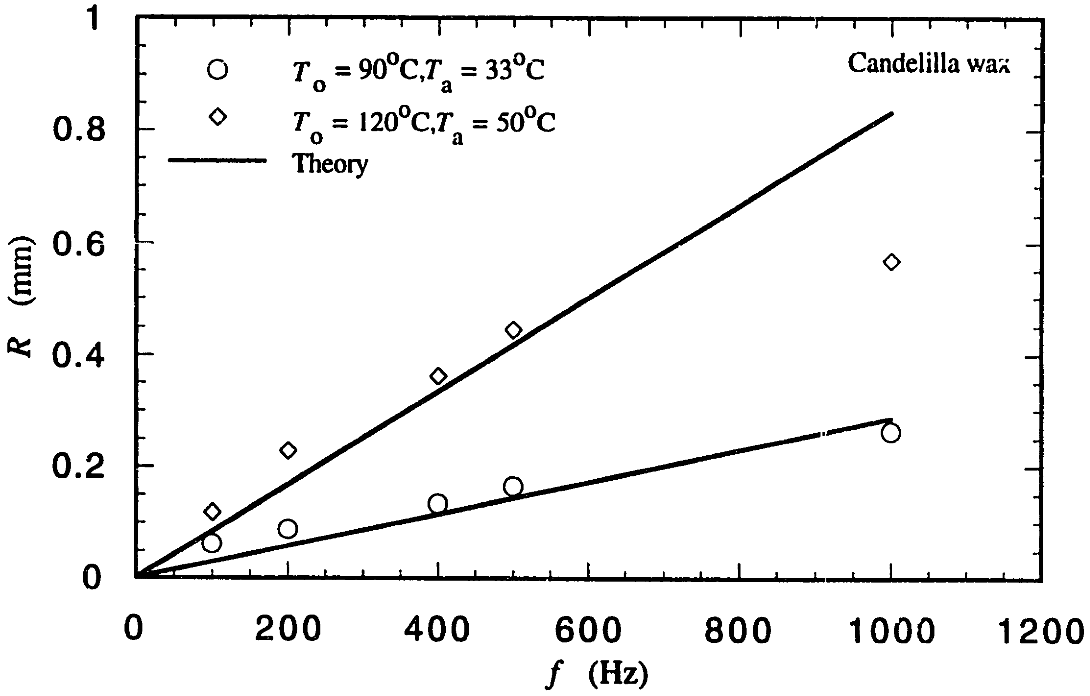

Figure 4.9. Column radius in the continuous solidification mode: experiment against theory.

$$L\frac{\mathrm{d}}{\mathrm{d}t}(\rho\pi r_s{}^2) = -2\pi R k_g Nu\frac{(T_f - T_a)}{R}. \tag{4.20}$$

An integration with $r_s(0) = R$ and transformation from t back to x yields the shape of the solidification zone as

$$r_s/R = \sqrt{1 - x/\lambda}, \tag{4.21}$$

where λ is the axial length of the solidification zone and is given by

$$\frac{\lambda}{R} = \frac{L}{c(T_f - T_a)}\frac{1}{\ln\left(\frac{T_o - T_a}{T_f - T_a}\right)}. \tag{4.22}$$

For a typical case with wax, this yields $\lambda/R \approx 2$. Video and visual observations using translucent waxes showed the liquid cap as a smooth, transparent hemisphere with a semi-opaque solid afterbody inside which a faintly visible molten region could be seen, much like the parabolic prediction sketched in Figure 4.8, with $\lambda/R \approx 2$. Visibility was not, however, adequate for accurate comparisons. These observations also suggested that the liquid region sketched in Figure 4.8 was not motionless relative to the solid: the tiny particles or bubbles which were occasionally visible in the liquid would execute a motion which suggested a circulatory flow field in the liquid region, with what appeared to be downward velocities near the axis and upward velocities near the boundary, presumably driven by the momentum flow rate of the incoming droplet stream at the cap's apex.

4.5 Sweep Deposition of Beads on Flat Surfaces

When a generator dispenses droplets at a frequency f while moving over a flat target at a speed U, the droplets will land with a center-to-center separation

$$w = U/f. \tag{4.23}$$

A line of separate sessile droplets will form if w is sufficiently large. The droplets will overlap, on the other hand, if $w < 2r_b$ for $\theta < \pi/2$ or $w < 2R_c$ for $\theta > \pi/2$, r_b being the base radius of a sessile droplet and R_c its radius of curvature as illustrated in Figure 4.1. Using Equations (4.2), (4.3), and (4.23), the condition for droplet overlap can be expressed as

$$\frac{f(2a)}{U} > F(\theta), \tag{4.24}$$

where

$$\begin{aligned} F(\theta) &= \left(\frac{(1 - \cos\theta)^2(2 + \cos\theta)}{4\sin^3\theta}\right)^{1/3} \qquad (\theta < \pi/2), \\ &= \left(\frac{(1 - \cos\theta)^2(2 + \cos\theta)}{4}\right)^{1/3} \qquad (\theta > \pi/2), \end{aligned} \tag{4.25}$$

θ being the solidification angle. If the time between successive droplets is small compared with that required for solidification, and if Equation (4.24) is satisfied, overlapping droplets will tend to coalesce by capillary action and form a continuous bead before the melt solidifies. Figure 4.10 summarizes the conditions where this is possible.

Figures 4.11-4.13 show top and side views from two series of sweep deposition experiments, each performed at a fixed sweep speed U but over a range of frequencies. As expected, separate drops are formed at lower frequencies. A transition to a smooth solid bead of constant width takes place at about the point predicted by Equation (4.24). This region ends in the case of Figures 4.11 and 4.12 at high frequencies when bulges appear on the bead and grow in amplitude as the frequency increases further (more on this below).

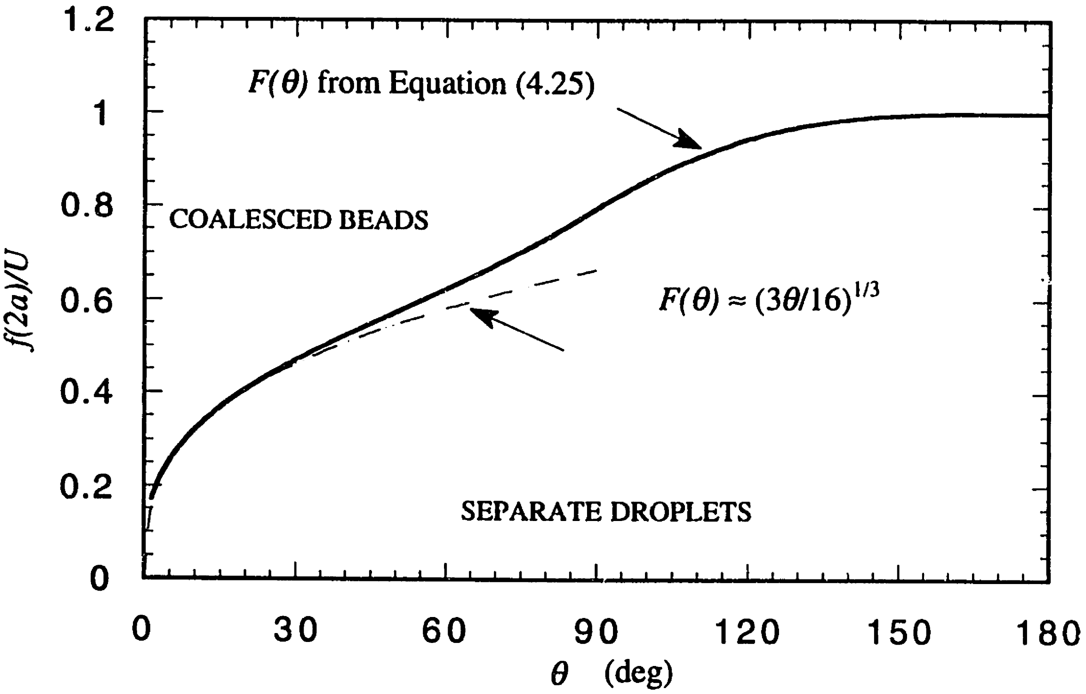

Figure 4.10. Droplet coalescence threshold and operating regimes for sweep deposition.

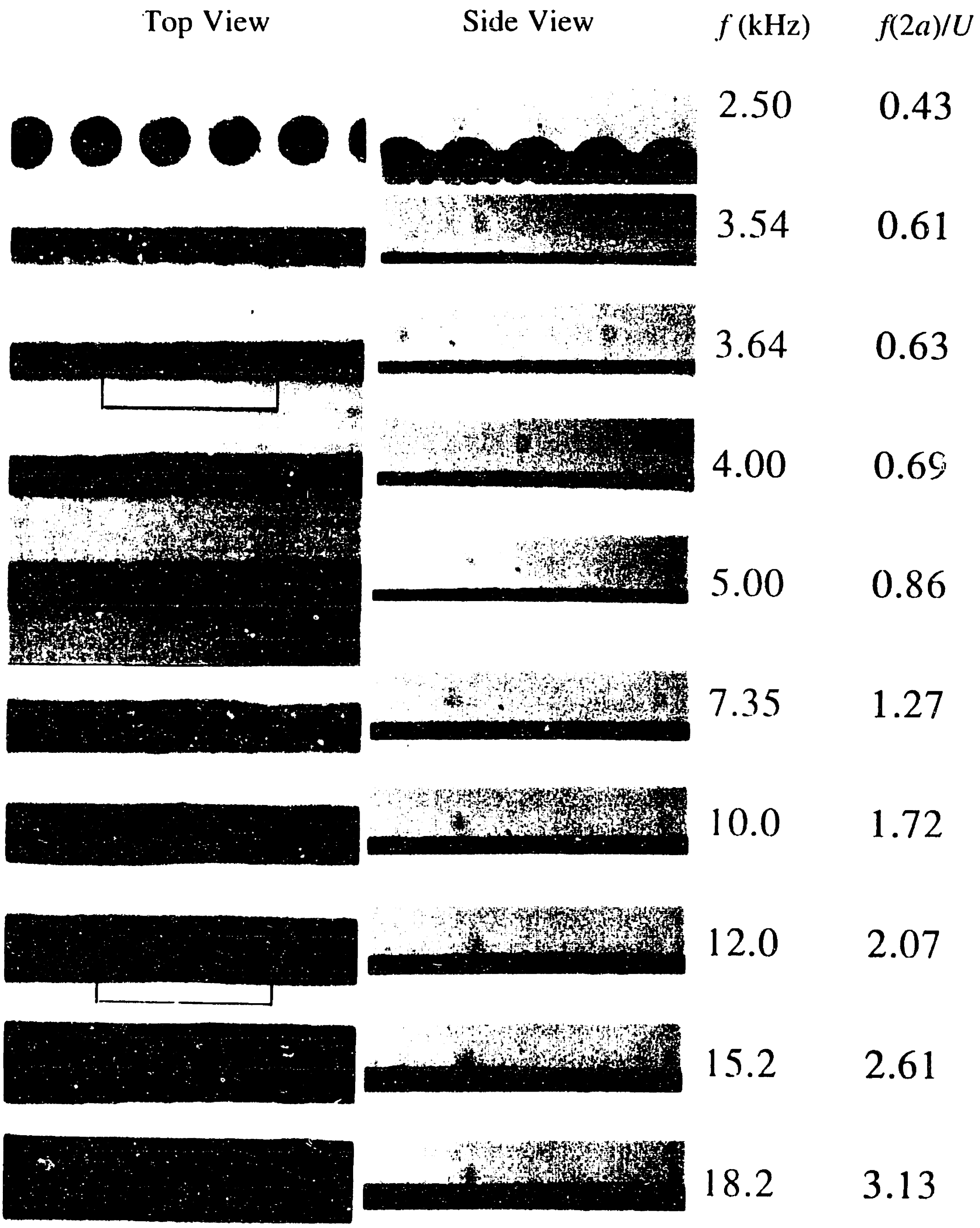

Figure 4.11. Sweep deposition at high speed and high target temperature. Candelilla wax on plexiglas, $2a = 50.5$ μm, $U = 0.293$ m s^{-1}, $T_0 = 90$°C, $T_a = 58$°C. The rectangle's length is 300 μm.

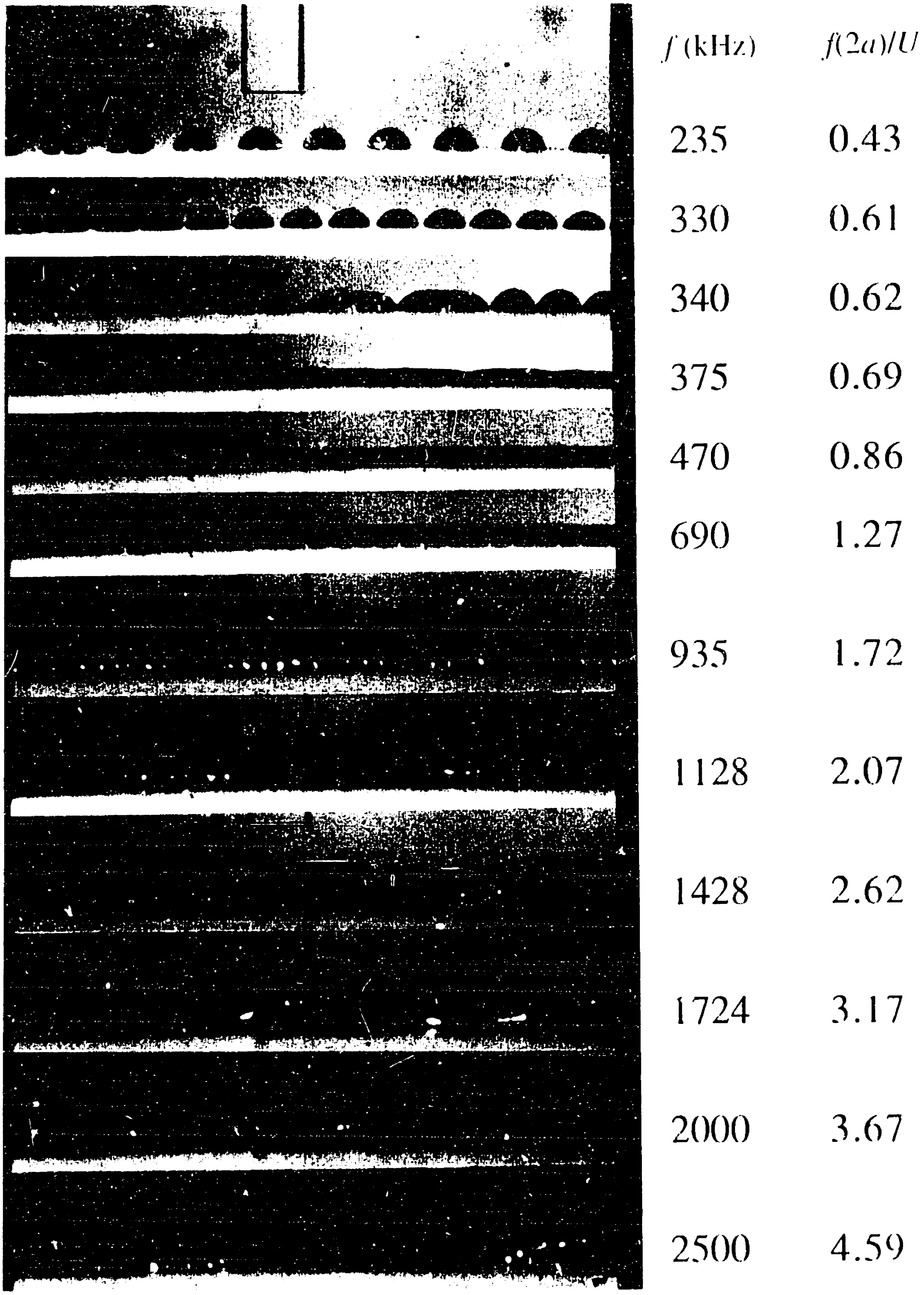

Figure 4.12. Sweep deposition at low speed and low target temperature, side view. Candelilla wax on plexiglas, $2a$ = 50.5 μm, U = 0.0275 m s^{-1}, T_0 = 90°C, T_a = 45°C. The rectangle's breadth is 100 μm.

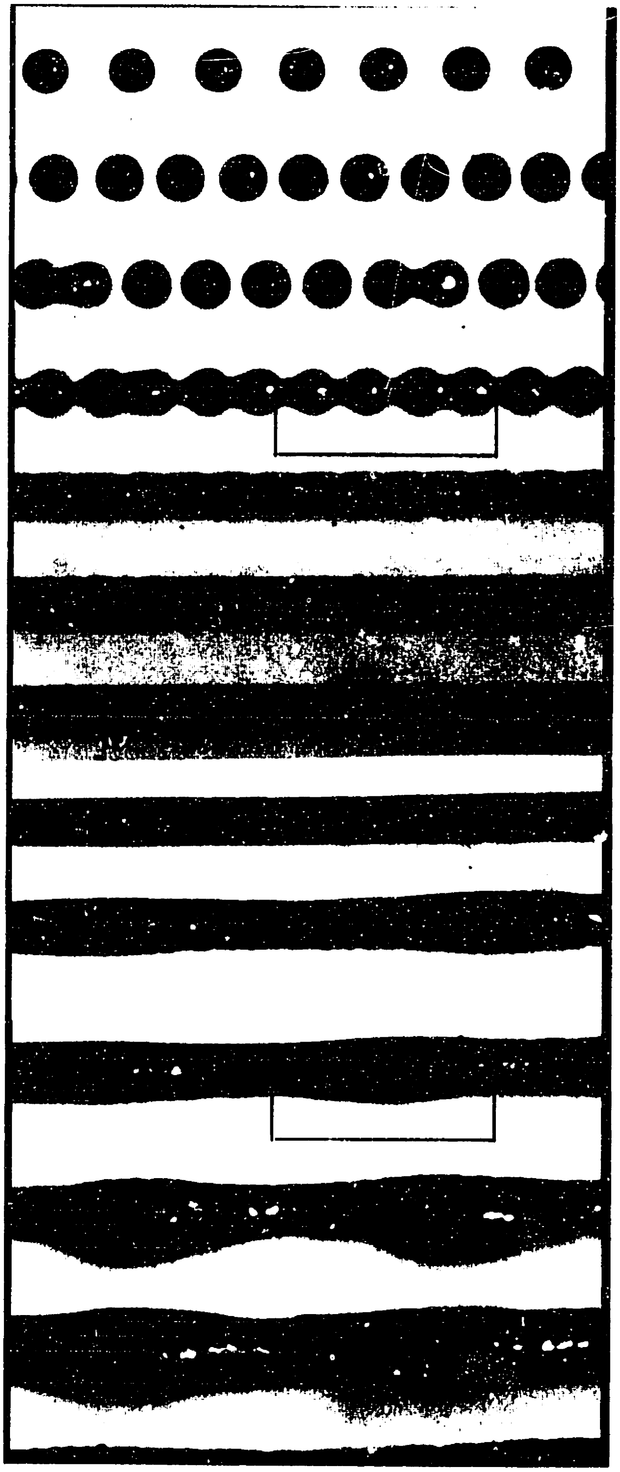

f (kHz)	$f(2a)/U$
235	0.43
330	0.61
340	0.62
375	0.69
470	0.86
690	1.27
935	1.72
1128	2.07
1428	2.62
1724	3.17
2000	3.67
2500	4.59

Figure 4.13. Top view of the beads in Figure 4.12. The rectangle's length is 300 μm.

Bead deposition has potential uses such as laying down electrically conductive (or resistive) lines on a substrate, and we wish to understand the conditions under which a smooth bead forms and to predict the bead's geometry as a function of operating conditions and material properties. In what follows we present a model written in terms of the material's solidification angle θ, the assumption being that this angle can, over a range of conditions where the melt spreads to a quasi-equilibrium condition much faster than it solidifies, be considered a property of the melt and target materials and the temperatures involved.

When a smooth bead forms the bead's shape is governed by the solidification angle and by mass conservation, which can be expressed as

$$\frac{4\pi a^3 f}{3} = UA, \tag{4.26}$$

where A is the bead's cross-sectional area. The bead's cross-section will have the shape of a segment of a circle as shown in Figure 4.14. The bead's cross-sectional area A and radius of curvature R_b are related to its base width b and solidification angle θ by the equations

$$A = \frac{b^2(\theta - \sin\theta\cos\theta)}{4\sin^2\theta}, \tag{4.27}$$

$$R_\mathrm{b} = \frac{b}{2\sin\theta}. \tag{4.28}$$

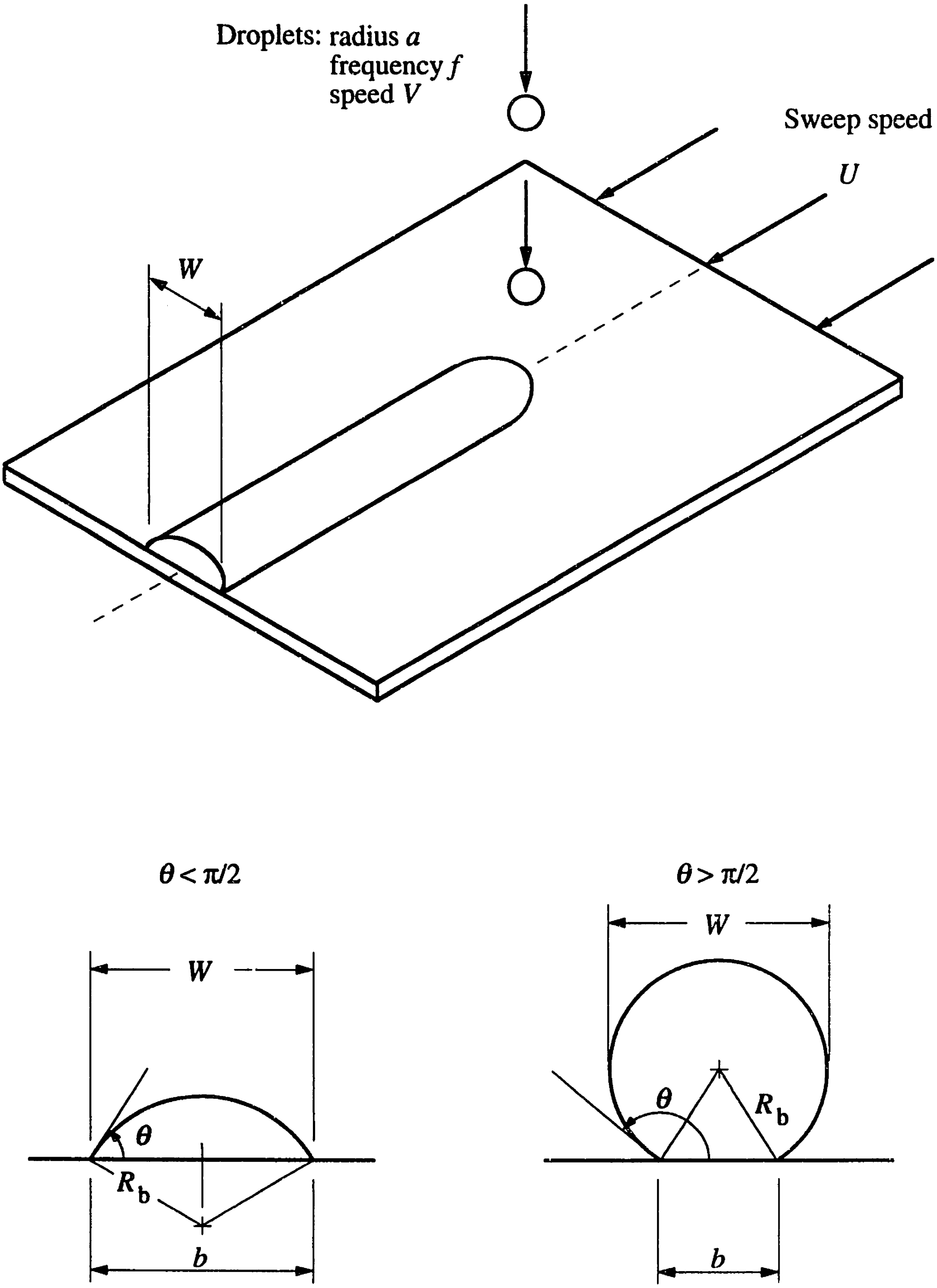

Figure 4.14. Parameters in sweep deposition of smooth beads.

Using Equations (4.26) and (4.27), we get the base width as

$$\frac{b}{2a} = \left(\frac{2\pi\sin^2\theta}{3(\theta - \sin\theta\cos\theta)} \frac{f(2a)}{U} \right)^{1/2} . \tag{4.29}$$

The maximum width W of the bead, i.e. the width seen from above, is b if $\theta < \pi/2$ and $2R_b$ if $\theta > \pi/2$, that is,

$$\begin{aligned} \frac{W}{2a} &= \left(\frac{2\pi\sin^2\theta}{3(\theta - \sin\theta\cos\theta)} \frac{f(2a)}{U} \right)^{1/2} \qquad (\theta < \pi/2), \\ &= \left(\frac{2\pi}{3(\theta - \sin\theta\cos\theta)} \frac{f(2a)}{U} \right)^{1/2} \qquad (\theta > \pi/2). \end{aligned} \tag{4.30}$$

Figure 4.15 shows a comparison of Equation (4.30) with the high speed, hot-target data of Figure 4.11. Bead formation begins at about $f(2a)/U = 0.6$, consistent with Equation (4.25). From the height and base radius of the separate droplets deposited at $f(2a)/U = 0.43$ we deduce a solidification angle of $53^\circ \pm 3^\circ$. This value $\theta = 53^\circ$ provides a good fit between Equation (4.30) and the data for $W/2a$, which has an error of about ±8%. From the average heights and widths of the beads above the coalescence threshold we obtain $\theta = 57^\circ \pm 3^\circ$, also in adequate agreement. The results are thus consistent with our model, which is based on the assumption that the solidification angle is a property of the materials and temperatures involved.

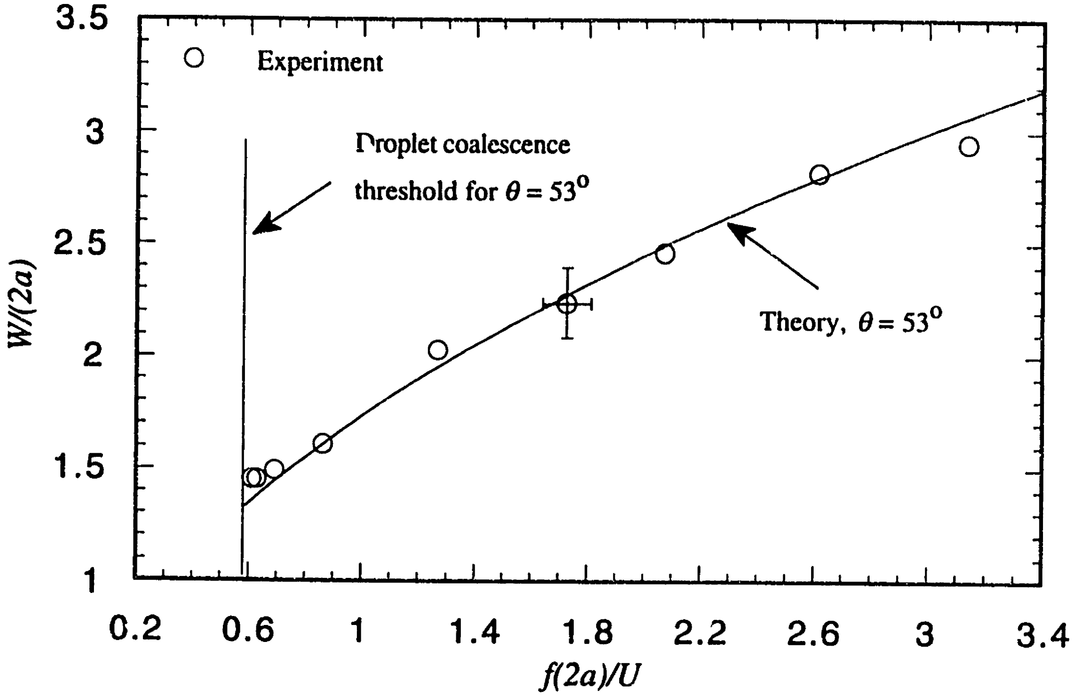

Figure 4.15. Bead width in sweep deposition: experiment against theory for the high speed, hot target data of Figure 4.11.

The good agreement in Figure 4.15 appears to result from the high target temperature and high frequencies, which provide conditions such that the beads have enough time to fully spread to a quasi-equilibrium state before they begin to solidify. Figure 4.16 shows a comparison of Equation (4.30) with the low-speed, colder-target data of Figures 4.12-4.13 and also with another data set taken at the same low target temperature (45°C) but high sweep speed and correspondingly higher frequencies. For both these data sets the separate-droplet data give a solidification angle $\theta = 81.5^{\circ} \pm 3^{\circ}$. The high-speed data are consistent with this value and Equation (4.30) at low $f(2a)/U$, but begin to fall below Equation (4.30) at dimensionless frequencies higher than about 1.8. The low-speed data agree only at the

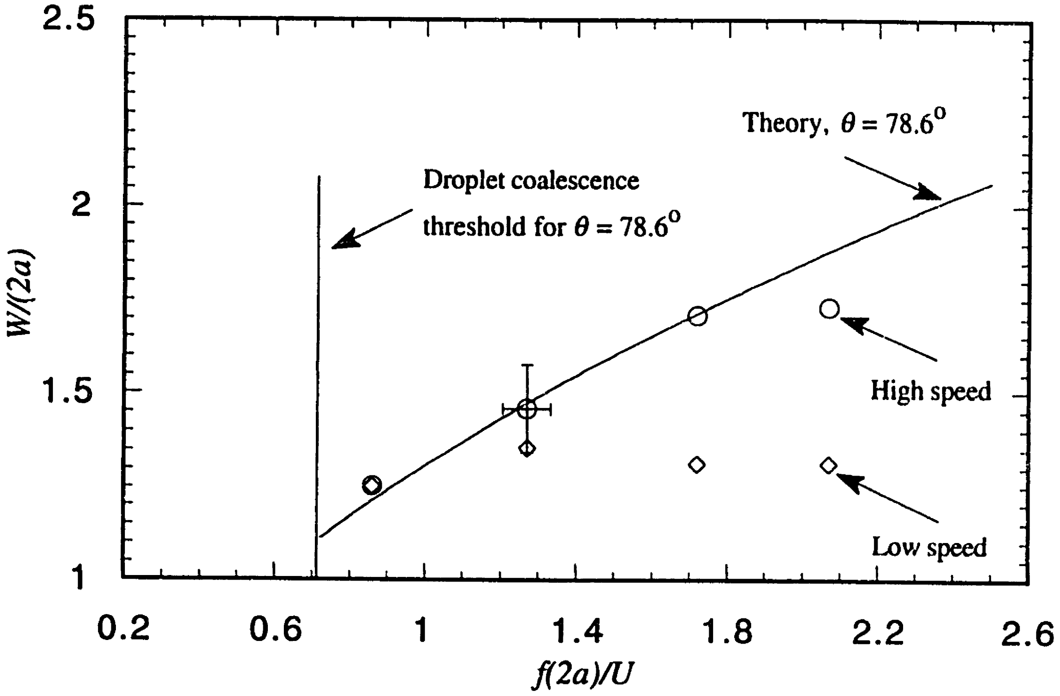

Figure 4.16. Bead width in sweep deposition: experiment against theory for cold targets. The lower speed data are that of Figures 4.12 and 4.13. Candelilla wax on plexiglas.

first data point above the bead-formation threshold, and thereafter fall below the equation and level off to an approximately constant maximum width W. The primary reason for the discrepancy becomes apparent from an examination of Figures 4.12 and 4.13: the base width of the bead does not seem to increase much beyond the base radius of the separately deposited droplets as the frequency is increased. This suggests that the lateral advance of the bead's contact line has been arrested by freezing and the bead has grown upward, swelling over the arrested contact line. Our model thus tends to break down at low sweep speeds (low frequencies) and with highly subcooled targets. Note that the target subcooling $T_f - T_a$ is twice as high in Figures 4.12 and 4.13 as in Figure 4.11.

The instability which becomes apparent at the higher values of $f(2a)/U$ in Figures 4.12 and 4.13 appears to be related to the Rayleigh instability of cylindrical liquid shapes, which has a fastest-growing wavelength of 9.02 times the cylinder radius (Chandrasekhar 1981). If we identify the "radius" in the Rayleigh instability with the radius of curvature of the melt bead, as given by Equation (4.28), we obtain a fastest-growing wavelength Λ of

$$\frac{\Lambda}{b}=\frac{4.51}{\sin\theta}, \tag{4.31}$$

where b is the bead's base width. This is in rough agreement with the data of Figures 4.12 and 4.13. For example, at $f(2a)/U = 2.62$ we observe $\Lambda/b \approx 7$. The appropriate contact angle during the bead's liquid state is open to some question, since the bead's base has begun to freeze, but its effective value is clearly larger than 90°. Equation (4.31) is, of course, an order of magnitude estimation. The identification of R_b with the radius in Rayleigh's analysis is an *ad hoc* step. Unlike Rayleigh's cylinder, our bead has contact lines with the solid surface which may hang up due to freezing, and the instability analysis will take a different form from Rayleigh's. The instability is prominent in Figures 4.12 and 4.13 because the contact line freezes and the liquid bulges out over it, leaving itself in a state more prone to instability than the low contact angle profile of the beads in Figure 4.11. This suggests that the instability is promoted by larger contact angle (lower target temperature) and/or by contact line freezing (lower target temperature, lower sweep speed, and lower frequency).

4.6 Repeated Sweep Deposition

A "wall" may be built by repeatedly traversing a droplet generator, which is dispensing droplets at a frequency f, over a flat target at a speed U. Figure 4.17 shows this repeated sweep deposition process, recorded with the help of strobe lighting.

Figure 4.18 shows a "wall", about 1500 μm tall and 65 μm thick, built by repeated sweep deposition at speed $U = 0.84$ m/s and deposition frequency $f = 13.9$ kHz, which correspond to $f(2a)/U = 0.83$. The melt in this case was candelilla wax, and its temperature was 100°C. The building rate was 10.8 cm^2 of wall per minute. The frequency in repeated sweep deposition can be very high, much higher than that in dropwise columnar deposition, because the time available for solidification is controlled by the interval between sweeps rather than by the deposition frequency. It is important, however, to keep $f(2a)/U$ somewhat above the critical value $F(\theta)$ of Equation (4.25). The exact value of $f(2a)/U$ for forming a "smooth wall" depends on the deposition frequency, the melt and ambient temperatures, and the melt properties. At too low values, the microdrops will not form a continuous bead, and structural irregularities will soon arise and amplify as the subsequent layers are laid down, while at too high values, instabilities tend to occur. The Rayleigh-like bulge instability is one of these, but we have also identified others. For example, if the droplet deposition line executes a small-amplitude harmonic oscillation in the horizontal plane, and this oscillation has a different phase on every sweep, a braid-like structural instability will appear and tend to grow as the wall grows, even if the amplitude of the oscillation is smaller than the droplet diameter.

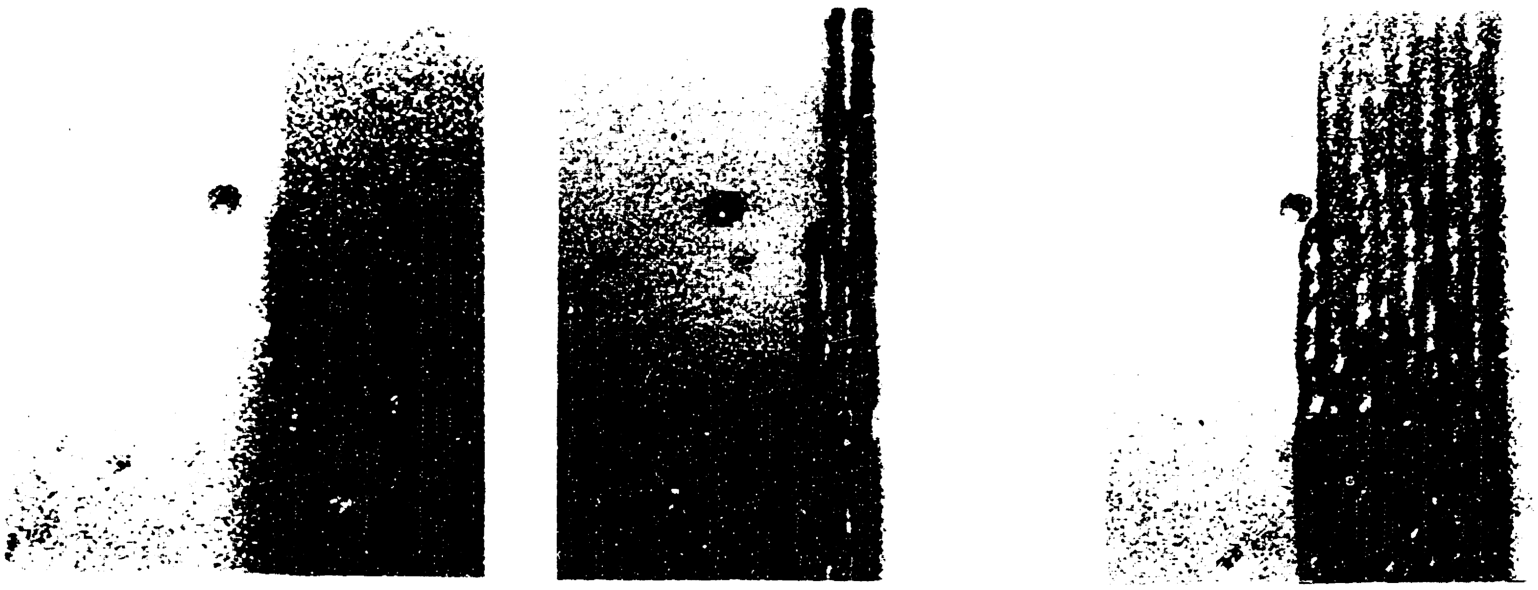

Figure 4.17. A "wall" being built up by repeated sweep deposition.

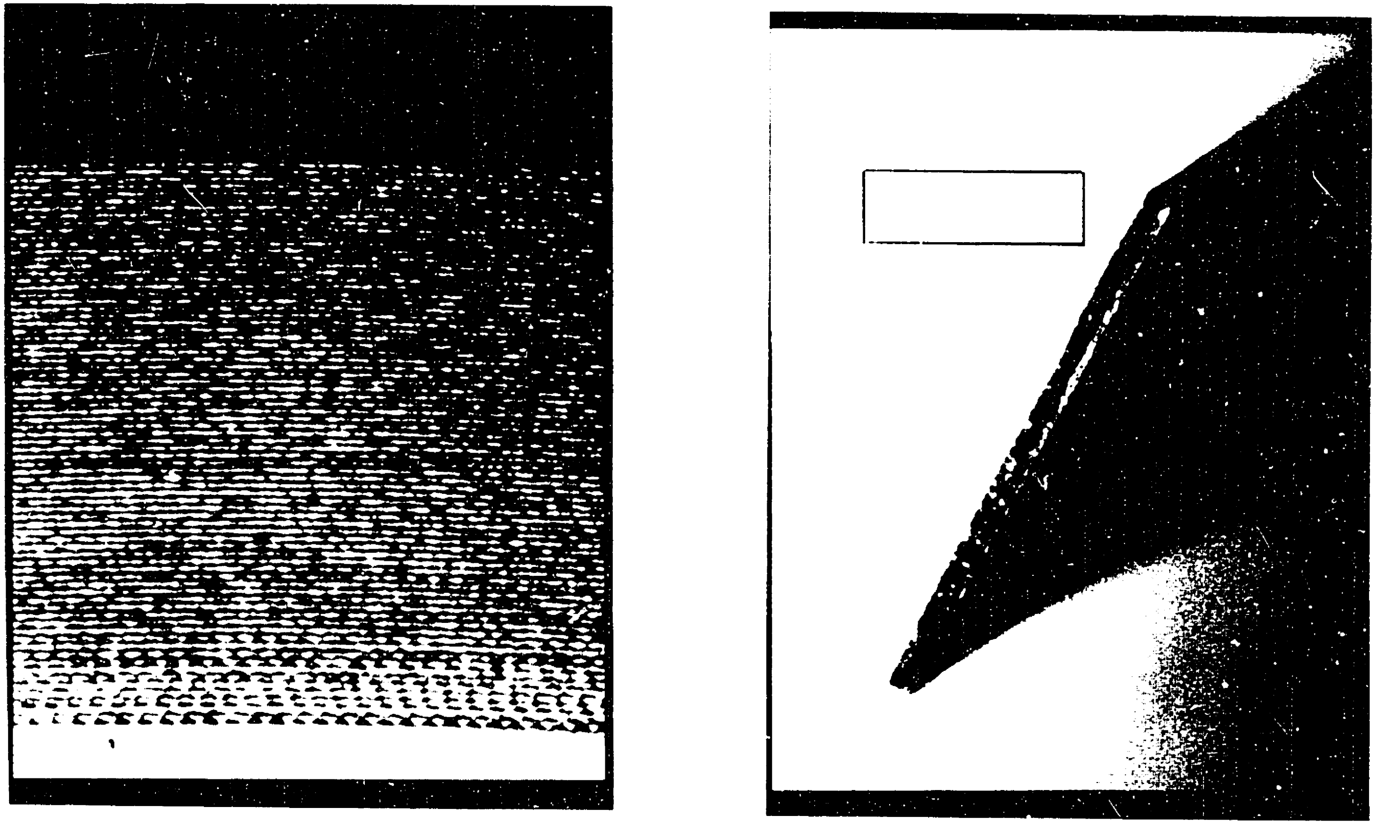

Figure 4.18. Wall built by repeated sweep deposition. Candelilla wax, $T_o = 100^oC$, $T_a = 43^oC$. At right is a view in perspective after the wall was cut. Rectangle: 200 μm x 600 μm.

Chapter 5

SOLIDIFICATION ANGLE OF MOLTEN DROPLETS DEPOSITED ON A SUBCOOLED TARGET

5.1 Introduction

The solidification angle is a very important parameter since it determines the shapes of the structures which are formed by deposition of molten microdrops (see Section 4.1). When a molten microdrop is deposited on a subcooled solid surface, it spreads at first like a liquid drop. The spreading of a molten drop, however, is a very complicated process because it involves both flow and solidification (see Chapter 1). The whole process occurs under thermal nonequilibrium conditions, with the molten drop superheated and the target surface subcooled. The moving contact line will freeze or stop moving as it reaches a state of mechanical equilibrium, and then the whole drop will solidify due to heat transfer from the melt to the solid substrate as well as to the ambient air.

To understand this complex problem, we first study the spreading of simple isothermal liquid droplets on a flat solid surface based on Hoffman's results (see Appendix B), then investigate experimentally how small spheres of solid wax melt, spread, and solidify on a flat solid surface, and last examine melt droplets impacting and spreading on subcooled target surfaces.

5.2 Small Spheres of Solid Wax Melting, Spreading, and Solidifying on Flat Solid Surfaces in a Temperature-controlled Oven

When a molten drop spreads on a subcooled solid surface, one important thing is that the whole process occurs under thermal nonequilibrium conditions (see Section 4.1). To empirically study the contact angle of wax under thermal equilibrium conditions, small solid spheres of wax (candelilla) were heated on a solid surfaces (plexiglas in this case) at varied temperatures in an oven. The oven temperature was kept at given point for a while to let the system reach thermal equilibrium condition. The solid wax spheres melted and spread on the solid surfaces, and the contact angle decreased during the spreading process and finally reached an equilibrium contact angle corresponding to the oven temperature. This final state was similar to that of a pure liquid drop sitting in an isothermal environment on a solid surface. The oven temperature was then decreased slowly to room temperature to allow the molten drop to solidify, and the solidification angle was determined from the diameter of the solidified drop and the drop volume. The whole process was also monitored through the oven window by the video system and no receding of the contact line was observed as the oven temperature was slowly decreased from 90°C to room temperature. Table 5.1 gives some results of measurement. The solidification angles obtained at thermal equilibrium conditions are smaller than that obtained at nonequilibrium conditions (see Section 5.3).

At thermal equilibrium conditions ($T_o = T_t = T_a$), a molten drop will stop spreading when the contact angle reaches the equilibrium contact angle; however, at thermal nonequilibrium conditions (same T_o, but lower T_t), the moving contact line of the molten drop may freeze during spreading due to the heat transfer to the target as well as to the ambient air, that is, for the same melt temperature T_0, the solidification angle will be greater than the solidification angle obtained at thermal equilibrium conditions.

Table 5.1. *Solidification angles of candelilla wax on a plexiglas surface, obtained at thermal equilibrium conditions*

Oven temperature T (°C)	Solidification angle θ (deg)
75	15
88	8.7
100	8.0

5.3 Melt Droplets Impacting and Spreading on Target Surfaces

5.3.1 Single Molten Droplets Impacting and Spreading on Target Surfaces

In Sections 3.1 and 4.1 we showed the impact of a single molten droplet of candelilla wax on a plexiglas surface (Figure 3.1). After the molten droplet makes contact with the target surface, it spreads on the surface and then solidifies. In Figure 3.1, the solidification angle is about 85°.

Based on the analysis in Section 4.1, the solidification time for one of our molten wax droplets is about 17 ms. The entire spreading process takes only about 40 μs which is much shorter than the solidification time. This means that the molten droplet typically stops spreading when it reaches some apparent static contact angle, and then solidifies on a much larger timescale. The solidification angle is in this case equal to the apparent static contact angle. Note that the apparent static contact angle (and hence the solidification angle) is not an equilibrium property since the droplet spreading occurs under thermal nonequilibrium conditions, with the droplet superheated and the target surface subcooled.

Table 5.2. *Solidification angles of single melt droplets on a plexiglas target*

Candelilla wax, melt temperature T_0 = 90°C.

Target temperature T_t (°C)	Solidification angle θ (deg)
30	85
45	81
58	53
60	40

Table 5.2 shows some data of the solidification angle of single droplets (candelilla wax) obtained at different temperatures. Comparing them with the data obtained at thermal equilibrium conditions (Table 5.1) we can see that solidification angles obtained at thermal nonequilibrium conditions are larger.

5.3.2 Growing Drops Spreading and Solidifying on a Flat Surface

To identify the parameters on which the solidification angle depends, we investigated growing molten drops spreading and solidifying on a subcooled target surface. A novel method was devised to study the solidification angle and the freezing of an advancing melt contact line: the continuously fed drop method, in which a certain number of superheated

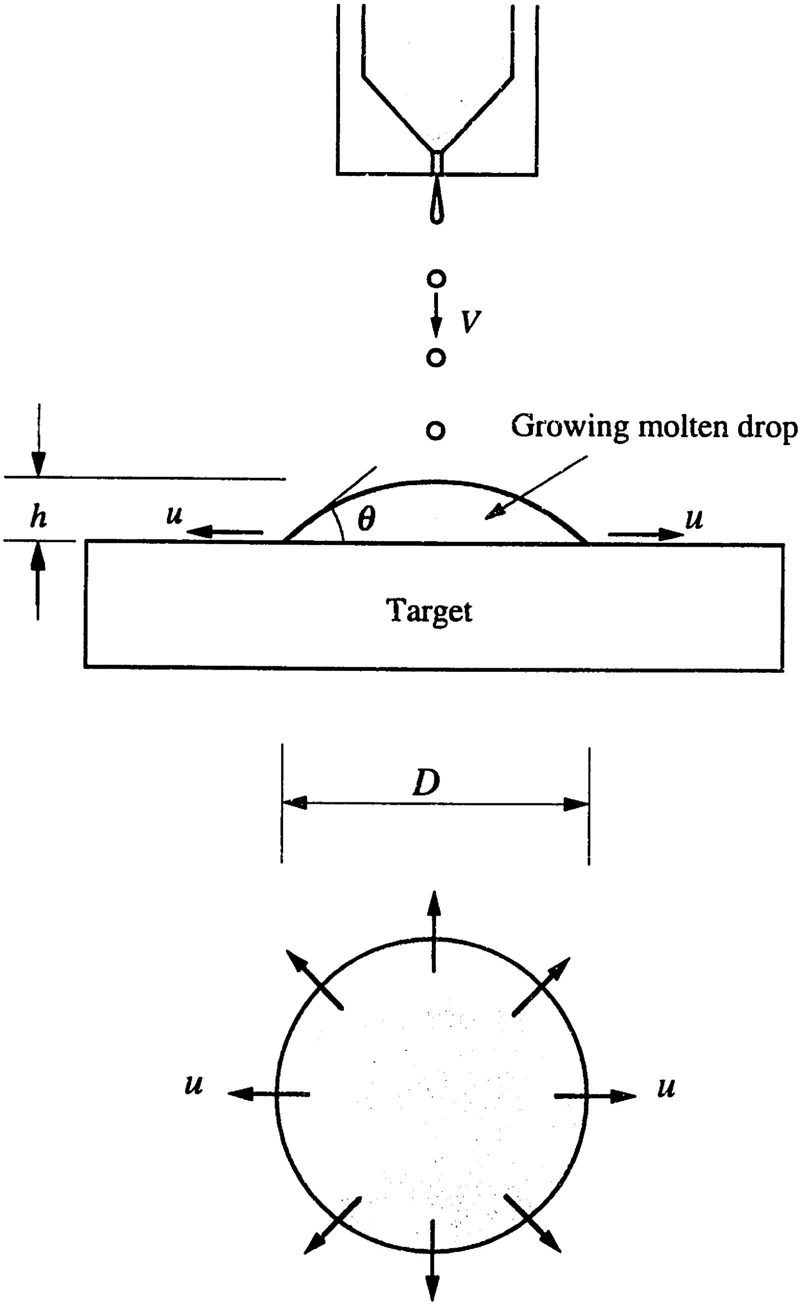

Figure 5.1. A growing molten drop spreading on a solid surface.

droplets were deposited on a subcooled target at a frequency which was so high (typically of the order of 10 kHz) that the droplets coalesced into a growing liquid drop.

Figure 5.1 shows a growing drop spreading on a subcooled solid surface. The solid target was stationary relative to the droplet generator. Since the deposition frequency was so high, there was not sufficient time for a droplet to solidify before the next one arrived. The impinging droplets coalesced into a sessile drop which was close to a spherical cap in shape and grew as it was continuously fed by the arriving droplets. The deposition was stopped after N droplets, and the shape of the deposit examined after complete solidification.

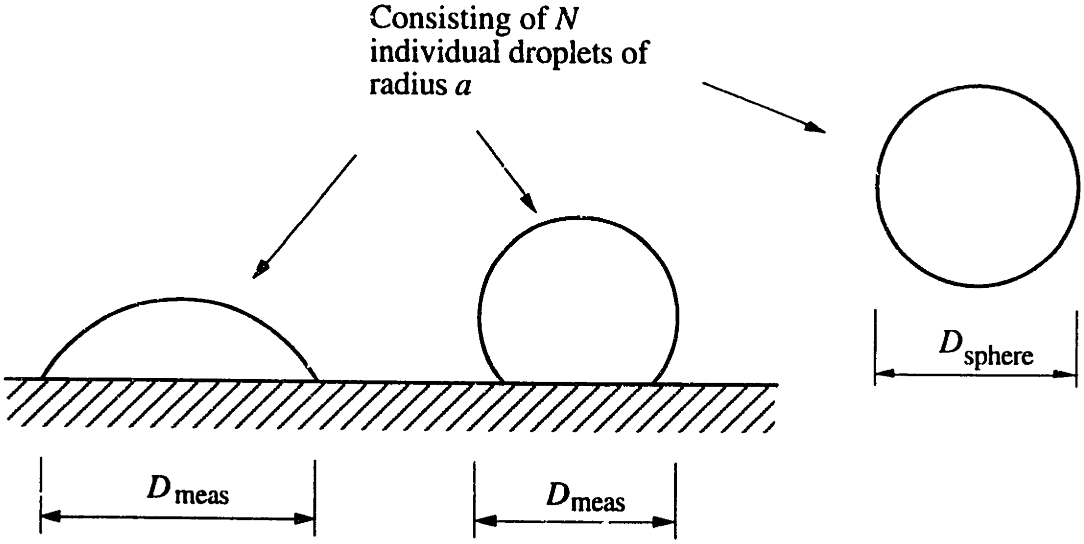

$$\frac{4}{3}\pi\left(\frac{D_{sphere}}{2}\right)^3 = N\frac{4}{3}\pi a^3$$

Figure 5.2. Shape parameters, D_{meas} and D_{sphere}, and their relationship.

For given melt and target materials, the major experimental parameters in our experiments are the deposition frequency and the melt and target temperatures. To examine the effects of each parameter on the solidification angle, we systematically varied one of them while keeping the others fixed. Here we use two shape parameters: D_{meas} and D_{sphere}. D_{meas} is the diameter of the deposited drop, as seen from directly above the target, that is, as measured at the widest position. D_{sphere} is the calculated diameter of a sphere which has the same volume as that of the deposited drop (Figure 5.2). For a deposited drop which consists of N droplets and has volume $N(\frac{4}{3}\pi a^3)$, D_{sphere} is equal to $2aN^{1/3}$, a being the radius of a single droplet. If the shape of the deposited drop is a spherical cap with solidification angle θ, from mass conservation (the same way as that for Equations (4.2) and (4.3)) we have

$$\frac{D_{\text{meas}}}{D_{\text{sphere}}} = \left(\frac{4\sin^3\theta}{(1-\cos\theta)^2(2+\cos\theta)}\right)^{1/3} \qquad \theta < 2/\pi \qquad (5.1a)$$

and

$$\frac{D_{\text{meas}}}{D_{\text{sphere}}} = \left(\frac{4}{(1-\cos\theta)^2(2+\cos\theta)}\right)^{1/3} \qquad \theta > 2/\pi. \qquad (5.1b)$$

Figures 5.3 shows the results obtained at different target temperatures. The deposition frequency is 10 kHz, the melt temperature is 90°C, and the target temperatures are 34°C and 60°C, respectively. Both the melt and the target are candelilla wax with melting point of 70°C. In the case of the lower target temperature, the ratio of D_{meas} to D_{sphere} is almost constant (about 1.5) at small droplet numbers, i.e. at small sessile drop volume, then decreases with the increasing of the droplet number, and finally becomes constant (1.0) after the droplet number is larger than 100.

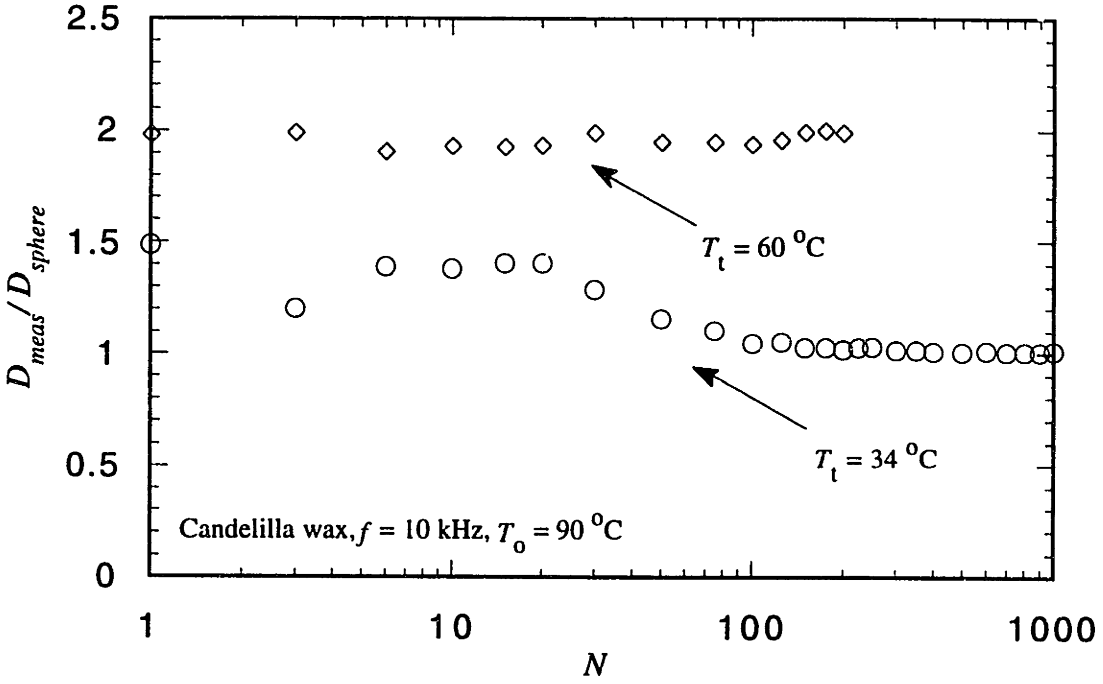

Figure 5.3. The ratio of D_{meas} to D_{sphere} against droplet number N at different target temperatures. Candelilla wax, $T_0 = 90$°C, $f = 10$ kHz.

Note that the number N of droplets deposited is actually a measure of the time t. Larger N corresponds longer time because for a given deposition frequency f, $t = N/f$. The contact line speed u of a growing drop is equal to $\frac{\mathrm{d}r_b}{\mathrm{d}t}$, r_b being the radius of the contact line. To estimate u, we assume that the shape of the drop is a spherical cap, and from mass conservation we have

$$u = \frac{\mathrm{d}r_b}{\mathrm{d}t} = \frac{a}{3}\left(\frac{4\sin^3\theta}{(1-\cos\theta)^2(2+\cos\theta)}\right)^{1/3}\frac{f}{N^{2/3}} \qquad (5.2a)$$

or

$$u = \frac{\mathrm{d}r_{\mathrm{b}}}{\mathrm{d}t} = \frac{a}{3}\left(\frac{4\sin^3\theta}{(1-\cos\theta)^2(2+\cos\theta)}\right)^{1/3}\frac{f^{1/3}}{t^{2/3}}. \tag{5.2b}$$

In the case of the higher target temperature, $D_{\mathrm{meas}}/D_{\mathrm{sphere}}$ is almost constant over a wider range of droplet number, indicating that the solidification angle is independent of N in that range.

For low target temperature, the solidification time is shorter than that for high target temperature, so the ratio of D_{meas} to D_{sphere} is smaller. For high target temperature, the

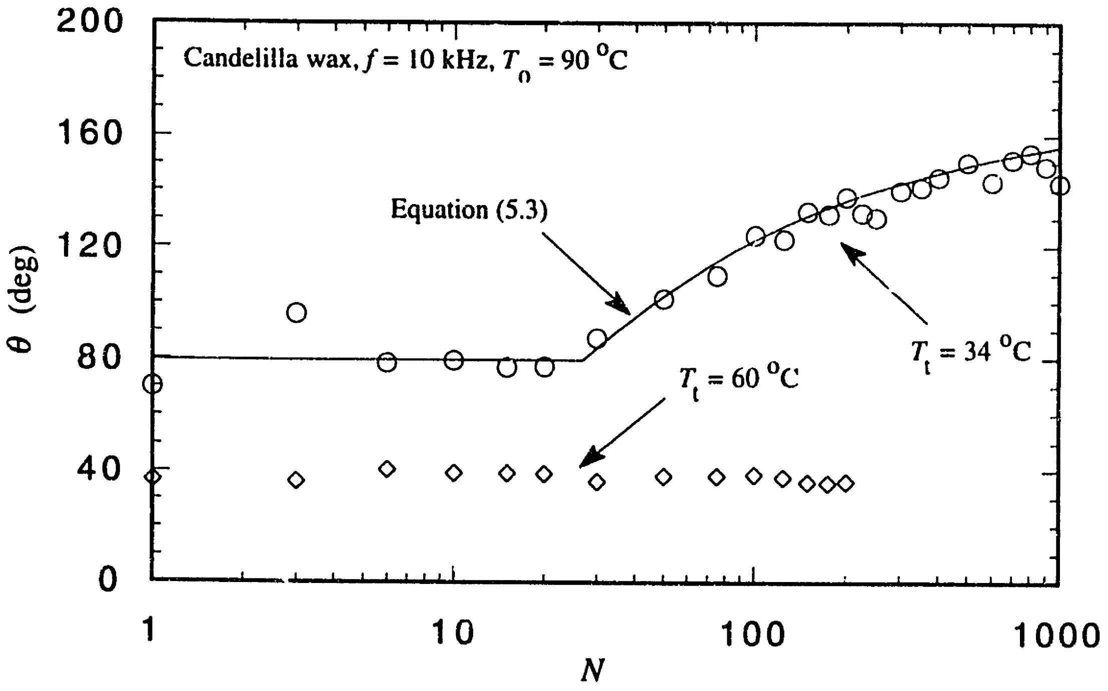

Figure 5.4. Solidification angle θ against droplet number N. From the same experiment as that for Figure 5.3.

moving contact line of a growing drop will not freeze before the droplet delivery stops, unless the droplet number is large (large time), and hence the ratio of D_{meas} to D_{sphere} is constant to higher values of droplet number N. In the case of low target temperature, the ratio of D_{meas} to D_{sphere} approaches 1 at large droplet number because the base diameter of the growing drop is small (i.e. the moving contact line freezes in a short time, long before droplet delivery stops), and the shape of the deposited drop is close to a sphere. Figure 5.4, which shows how the solidification angle changes with the droplet number N, was obtained from the same experiment as that for Figure 5.3.

The shape of a growing drop varies with the number of individual droplets, and there are two stages (except for the very beginning). In the first stage, the growing drop spreads on the solid surface with a constant apparent contact angle, θ_0, and in the second stage, the apparent contact angle increases with increasing droplet number due to the frozen or near-frozen contact line (Figure 5.5). The higher the target temperature, the longer the first stage lasts.

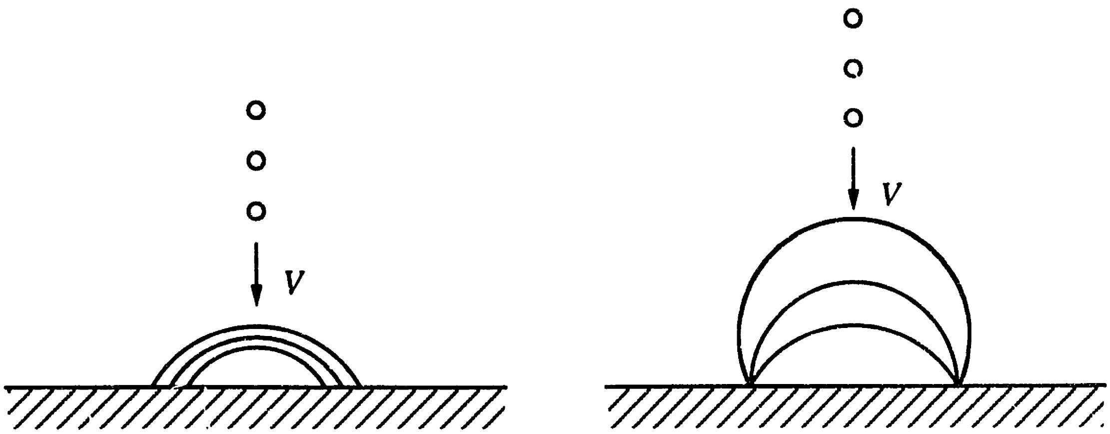

Figure 5.5. Two stages in growing drop spreading.

Assuming contact line freezing occurs abruptly at N^*, we can make a simple model to predict the solidification angle θ versus the droplet number N. If N individual droplets with (solidified) volume $N(\frac{4}{3}\pi a^3)$ are deposited as a spherical cap with solidification angle θ (Figure 5.2), from mass conservation we obtain

$$N = \left(\frac{r_b}{a}\right)^3 \left(\frac{(1-\cos\theta)^2(2+\cos\theta)}{4\sin^3\theta}\right). \qquad (5.3)$$

For given C_0 and N^* obtained from experimental data, Equation (5.3) gives $r_b{}^*$, here $r_b{}^*$ is the base radius when the contact line freezes. With this $r_b{}^*$ and Equation (5.3), we can predict θ versus N after contact line freezing. The curve in Figure 5.4, for example, is from Equation (5.3) with $\theta_0 = 79^o$ and $N^* = 27$.

To further examine how the apparent contact angle (or shape) of a growing drop changes with the droplet number, that is, time, the whole deposition process was recorded by a microscope objective attached to a video camera and a multifunctional VCR, and examined field by field. The period between two successive fields is 1/60 sec. In this way, one can find out at what time the moving contact line begins to freeze. Figure 5.6 shows the pictures of a growing drop of microcrystalline wax (with a melting point of 91°C) spreading on a subcooled solid surface of the same wax. Since the pictures were taken with a fiber optic illuminator (not a stroboscope), the arriving droplets show as a vertical blurry line in the pictures. The wax melt and target temperatures are 115°C and 75°C, respectively. The deposition frequency f is 2.5 kHz and the final droplet number N is 1,000, so the total deposition time is N/f = 1000/2500 = 0.4 sec. The growing drop spreads with a constant apparent contact angle (about 52.5°) until field 8 when the moving contact line begins to freeze and the apparent contact angle increases slightly. The contact

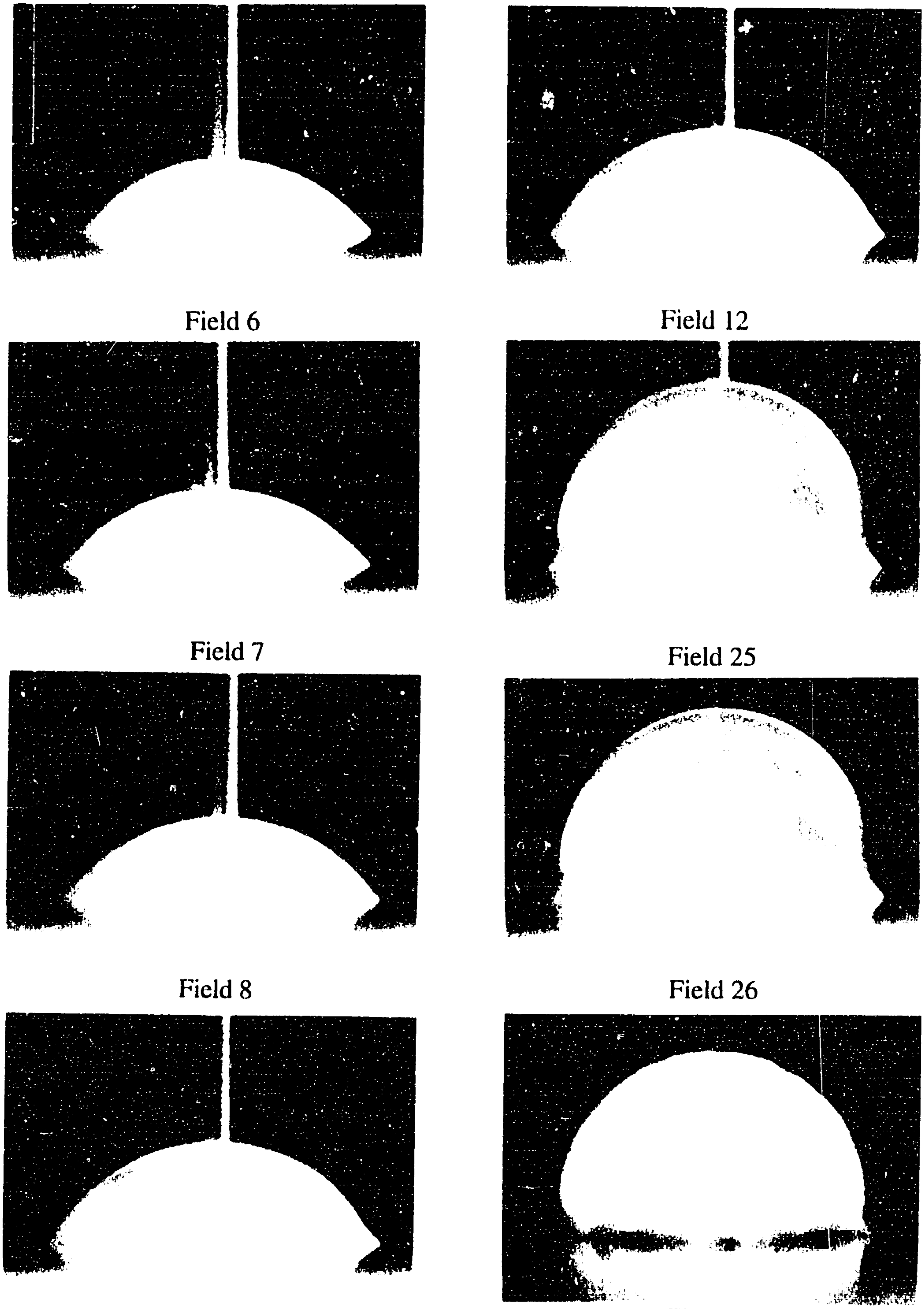

Field 6

Field 12

Field 7

Field 25

Field 8

Field 26

Field 11

Field 400

Figure 5.6. A growing drop spreading on a solid surface of its own kind. Microcrystalline wax, T_0 = 115°C, T_t = 75°C, f = 2.5 kHz.

line is arrested by freezing at field 11, and the apparent contact angle increases significantly since the droplet delivery still continues. The droplet delivery stops at field 26. The last picture in Figure 5.6 shows the solidified drop.

In Figure 5.6 the droplet delivery continues after the contact line is frozen. If the droplet delivery stops before the contact line is frozen, the value of the solidification angle will be different from the apparent dynamic contact angle of the melt during spreading. Figure 5.7 shows the pictures of a growing drop of candelilla wax (with a melting point of 70°C) spreading on a subcooled solid surface of the same wax. The wax melt and target temperatures are 115°C and 60°C, respectively. The deposition frequency *f* is 10 kHz and the final droplet number *N* is 1,000. In this case, the droplet delivery stops before the contact line freezing. We see that the molten drop spreads further on the target after the droplet delivery stops, and then solidifies. The solidification angle is about 45°, but the dynamic apparent contact angle (i.e. before droplet delivery stops) is larger (57°) due to the advance velocity of the contact line. This is the same phenomenon as that found in the spreading of a simple, isothermal liquid droplet. The method used here can also be used to study the dynamic advancing angle of a liquid droplet spreading on a solid surface.

The pictures (in perspective) in Figure 5.8 were obtained under the same experimental conditions as those for Figure 5.7. We can see that during droplet delivery the growing drop has a dimple at the center where the arriving droplets impact. The dimple disappears as soon as the delivery stops, and the drop becomes an approximately spherical cap which spreads a little further and then solidifies.

From Figure 5.4 we know that the target temperature has a significant effect on the solidification or apparent static contact angle. In order to study whether the deposition frequency *f* has an effect on solidification angle, we conducted another experiment set at the same condition as that in Figure 5.4 except for the deposition frequency. In this case, *f* =

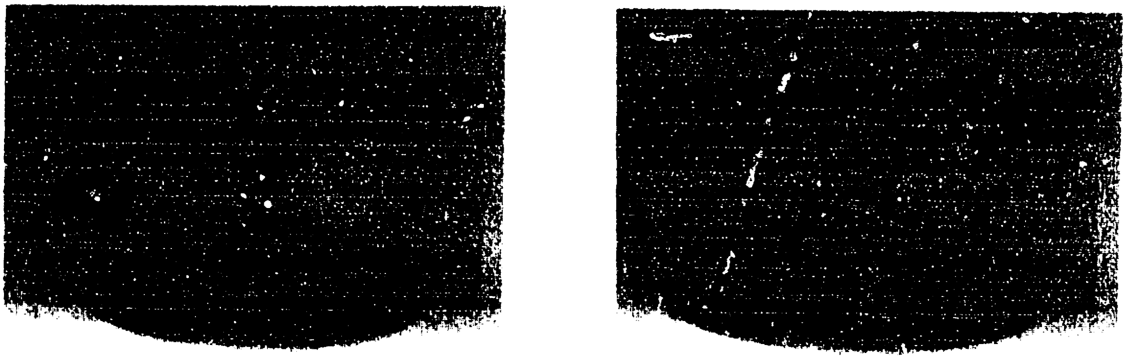

Field 6

Field 7

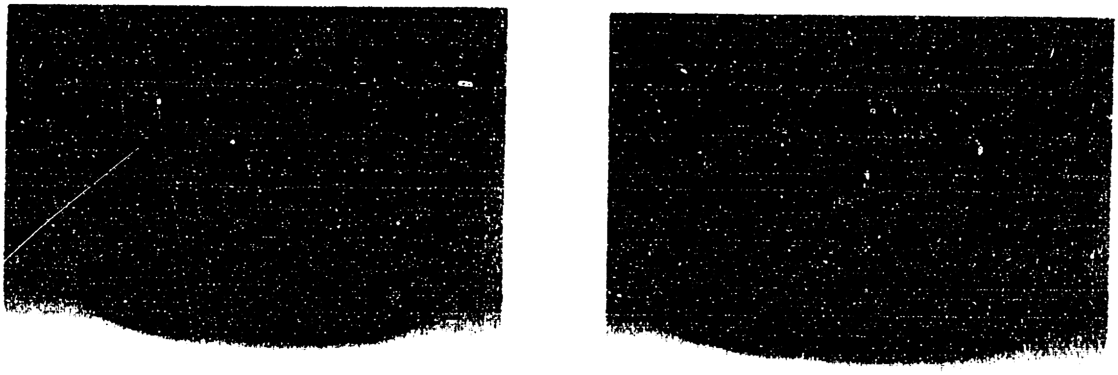

Field 8

Solidified

Figure 5.7. A growing drop spreading on a solid surface of its own kind. Candelilla wax, T_0 = 115°C, T_t = 60°C, f = 10 kHz.

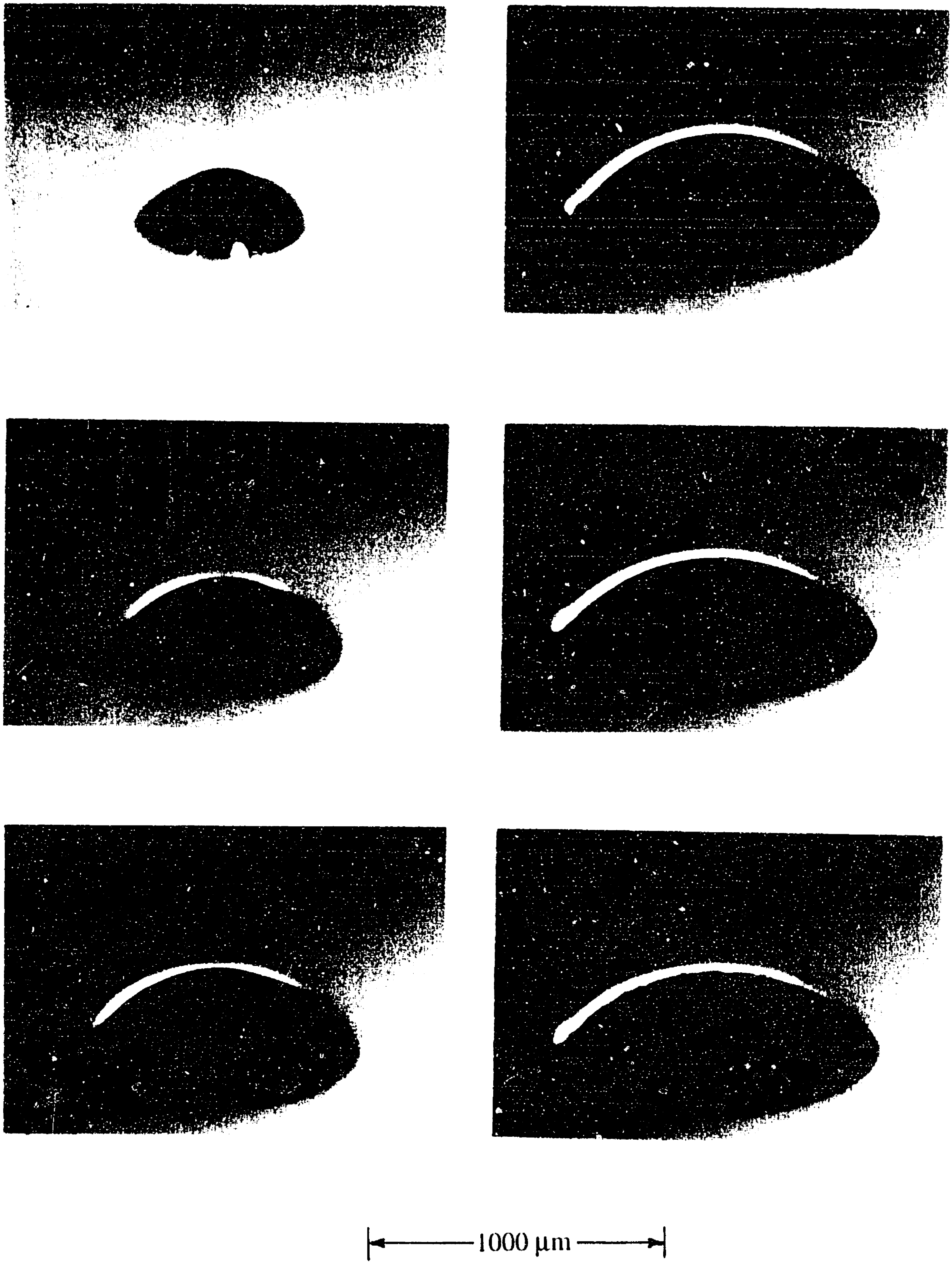

Figure 5.8. Pictures (in perspective) obtained under the same experimental conditions as those for Figure 5.7.

15 kHz; the higher deposition frequency corresponds to higher spreading velocity. Experimental results are given in Figures 5.9 and 5.10. Comparing Figure 5.9 with Figure 5.4, we see that for high target temperature (60°C) the values of solidification angles are almost the same. The deposition frequency (and thus the velocity of the contact line) does not have a significant effect on the solidification angle as long as spreading occurs on a timescale short compared with the solidification time.

Figure 5.11 shows the results obtained at higher melt temperature (115°C), other conditions being the same as that in Figure 5.4. The value of the solidification angle does not change much compared with that at lower melt temperature (90°C), that is, the solidification angle is insensitive to the melt's superheat.

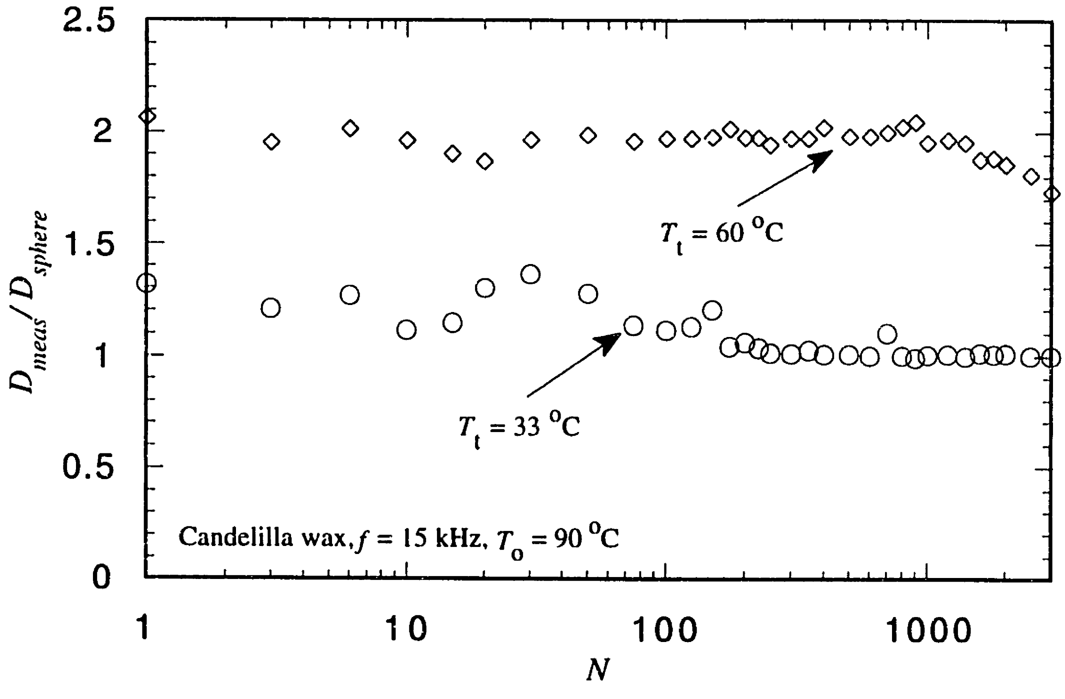

Figure 5.9. The ratio of D_{meas} to D_{sphere} against droplet number N at different target temperatures. Candelilla wax, T_0 = 90°C, f = 15 kHz.

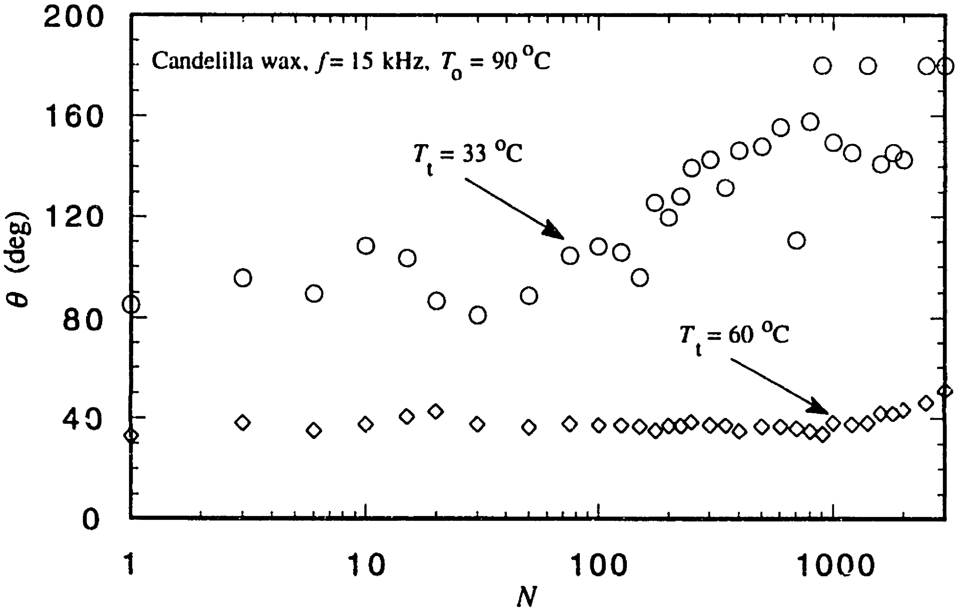

Figure 5.10. Solidification angle θ against droplet number N. From the same experiment as that for Figure 5.9.

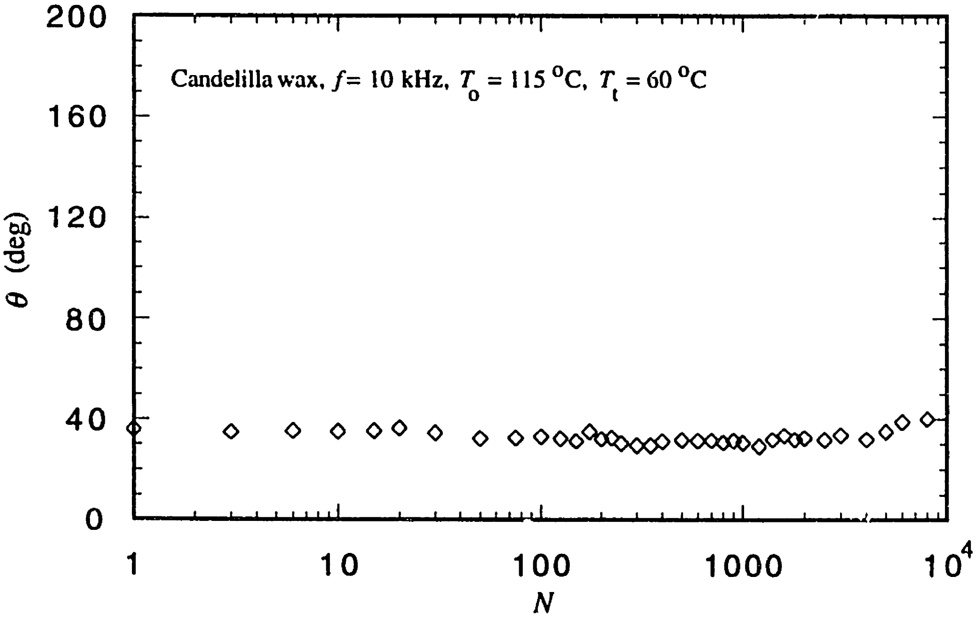

Figure 5.11. Solidification angle θ against droplet number N. Candelilla wax, T_o = 115°C, T_t = 60°C, f = 10 kHz.

From the experiments mentioned above, we know that the deposition frequency and melt temperature do not have significant effects on the solidification angle as long as spreading occurs on a timescale short compared with the solidification time. When the deposition frequency is high enough (i.e. the contact line advance speed is not too small) and the target temperature is sufficiently high, the solidification angle is mainly controlled by the target temperature.

To further investigate how the solidification angle depends on the target temperature, a series of experiments was done with candelilla wax at varied target temperatures as well as droplet numbers. The target temperatures ranged from 36°C to 66°C and the final droplet numbers from 50 to 2,000. For all target temperatures and droplet numbers, the melt temperature was fixed at 115°C and the deposition frequency was 10 kHz. The results of this series of experiments are shown in Figures 5.12 and 5.13. When the target temperature is high enough (higher than 55°C in this case), the solidification angle does not change within the tested droplet number range and varies significantly with target temperatures. For the low target temperatures, the solidification angle increases as the droplet number increases.

From all the experimental results mentioned above, we known that when the contact line advance speed is not too small (high deposition frequencies) and the target temperature is high, the solidification angle is mainly controlled by the target temperature.

If we plot the data in Figure 5.13 in another way, solidification angle versus target temperature, we find that as target temperature approaches the melting point of the wax, the solidification angle approaches zero and the solidification angles for different droplet numbers converge (Figure 5.14).

Similar data were obtained with microcrystalline wax (Figure 5.15).

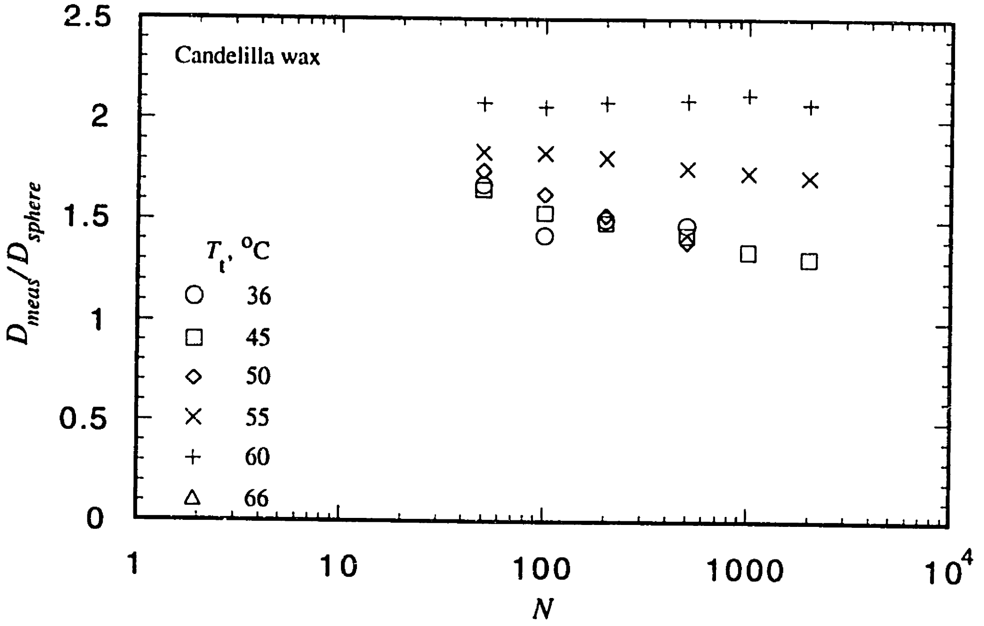

Figure 5.12. The ratio of D_{meas} to D_{sphere} against droplet number N at different target temperatures. Candelilla wax, $T_0 = 115°\text{C}, f = 10$ kHz.

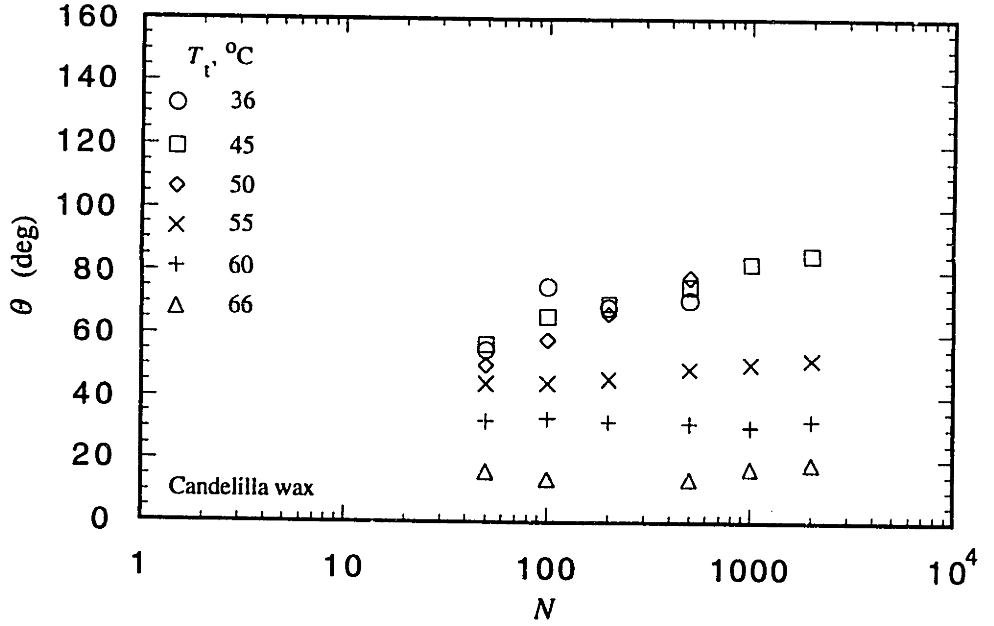

Figure 5.13. Solidification angle θ against droplet number N at different target temperatures. From the same experiment as that for Figure 5.12.

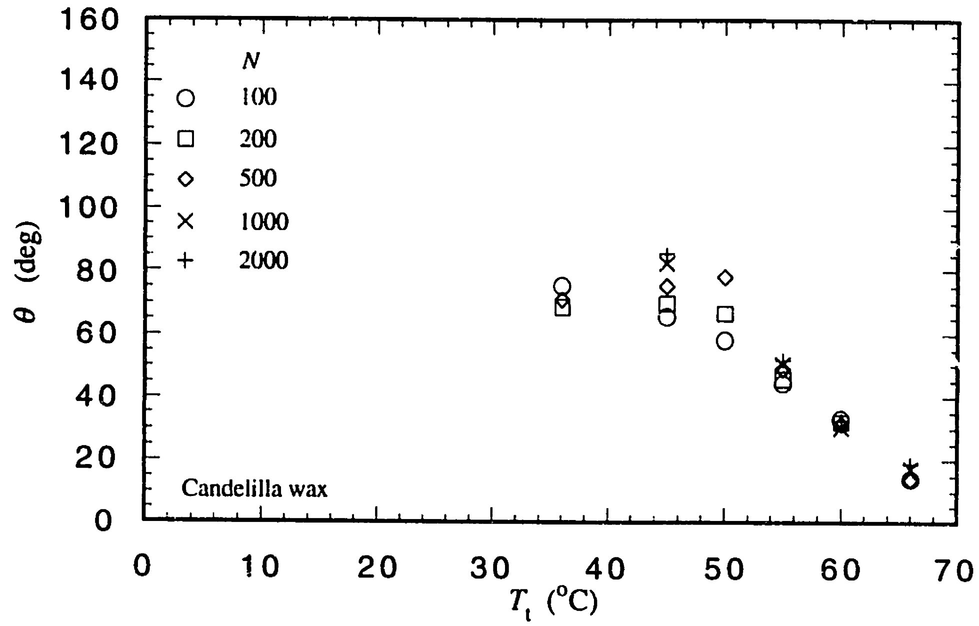

Figure 5.14. Solidification angle θ against target temperature T_t for different droplet numbers. From the same experiment as that for Figure 5.12.

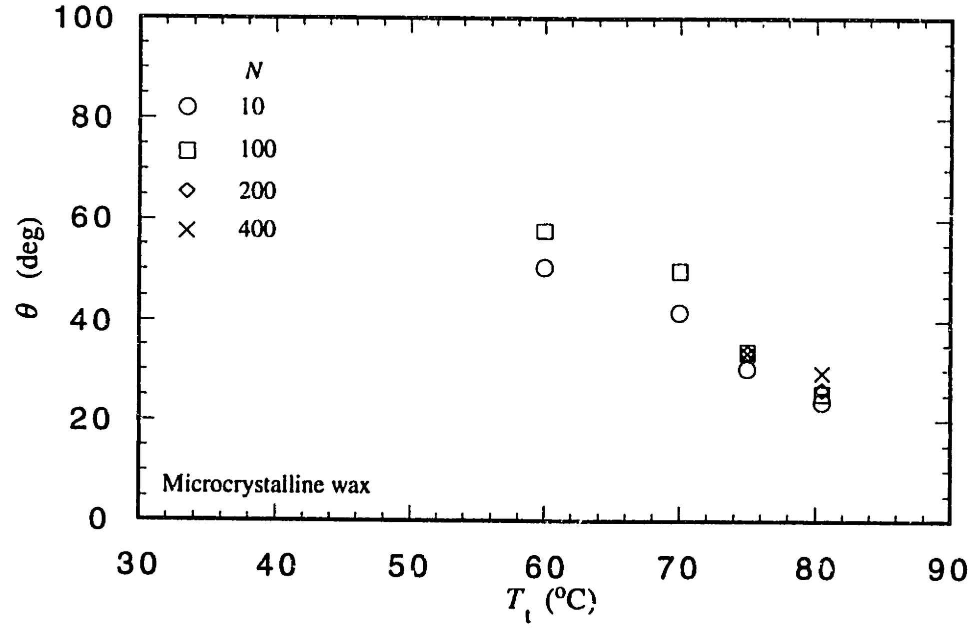

Figure 5.15. Solidification angle θ against target temperature T_t for different droplet numbers. Microcrystalline wax, $T_0 = 115$°C, $f = 10$ kHz.

5.3.3 Growing Drops Spreading on Surfaces of Different Materials

From the previous discussion, we know that the solidification angle is strongly dependent on the target temperature and presumably on the target thermal properties (thermal conductivity, specific heat, and density). We also know that the equilibrium contact angle of a liquid drop on a solid surface varies with the surface properties of the solid material. In this section, we will describe the phenomena observed in experiments of deposition of molten droplets on the solid surfaces of different materials. Two types of experiments on this topic were performed, one designed to investigate the dependence on the thermal properties of targets and the other to investigate the effect of interface conditions.

In the first type of experiment, two different targets were used, plexiglas and aluminum (see Table 2.1 for the properties of these materials). Twenty-five individual molten droplets, candelilla wax in this case, were deposited on these two different targets under the same conditions. The deposition frequencies were high (1,000, 2,500, and 10,000 Hz). Figure 5.16 shows the structures formed on these two targets. The whole burst of 25 droplets coalesced into a spherical drop due to the high deposition frequencies. The shapes of the drops on plexiglas was significantly dependent on the deposition frequency f. Increasing f increased the base radius of the drop (decreased the solidification angle). This can be attributed to the fact that the delivery time of 25 droplets is, in this case, long compared with the contact line freezing time, and the contact line freezes and becomes arrested on its way outward before it can attain the quasi-equilibrium contact angle (also see Section 4.2). For the same deposition frequency, that is, the same delivery time t ($t = N/f$), the structure formed on the aluminum target is significantly different from that on the plexiglas target. Because of the high thermal conductivity of aluminum (204 W $m^{-1}K^{-1}$) which is much higher than that of plexiglas (0.153 W m^{-1} K^{-1}), the moving contact line

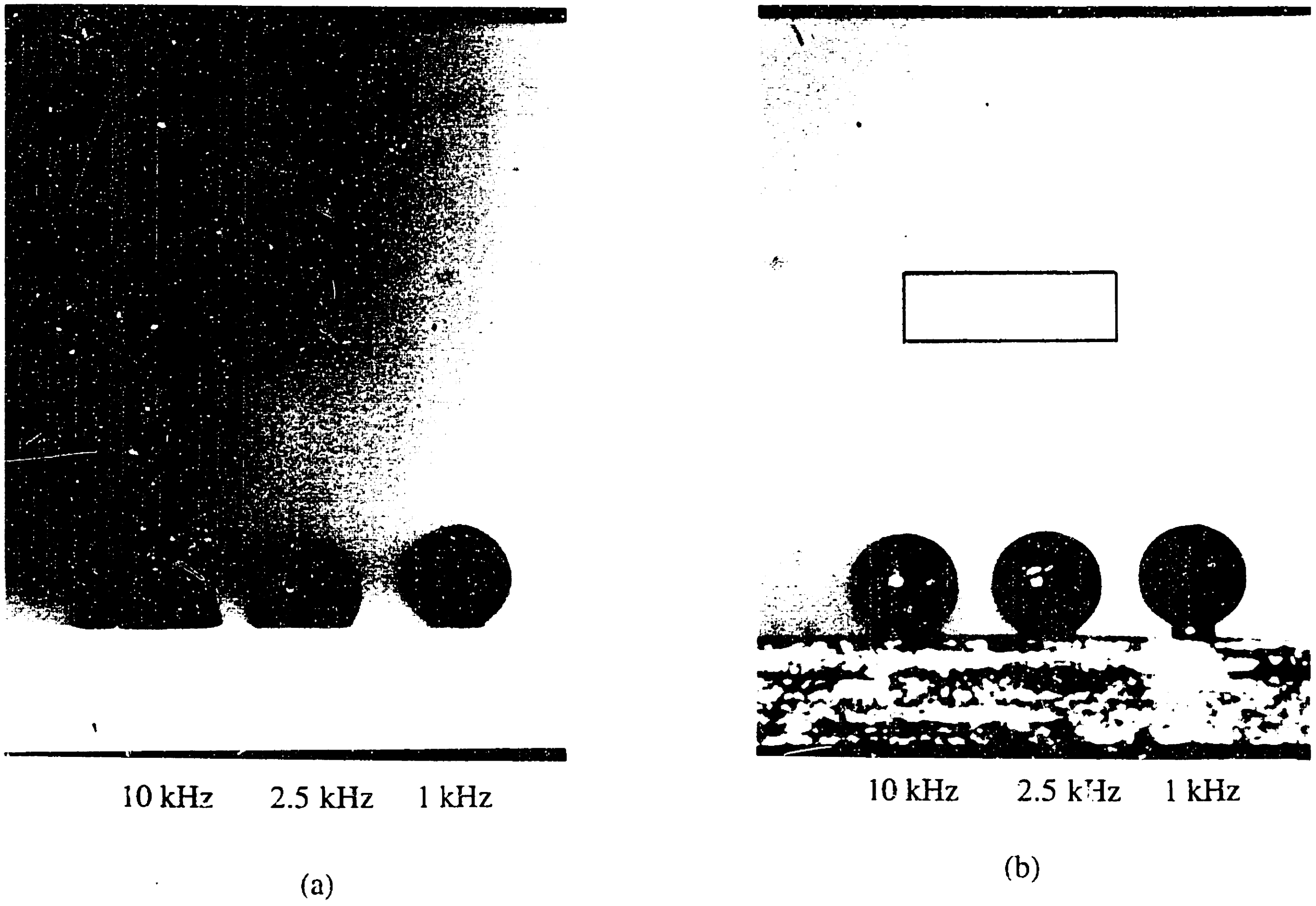

(a)

(b)

Figure 5.16. Structures formed by depositing 25 microdrops at different frequencies: (a) plexiglas target; (b) aluminum target. Candelilla wax, $T_0 = 90^{\circ}C$.

freezes very fast on the aluminum target and the base radius of the formed structure is smaller.

Since the molten drop spreads under thermal nonequilibrium conditions and involves heat transfer and solidification, the target materials would have two factors which influence the solidification angle: surface properties and thermal properties. In the second type of experiment, a glass plate with and without a very thin vapor-deposited coating of gold (about 350 Å thick) was used as the target. The gold coating was chosen in the hope that it would be so thin and its thermal conductivity so high (k = 315 W m^{-1} K^{-1}) that the conditions of heat transfer would be almost the same as those without the coating, that is, for the same target temperature the heat flux to the target with the thin gold coating would be the same as that to the target without gold coating. This is actually an open question, however, as we show below, and further investigation is needed.

The system can be considered as a semi-infinite melt drop spreading on a semi-infinite subcooled glass coated with a thin gold film. The thermal penetration depth $\delta(t)$ in the target is

$$\delta(t) \sim (\alpha t)^{1/2}.$$

Let $\delta(t) = \delta_g$, where δ_g is the thickness of the gold film. The thermal transit time across the gold film is then $t \sim \delta_g^2/\alpha = 9.7\text{x}10^{-6}$ μs, which is much smaller than both spreading and solidification times. This suggests that the thermal effects of this thin gold film might be neglected; however, the question is not fully resolved because we have not analyzed the effects of the horizontal heat flux along the thin coating.

Figure 5.17 shows the glass target used in our experiments on which there are some strips of the thin gold coating. The drop can be deposited either on gold surface or glass surface. It can also be deposited just on the borderline of the gold coating and the glass

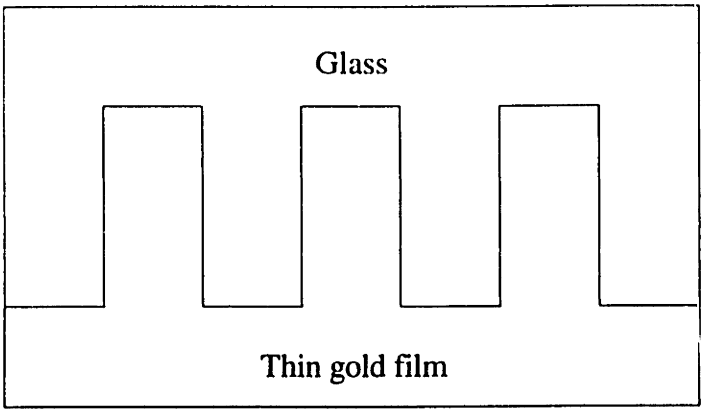

Figure 5.17. Glass target with a thin gold film.

surface. In this case, part of the drop will be spreading on gold and part of it on glass, and the spreading conditions for these two different parts of the drop will be approximately the same except for the surface properties.

In this experiment, we deposited molten droplets of candelilla wax on the target at different target temperatures. The melt temperature was 90°C (20°C above the melting point), the target temperatures were 65°C, 60°C, 44°C and 36°C, respectively, and the deposition frequency was 10 kHz.

Figures 5.18 to 5.20 show some photographs of experimental results which demonstrate that the gold surface film does affect the solidification angle. The target temperature is 65°C for both cases. The diameter of the drop deposited on the gold surface is larger than that on the glass surface (Figure 5.18), and if the drop is deposited so as to straddle the borderline, the radius of the curve of the drop on the gold surface is larger than that on the glass surface (Figure 5.19). The larger diameter implies a smaller local solidification angle.

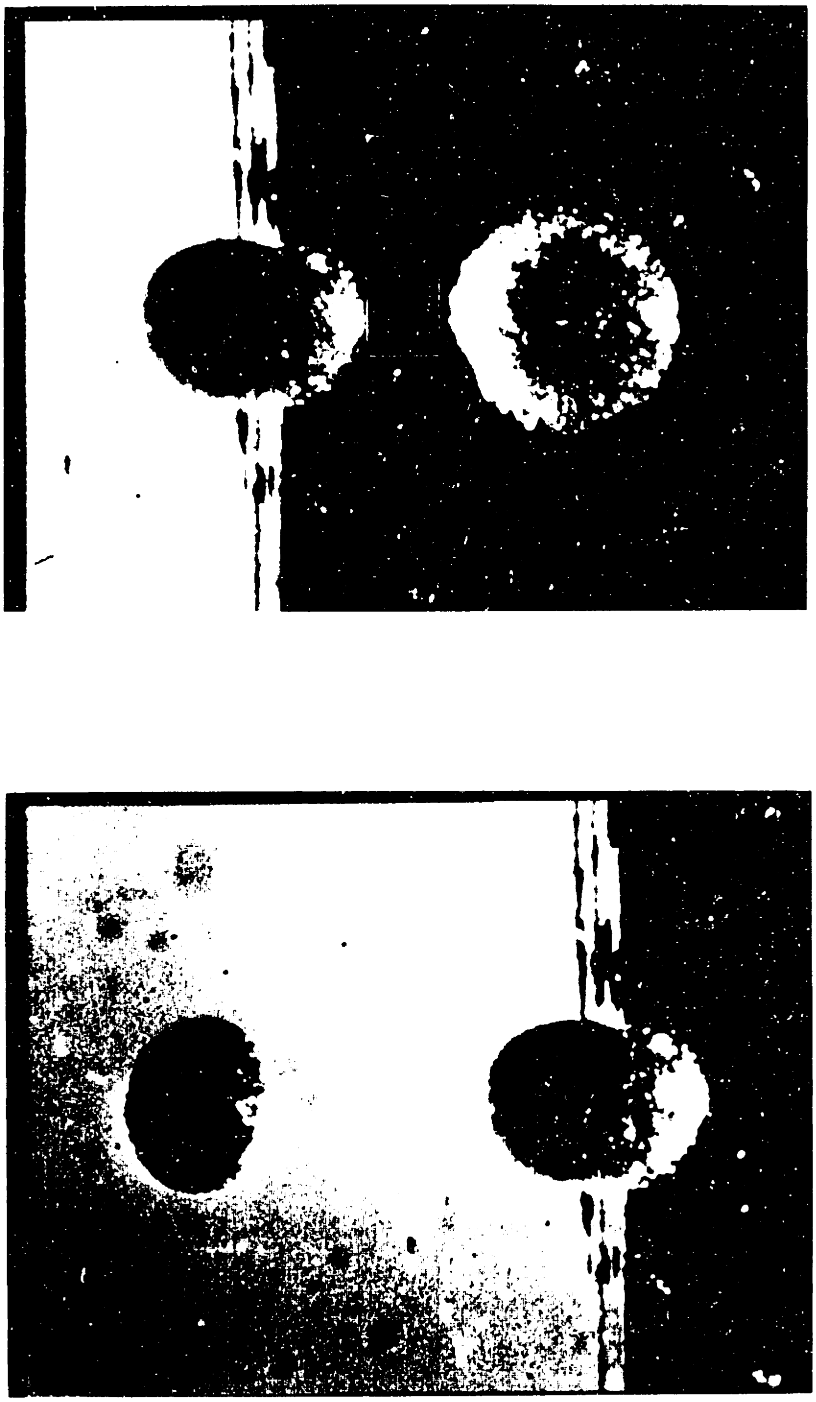

Figure 5.18. Shapes formed by depositing 10 microdrops on the target shown in Figure 5.17. Candelilla wax, T_0 = 90°C, T_t = 65°C, f = 10 kHz. Rectangle: 100 μm x 300 μm.

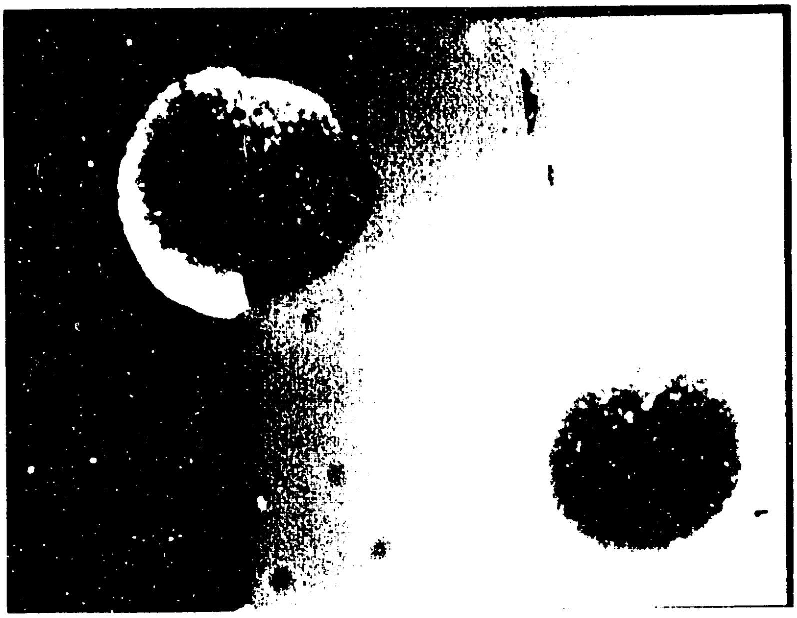

Figure 5.19. Shapes formed by depositing 20 microdrops on the target shown in Figure 5.17. Candelilla wax, T_0 = 90°C, T_t = 65°C, f = 10 kHz. Rectangle: 100 μm x 300 μm.

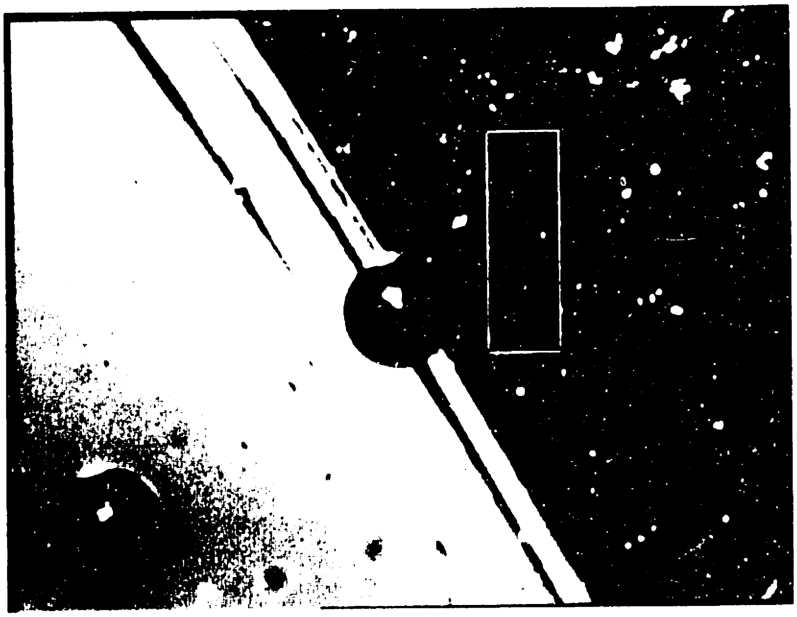

Figure 5.20. Shapes formed by depositing 10 microdrops on the target shown in Figure 5.17. Candelilla wax, T_0 = 90°C, T_t = 36°C, f = 10 kHz. Rectangle: 100 μm x 300 μm.

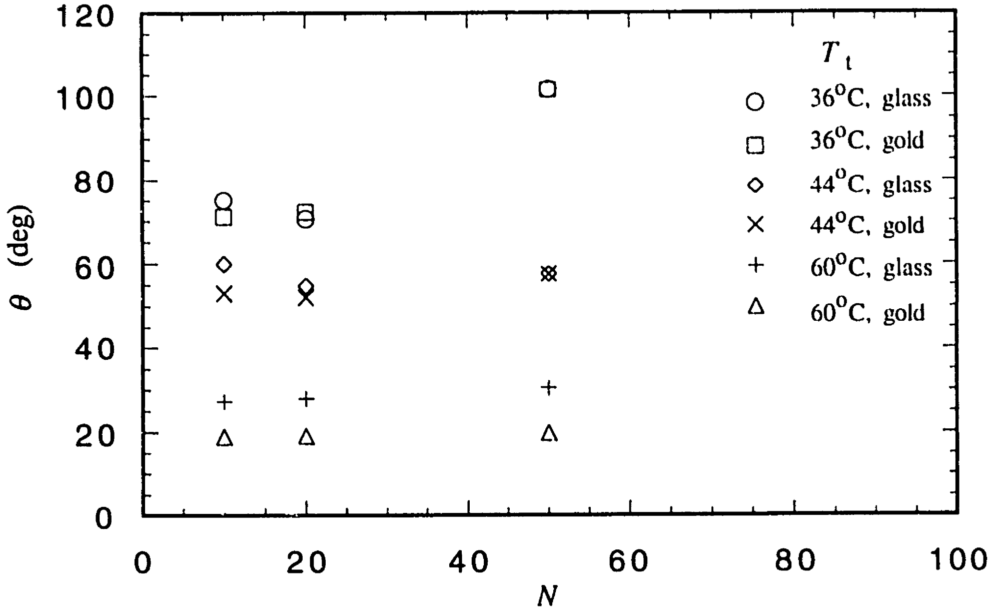

Figure 5.21. Solidification angle θ against droplet number N at different target temperatures. The same target as that shown in Figure 5.17. Candelilla wax, $T_0 = 90^oC$, $f = 10$ kHz.

Figure 5.21 compares the solidification angle obtained on the thin gold coating with that obtained on the uncoated glass surface at different target temperatures. The temperature of the melt (candelilla wax) is 90°C and the deposition frequency is 10 kHz. In the figures, the x coordinate is droplet number which means the deposition time, that is, the larger the droplet number, the longer the deposition time.

At higher target temperatures, there are significant differences in solidification angles between glass and gold surfaces; however, at lower target temperatures (say, $T_t = 36^oC$, Figure 5.20), there are only slight differences between these two cases. The properties of the surface film appear to play a more important role at higher target temperatures, while at lower target temperatures the solidification process appears to dominate.

Chapter 6

SOME PHENOMENA OBSERVED IN THE DEPOSITION OF MOLTEN MICRODROPS

In this chapter we will briefly describe some interesting phenomena associated with the molten droplet deposition processes. These phenomena were observed but not fully investigated and further study is needed to understand them in quantitative terms.

6.1 Continuous High-frequency Deposition of Droplets on a Cold Target with High Thermal Conductivity

As mentioned in Section 5.3.3, the shapes formed by dropwise deposition are significantly different for targets with different thermal conductivities (Figures 5.16). In this section we will illustrate phenomena that occur when a large volume of melt is deposited by high-frequency droplet deposition on a cold target whose thermal conductivity is much higher than that of the melt.

The pictures in Figure 6.1 show two imperfect spheres formed by depositing 8,000 50 μm diameter droplets at 10 kHz on an aluminum target. One is composed of candelilla

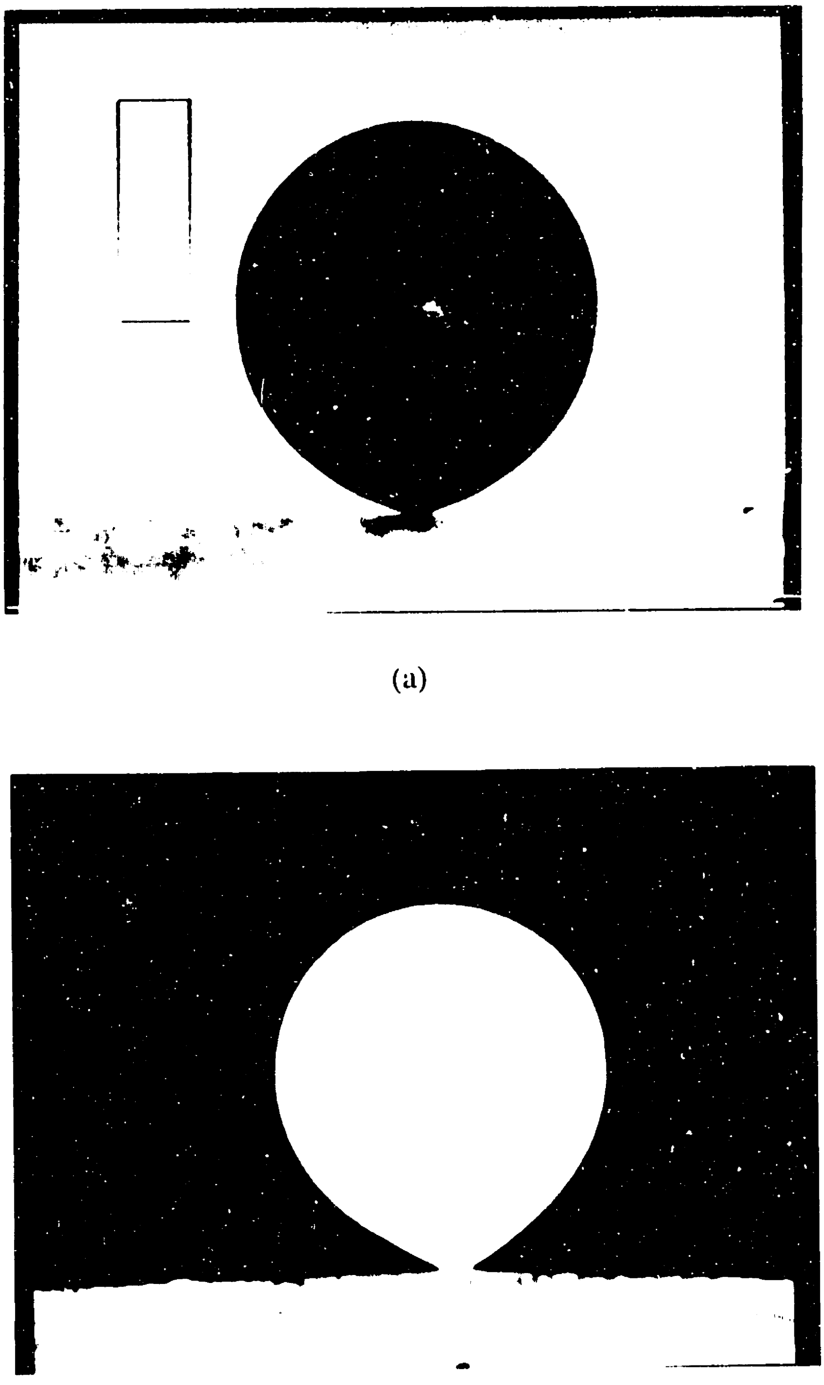

(a)

(b)

Figure 6.1. Imperfect spheres formed by depositing 8,000 50 μm diameter droplets on an aluminum target, f = 10 kHz. Rectangle: 200 μm x 600 μm. (a) Candelilla wax, T_0 = 90°C, T_t = 35°C; (b) microcrystalline wax, T_0 = 115°C, T_t = 48°C.

wax (Figure 6.1a) and the other of microcrystalline wax (Figure 6.1b). The rectangle measures 200 μm x 600 μm and the diameter of the spheres about 1 mm. The distance between the droplet generator and the aluminum target is 4.5 mm for the case of candelilla wax, and 3 mm for the case of microcrystalline wax.

The interesting thing is that the diameter of the contact area between the sphere and the target is only about 65 μm, which is very small compared with that of the sphere. Because of the high thermal conductivity of aluminum (204 W m^{-1} K^{-1}) and the low target temperature, the moving contact line froze and became immobilized very quickly, so quickly in fact that the first couple of droplets solidified before the next ones arrived, and thus formed a "thermal bottleneck" of very small diameter between the aluminum target and the rest of the incoming droplets. This thermal bottleneck reduced the heat transfer from the incoming droplets to the aluminum target and there was not enough time for the rest of the incoming droplet to solidify due to the high deposition frequency and low thermal conductivity of the ambient air (0.0261 W m^{-1} K^{-1}). The incoming droplets formed a big, liquid melt drop sustained by surface tension, which eventually (after the deposition stopped, except very near the "thermal bottleneck", see below) solidified due to heat transfer from the liquid drop to the ambient air as well as to the target.

The exact shape of the sphere is also affected by the deposition frequencies in this case. Figure 6.2 was obtained under the same conditions as those for Figure 6.1 except for the deposition frequency which was 10 kHz for Figure 6.1 and 15 kHz for Figure 6.2. Comparing Figure 6.2 with Figure 6.1, we see that the shape in Figure 6.2 is closer to a sphere than that in Figure 6.1. During the deposition processes, the temperature inside the growing drop was not uniform and was lower at the lower part of the drop, which was exposed to the ambient air longer and was also closer to the cold target, than the upper part of the drop. The resulting shape of the drop was somewhat like an inverted pear. If the deposition frequency is increased (shorter forming time), the temperature in the drop will

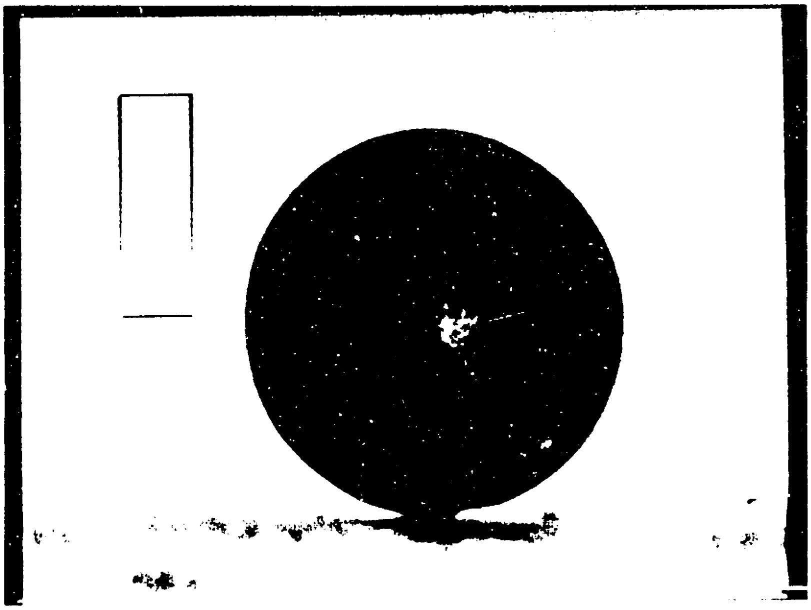

Figure 6.2. Sphere formed under the same conditions as those in Figure 6.1a except for the deposition frequency, f = 15 kHz. Rectangle: 200 μm x 600 μm.

be more uniform and thus the shape will be closer to a sphere. The forming time (droplet delivery time) for Figure 6.2 was 0.53 seconds which was 0.27 seconds shorter than that for Figure 6.1. The diameter of the "thermal bottleneck" which connects the sphere to the target is also larger for the case of higher deposition frequencies.

6.2 Vibration of a Growing Drop Deposited on a Cold Target with High Thermal Conductivity at High Frequencies

We observed that when a growing drop was formed by continuous high-frequency deposition of a large number of molten droplets on a cold target with high thermal

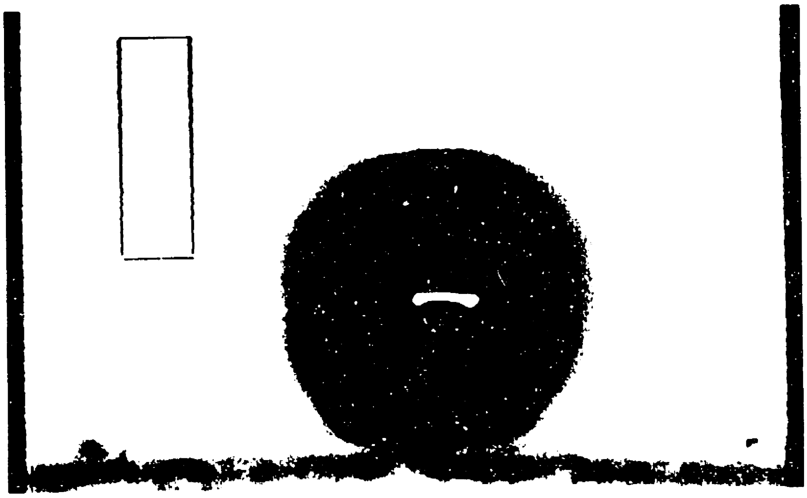

Field 17

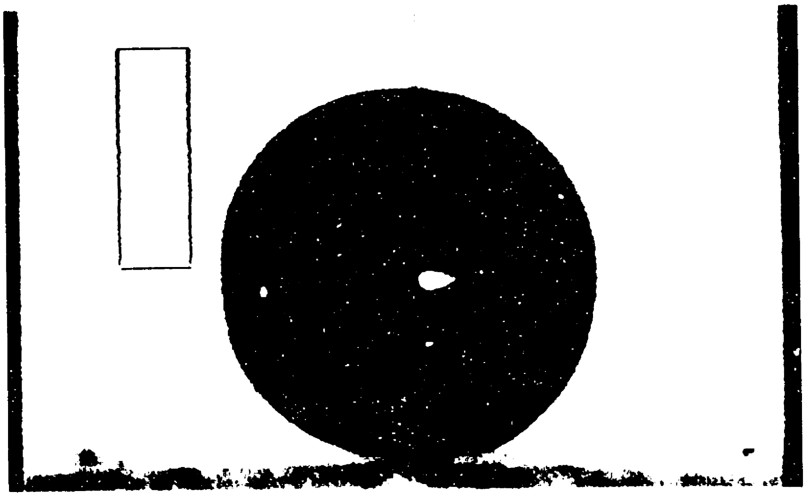

Field 29

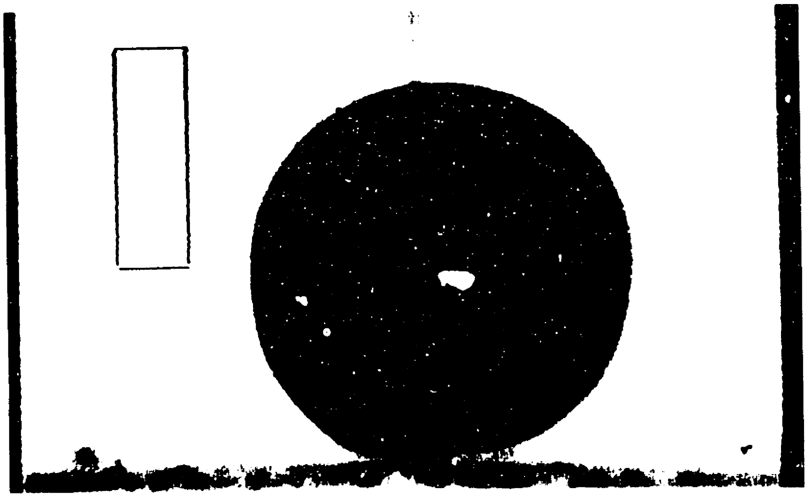

Field 30

Figure 6.3. Vibration of a growing drop deposited on an aluminum target. Candelilla wax, $T_0 = 90^{\circ}C$, $T_t = 35^{\circ}C$, $f = 15$ kHz. Rectangle: 200 μm x 600 μm.

conductivity, it would sometimes vibrate. The pictures in Figure 6.3 show a growing drop at different times (fields). The temperatures of the melt (candelilla wax) and the target (aluminum) are 90°C and 35°C, respectively. The deposition frequency is 15 kHz.

As mentioned in the previous section, the fist couple of droplets solidified very fast after being deposited on the cold aluminum target, and formed a "thermal bottleneck" of small diameter which was the sole support for the large growing melt drop, which was very large compared with the "thermal bottleneck" diameter. The system was like a liquid sphere sitting on a very small solid disc (the contact area was very small) and not very stable dynamically, particularly to lateral perturbations. Small perturbations (say, in the incoming droplet jet), could set the liquid sphere into lateral vibration.

6.3 Dynamic Collapse of a Growing, Arrested Drop

As shown in Section 6.1, by depositing 8,000 droplets on an aluminum target at high frequency (10 kHz or 15 kHz), a big liquid sphere will form and then solidify. If the same number of droplets is deposited on a plexiglas surface at the same frequency, the drop shape will be different. Figure 6.4 was taken at the same conditions as that for Figure 6.1 except for the target, which in this case is plexiglas. The contact line freezes (is arrested), at a much larger diameter, and thereafter the liquid drop grows by bulging out. At the beginning, the shape of the growing drop is similar to that on an aluminum target except with a larger base, but at frame 32 the growing drop suddenly collapses (i.e. suddenly spreads over the target, reaching a new frozen contact line position) and becomes a hemisphere.

The thermal conductivity of plexiglas is 0.1527 W m^{-1} K^{-1} which is much smaller than that of aluminum (204 W m^{-1} K^{-1}), so the base diameter of the growing drop for plexiglas is larger than that for aluminum. The local temperature around the contact line is

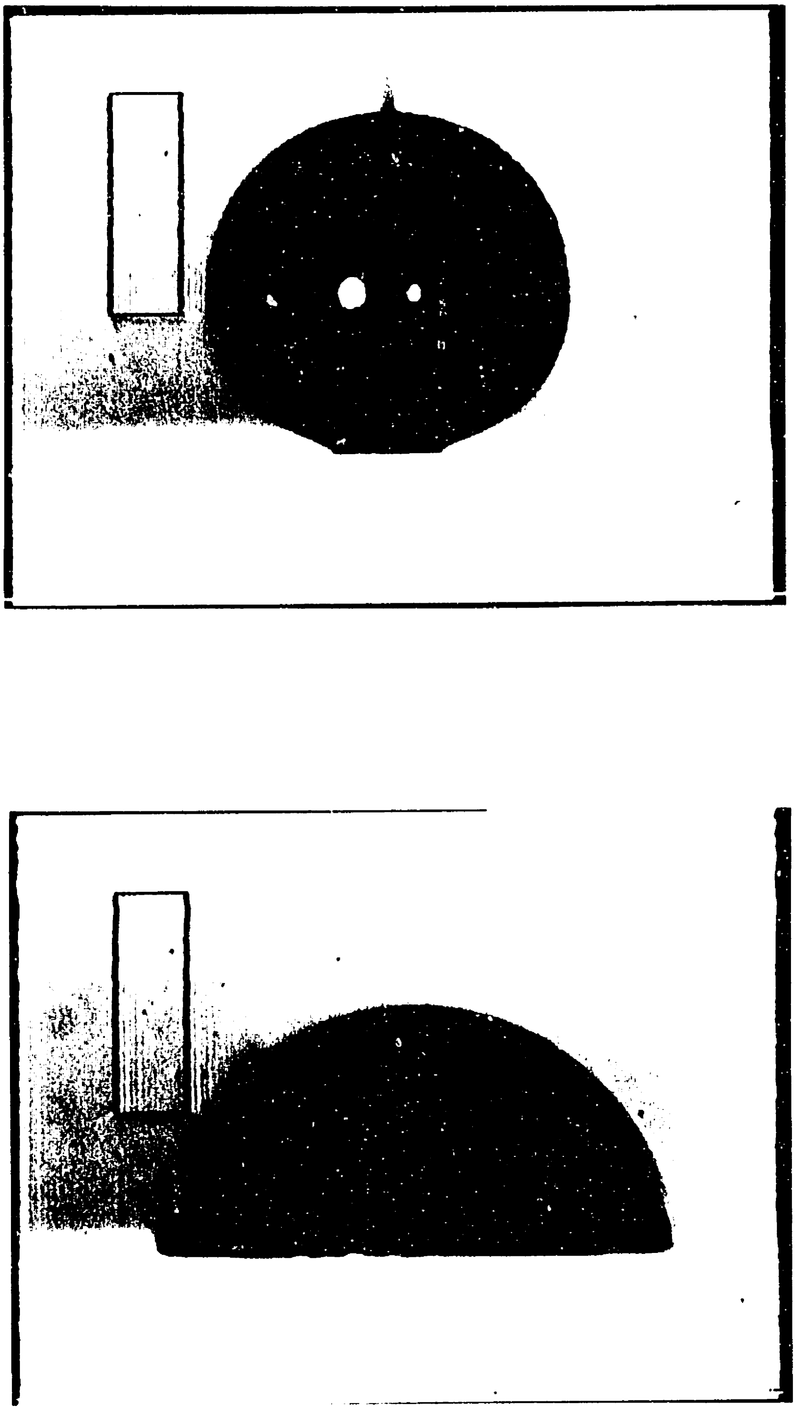

Figure 6.4. Collapse of a growing drop on a plexiglas surface. Candelilla wax, $T_0 = 90^{\circ}C$, $T_t = 35^{\circ}C$, f = 15 kHz. Rectangle: 200 μm x 600 μm.

higher in the case of the plexiglas target. One of the possibilities which could cause the collapse of a growing drop is remelting of the frozen contact line. After the contact line freezes the first time, hot melt is added to the drop, but the heat is retained there because of the "thermal bottleneck". Eventually, as the superheated melt bulges out over the frozen contact line, and the local temperature of the "thermal bottleneck" region increases, the contact line remelts and then skips to a new radial position and refreezes there.

6.4 Some Electrostatic Effects

The deformation and stability of a free uncharged dielectric drop in an electric field has been studied by a number of authors (e.g. Cheng 1989). The processes of charging ink droplets have also been studied in the context of ink jet printing (Heinzl and Hertz, 1985). In this section, we will discuss some electrostatic effects on a drop of water or glycerin on a plexiglas surface as well as on a flying molten wax droplet observed in our experiments.

6.4.1 Effects of an External Electric Field on Simple Liquid Drops on a Plexiglas Surface

When a drop of water or glycerin is placed on a plexiglas surface, it will spread on that surface until it reaches the equilibrium state and the contact line is a circle. If an electric field is applied parallel to the surface, the shape of the drop will change and the contact line will move towards both electrodes (metal plates) and the drop shape will become oval (Figure 6.5). In these experiments, the distance between the two metal plates which formed the electrodes was about 8 mm and the voltage applied to them was 10,000 V. Thus the electric field strength E was $1.25\text{x}10^6$ V m^{-1}. The base diameter of the liquid drop was about 3 mm.

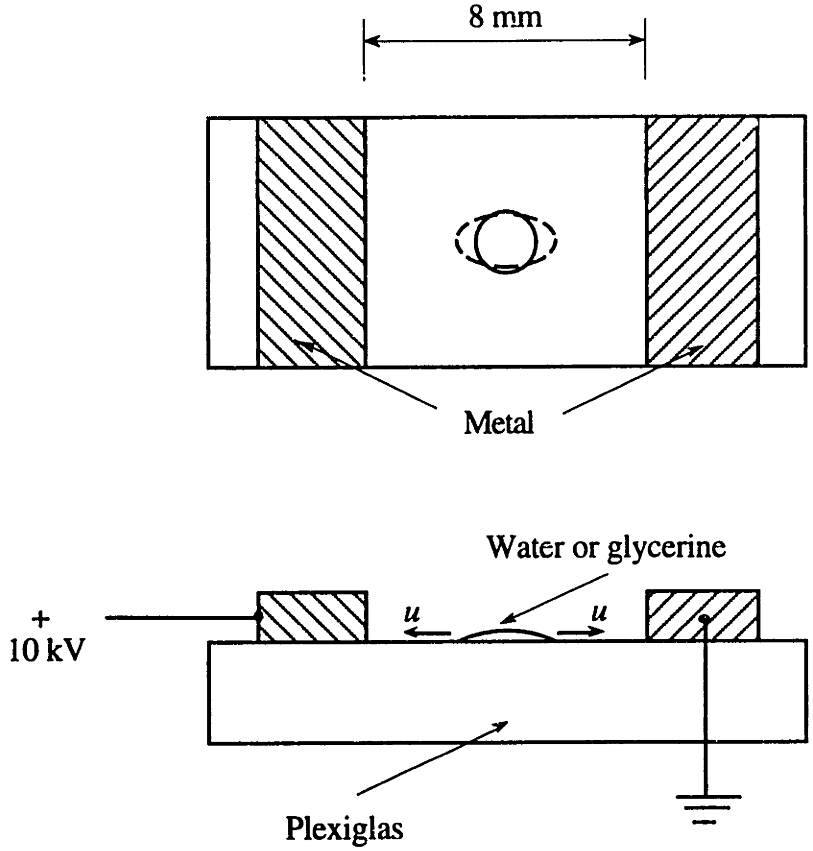

Figure 6.5. A drop of water on a plexiglas surface in an electric field.

After the electric field is applied, the drop is charged by polarization. The negatively charged side tends to move toward the positive plate and the positive charged side toward the negative plate. Thus the drop is distorted by the electric field until it finally reaches a new equilibrium state. From this observation, one may imagine that when molten wax droplets fly through an electric field, they will also be polarized and deformed by the electric field. Thus the solid structure formed on the target will be different from that formed without the electric field (see the next section).

6.4.2 Effects of an External Electric Field on Molten Wax Microdrops in Flight

In our experiments, an electric field was established in the space between two parallel metal plates and the voltages applied to these two plates were varied from 0 to 3,500 V. The distance between the two metal plates was 3 mm and the distance from the droplet generator to the target was 4 mm. The experimental set-up is schematically shown in the Figure 6.6. When a droplet of molten wax travels through the electrical field, its shape will change and the shape of the structure formed on the target will also change significantly.

Figure 6.7 shows the shapes of the formed structures under different voltages. If no voltage was applied to the metal plates , the 15 droplets which were deposited in succession

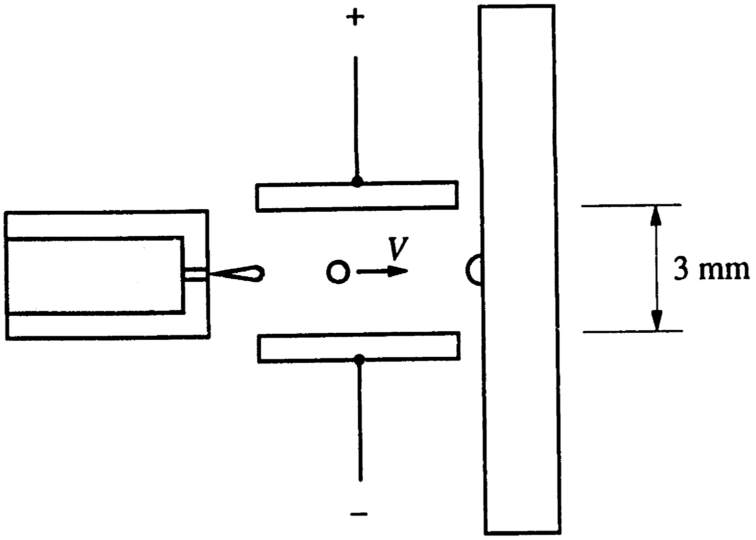

Figure 6.6. Schematic of the experimental set-up for examining the effects of electrical fields on flying droplets.

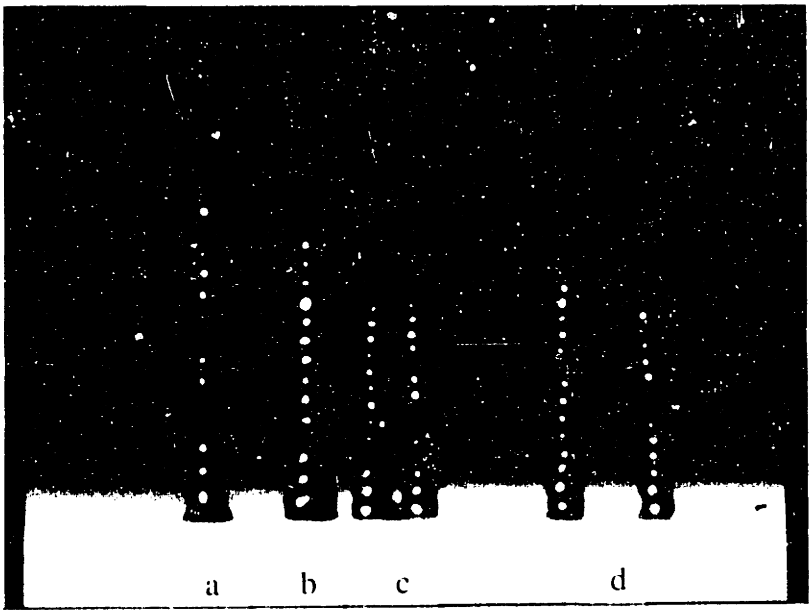

Figure 6.7. Pillars formed by depositing 15 droplets under different electrical fields. Candelilla wax, $T_0 = 95^{o}C$, $T_t = 38^{o}C$, $f = 10$ Hz. Rectangle: 100 μm x 300 μm. (a) $V = 0$ V; (b) $V = 1{,}500$ V; (c) $V = 2{,}500$ V; (d) $V = 3{,}500$ V.

formed a straight pillar of height 0.48 mm on the target, but when a voltage of 1,500 V ($E = 5\text{x}10^5$ V m^{-1}) was applied to the metal plates the pillar was shorter (0.41 mm). If the applied voltage increased to 2,500 V ($E = 8.3\text{x}10^5$ V m^{-1}), the 15 droplets formed *two* shorter pillars instead of one, with a separation of about 70 μm. Increasing voltage increased the separation; the separation was, for example, 130 μm when the voltage was 3,500 V ($E = 1.17\text{x}10^6$ V m^{-1}).

The explanation for these phenomena is as follows. As mentioned in Section 4.1, on its way to the target the droplet typically cools down by only few ^{o}C and is thus still in liquid state during flight. Figure 6.8 shows a sketch of the process of a droplet traveling

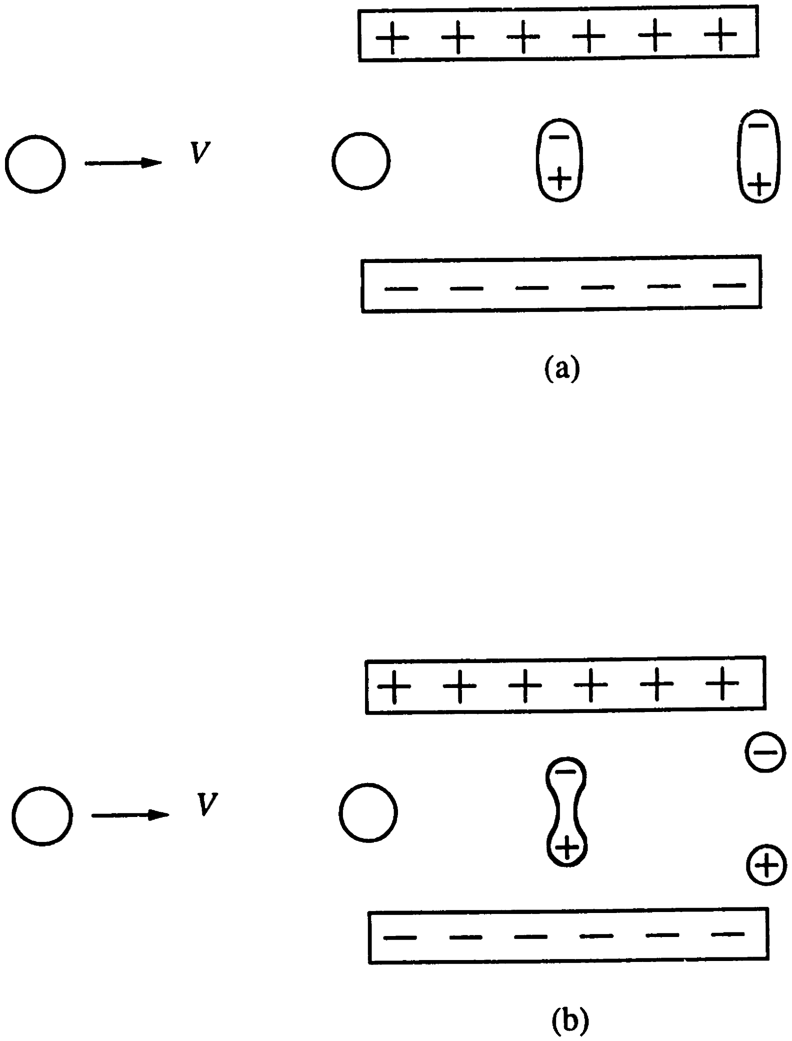

Figure 6.8. Droplets traveling through an electrical field.

through an electrical field. As it flies through the applied electric field, the droplet becomes polarized and is pulled by the electric field into an oval shape (Figure 6.8a). When these deformed droplets land, they produce a pillar which is shorter and stouter. If the force due to the electric field is strong enough to overcome the surface tension, the droplet will be broken into two small droplets in flight (Figure 6.8b). The two smaller droplets (because of the droplet's polarization in the electric field, one is positively charged and the other is negatively charged) will be deflected in opposite directions as they travel through the rest of the electric field. The positively charged one will be attracted by the negative plate and the negatively charged one by the positive plate. This produces the twin pillars seen in Figure 6.7.

6.5 Irregular Shapes of Spreading Molten Drops

In Section 5.3.2 we described the spreading and solidification of a growing drop. It was, occasionally, found that the shape of the solidified drop was irregular, especially, at the low target temperature T_t and large droplet number N.

Figures 6.9 and 6.10 give two examples. In Figure 6.9 both the melt and the target were candelilla wax. The melt temperature was 90°C, the deposition frequency 15 kHz, and the droplet number 100. The target temperatures in Figures 6.9a and 6.9b were 60°C and 35°C respectively. The shape of the solidified drop was a spherical cap in the case of higher target temperature (60°C, Figure 6.9a); however, it was irregular when the target temperature was lower (35°C, Figure 6.9b).

In Figure 6.10 both the melt and the target were microcrystalline wax. The melt temperature was 115°C, the target temperature 60°C, and the deposition frequency 10 kHz. The droplet numbers in Figures 6.10a and 6.10b were 100 and 250 respectively. The shape of the solidified drop was a spherical cap for the droplet number $N = 100$ (Figure 6.10a), but for $N = 250$ the solidified drop had an irregular shape. Note that Figures 6.9 and 6.10 only give two examples and it is not always the case to have the irregular shapes at the low target temperature or the large droplet number.

Normally the contact line of a molten drop is a circle as it is moving on a solid surface; however, it will become irregular (thus the shape of the solidified drop) if its

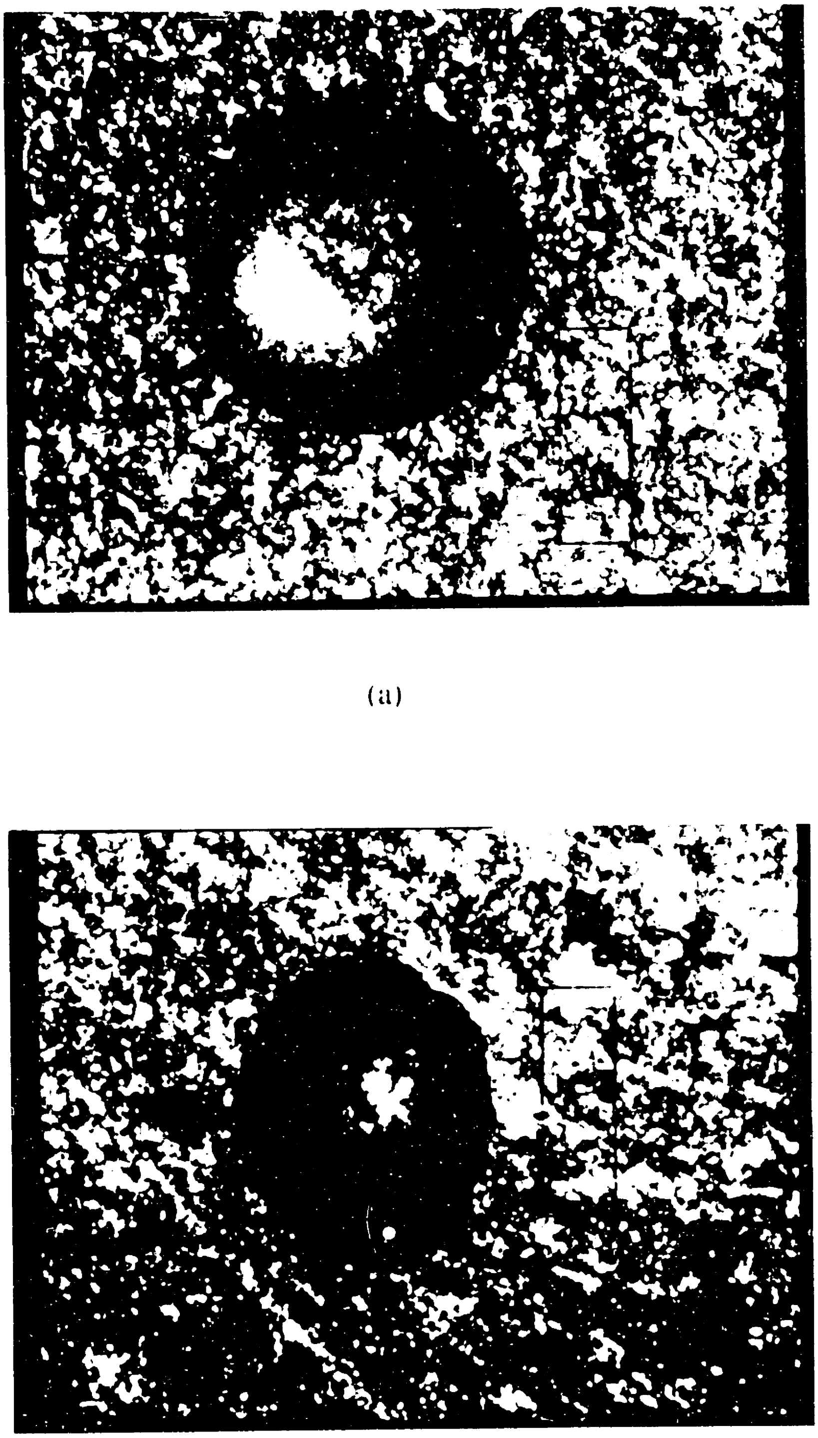

(a)

(b)

Figure 6.9. Shapes of the solidified drops. Candelilla wax, $T_0 = 90^\circ C$, f = 15 kHz, N = 100. Rectangle: 100 µm x 300 µm. (a) $T_t = 60^\circ C$; (b) $T_t = 35^\circ C$.

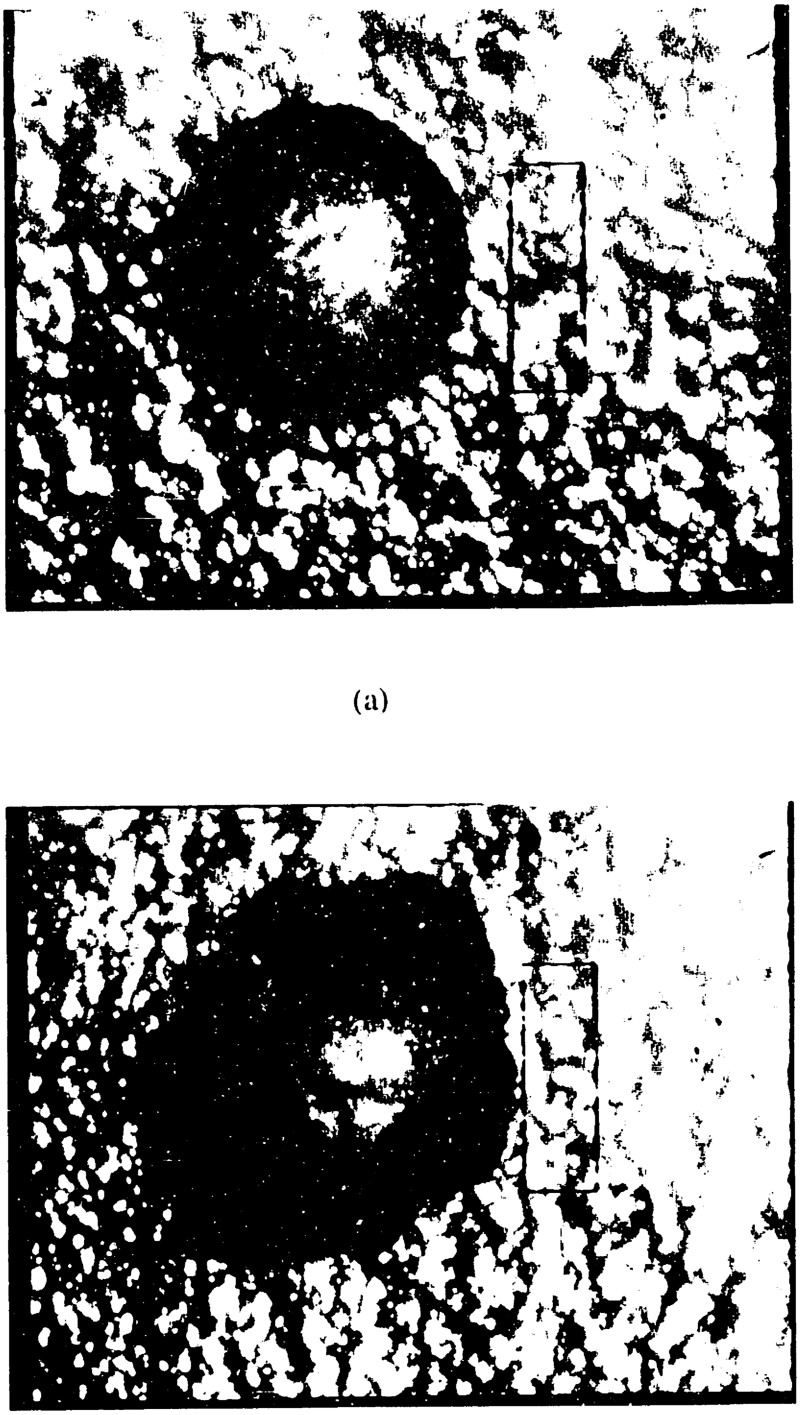

(a)

(b)

Figure 6.10. Shapes of the solidified drops. Microcrystalline wax, $T_0 = 115^\circ C$, $T_t = 70^\circ C$, $f = 10$ kHz. Rectangle: 100 μm x 300 μm. (a) $N = 100$; (b) $N = 250$.

advance velocity around the circle is not uniform. The reason why the velocity is not uniform is not clear. One likely reason might be the high sensitivity of contact line freezing to the local values of the irregularities of the solid surface, the chemical contaminations of the solid surface, and the inhomogeneity of the solid surface or the melt. If the spreading is virtually complete before the contact line freezes, these effects have little impact. If, on the other hand, contact line freezing dominates the final drop shape, the effects will be very apparent.

Several targets, which were made of different materials such as glass, plexiglas, aluminum, and the same materials as the melts (candelilla wax and microcrystalline wax in this case), were used and the irregular shapes occurred occasionally for each target.

Chapter 7

CONCLUSIONS

Arbitrary 3D objects may be fabricated by precisely controlled deposition and solidification of melt microdrops. To gain an understanding of the physical phenomena associated with the basic deposition modes, extensive experiments have been carried out with a piezo-driven, drop-on-demand droplet generator. Individual molten droplets (about 50 μm in diameter) are ejected at controlled frequencies in the range 0 to 15 kHz from the generator and directed to a target, where they impact and solidify. The conditions required for controlled deposition and solidification are discussed, and experimental results and theoretical analyses are given for each basic deposition mode. Two types of waxes, candelilla and microcrystalline, were used. Our experiments were done with waxes, but the analysis provides a means of generalizing the results to other materials.

To maintain ballistic accuracy, the distance between the droplet generator and the target must be smaller than the droplet's stopping distance l_s, which is the distance the droplet travels before it is brought to a halt by viscous drag. A simple model for estimating the stopping distance is given in Section 3.2 (Equation (3.3)). The estimate of the stopping distance agrees well with our observations.

An understanding of the cooling and solidification of molten droplets is essential for controlling the deposit shape. There are three thermal times: (i) the time τ_1 for removing the droplet's superheat and bringing the liquid down from T_0 to T_f; (ii) the additional time τ_2 for the droplet to lose all its latent heat of fusion and completely solidify; and (iii) the further time τ_3 for it to complete its cooldown to the ambient temperature T_a. The total time $\tau_1 + \tau_2 + \tau_3$ is dominated by τ_2. The analysis given in Sections 3.3 and 4.1 (Equations (3.5), (3.6), (3.7), and (4.1)) provides simple approximate estimates of thermal and solidification timescales for molten droplets.

In this study, the distance between the droplet generator and the target was about 3 mm and the Weber number at impact was typically about 6. On its way to the target the droplet typically cooled down by only a few ^{o}C and thus impacted with essentially its original temperature T_0. The entire spreading process of a single droplet took only about 40 μs, while the solidification timescale was typically of the order of 10 ms, three orders of magnitude longer than the spreading time (Section 4.1). The spreading time of 40 μs was roughly consistent with both the kinematic collision timescale $2a/V$ and the capillarity-driven, inertially-resisted spreading timescale $(\rho a^3/\sigma)^{1/2}$; these were of the same order because $We \sim O(1\text{-}10)$. Gravitational effects were completely insignificant, the Bond number $\rho g a^2/\sigma$ being very small in this case. The droplet touched the surface, wetted it, showing some inertial distortion about 20 μs after impact, but quickly assumed a spherical-cap shape under the action of capillarity forces, reaching what appeared to be a state of mechanical equilibrium with finite contact angle long before it solidified (Figure 3.2).

The basic deposition modes are— dropwise (low frequency) columnar deposition, continuous (high frequency) columnar deposition, sweep deposition of continuous beads on surfaces, and repeated sweep deposition. Each of these basic deposition modes offers a particular way of producing a solid structure and suggests some potential applications of this technology.

For the low frequency columnar deposition, there are two design parameters: (i) the solidification angle θ, which determines the shape of the column (Equations (4.4) and (4.5)), and (ii) the maximum frequency f_{max} at which the shape formed by dropwise deposition is independent of frequency. A model for estimating this maximum frequency f_{max} was described in Section 4.3. The column was modeled as a semi-infinite cylinder which acted as a fin (Figure 4.6). The entire pillar was at the ambient air temperature T_{a} before a molten droplet with temperature T_{o} arrived at its tip at $t = 0$. The resulting temperature transient in the solid part of the cylinder was controlled by the fin heat transfer equation (Equations (4.7)) and the droplet solidification time τ_{s} was assumed to be dominated by the time for the droplet to lose its latent heat. A solution for the solidification time τ_{s} was pieced together from the small-time and large-time limiting cases of the heat flux $q_{\mathrm{o}}(t)$ at $x = 0$ by assuming that the transition from one to the other occurs at a time when the two give the same result. The characteristic post-solidification cooldown time τ_{c} was given by Equation (4.15). The maximum frequency f_{max} obtained from Equations (4.6), (4.12), and (4.15) was in good agreement with our observations.

By adjusting the ratio of the horizontal center-to-center droplet spacing w to the incoming droplet radius a, one can give a pillar of droplets any angle ϕ between 0^{o} and 90^{o} (Figure 4.5). The precise relationship between w/a and ϕ depends on the apparent contact angle and the Weber number at impact, if that number is not sufficiently small. For small Weber number (inertial effects are insignificant compared with capillary forces), Equation (4.17) is in good accord with our observations (Figure 4.7). Even a "horizontal" element can be made by deposition of molten droplets from "above", since capillary forces dominate over inertial forces at impact.

For the continuous high-frequency deposition, the design parameter is the radius R of the formed column. A simple theory for continuous deposition was derived by referring to Figure 4.8 and an expression (Equation (4.19)) for the radius R was obtained by writing down the first law of thermodynamics for a control volume comprised of the hemispherical liquid cap, setting the temperature equal to T_f in the outflow at the base. The experimental data for R obtained with two different waxes over a range of deposition frequencies were compared with the model and the agreement was quite good (Figure 4.9).

The model for predicting the solidification front inside the column was also described in Section 4.4. The local radius of the solidification zone r_s and the axial length of the solidification zone λ were given by Equations (4.21) and (4.22). For a typical case with wax, λ/R was about 2-3.

For the sweep deposition of beads on flat surfaces, the important parameter is the ratio of $f(2a)$ to U. If the ratio $f(2a)/U$ is too small, a line of separate sessile droplets will form. If the ratio $f(2a)/U$ is too large, on the other hand, the instability may cause the bead to have large bulges (Figures 4.12 and 4.13). The required operating conditions for droplet overlap are given by Equation (4.24). The range of the ratio $f(2a)/U$ within which a smooth bead will form depends on the deposition frequency, the temperatures and the properties of the substrate as well as the melts. This range is wider for high deposition frequencies, high temperatures, and the targets with low thermal conductivities.

For the smooth bead, the design parameters are its maximum width W (or its base width b) and the solidification angle θ. A model written in terms of the solidification angle was given to predict the bead width versus the operating parameter $f(2a)/U$ (Equations (4.29) and (4.30)). The prediction was in good agreement with the experimental data obtained from the high target temperature and high deposition frequency.

The required operating conditions for repeated sweep deposition were also discussed. Like the sweep deposition of beads on flat surfaces, the ratio of $f(2a)/U$ is very important and should be kept somewhat above the critical value $F(\theta)$ of Equation (4.25). The exact value of $f(2a)/U$ for forming a smooth wall depends on the deposition frequency, the melt and ambient temperatures, and the melt properties. At too low values, the microdrops will not form a continuous bead, and structural irregularities will soon arise and amplify as the next layers are laid down, while at too high values, instabilities tend to occur.

The solidification angle is an important parameter since it determines the shapes formed by droplet deposition. This angle was studied for both single molten microdrops and growing molten drops spreading and solidifying on the targets of different materials. The solidification angle is not an equilibrium property since the molten drop spreading occurs under thermal nonequilibrium conditions. Under certain conditions the melt behaves as if it possesses an apparent static contact angle which is, at least approximately, a property of the melt material, the target material, and the characteristic temperatures involved, but independent of the spreading process. If the impact and spreading occur in a time short compared with the solidification time, the droplet will end up with a quasi-equilibrium shape with this apparent static contact angle, having apparently attained a mechanical but not thermal equilibrium, and will then freeze on a much longer timescale. The solidification angle is in such cases essentially equal to the apparent static contact angle of the melt before solidification.

A novel method is devised to study the solidification angle and the freezing of an advancing melt contact line: the continuously fed drop method, in which a certain number of superheated droplets are deposited on a subcooled target at a frequency which is so high (typically of the order of 10 kHz) that the droplets coalesce into a growing liquid drop. The shape of a growing drop varies with the droplet number (Figure 5.5), and there are two stages (except for the very beginning). In the first stage, the growing drop spreads on the solid surface with a constant apparent contact angle θ_0, and in the second stage, the apparent contact angle increases significantly with increasing the droplet number due to the frozen or near-frozen contact line. The higher the target temperature, the longer the first stage lasts.

For given target and melt materials, if the contact line advance speed is not too small (high deposition frequencies) and the target temperature is high, the solidification angle is mainly controlled by the target temperature (Figures 5.10, 5.11, and 5.13).

The thermal properties of the target have strong influence on the shape of the structures formed by molten droplet deposition (Figure 5.16).

Finally, some interesting phenomena associated with the molten droplet deposition and solidification processes were briefly described in Chapter 6. These phenomena were observed but not fully investigated and further study is needed to understand them.

NOMENCLATURE

a	droplet radius
A	cross-sectional area of a bead
b	base width of a bead
c	specific heat
C_D	drag coefficient
D_meas	diameter of a deposited drop which consists of N individual microdrops, Figure 5.2
D_sphere	calculated diameter of a sphere which has the same volume as that of a deposited drop, $2aN^{1/3}$, Figure 5.2
E	electric field
f	deposition frequency
f_max	maximum frequency at which dropwise deposition is independent of frequency
$F(\theta)$	droplet coalescence threshold, Equation (4.25)
g	acceleration due to gravity
h	length added to a pillar by each deposited droplet, Figure 4.5
k	thermal conductivity
k_a	thermal conductivity of ambient material
k_g	thermal conductivity of gas
k_t	thermal conductivity of target material
l_s	droplet's stopping distance, Equation (3.3)
L	latent heat
L'	latent heat, $L + c(T_\mathrm{o} - T_\mathrm{f})$, Equation (4.14)
N	droplet number
N^*	droplet number at which contact line freezes, Section 5.3.2
Nu	Nusselt number
q	heat flux
q_o	heat flux at $x = 0$, Equation (4.9) and Figure 4.6
r	pillar radius measured at the maximum point, Figure 4.5
r_b	drop base radius, Figure 4.1

r_b^*	drop base radius when contact line freezes, Section 5.3.2
r_s	radius of the solidification front in a growing column, Figure 4.8
R	column radius in the continuous solidification mode, Figure 4.8
R_c	cap radius of curvature of a deposited droplet, Figure 4.1
Re	Reynolds number, $\rho_g V(2a)/\mu_g$
Re_o	Reynolds number, $\rho_g V_o(2a)/\mu_g$
R_p	radius of a semi-infinite cylinder, Figure 4.6
t	time
T	temperature
T_a	ambient temperature
T_f	fusion temperature
T_t	target temperature
T_o	source temperature
u	contact line speed, Equation (5.2)
U	material's downward flow speed in the reference frame of Figure 4.8, $4\pi a^3 f/(3\pi R^2)$; target speed
V	droplet velocity; droplet impact speed
V_o	droplet velocity at the droplet generator
w	horizontal center-to-center separation between two consecutive droplets
W	maximum width of a bead
We	Weber number, $\rho V^2 a/\sigma$
x	coordinate axis
x_e	coordinate of the point at which $T - T_a$ equals $(T_f - T_a)/2.71$ at time τ_s

Greek symbols

α	thermal diffusivity
α_a	thermal diffusivity of ambient material
β	$2k_g Nu/k$, Equation (4.8)
δ	thermal penetration depth
δ_g	thickness of thin gold film
θ	solidification angle

θ_0	constant apparent contact angle, Section 5.3.2
λ	axial length of the solidification zone of a growing column, Figure 4.8
Λ	fastest-growing wavelength of a melt bead, Equation (4.31)
μ	viscosity
μ_g	gas viscosity
ξ	defined by Equation (4.13)
ρ	density
ρ_g	gas density
σ	surface tension
τ	characteristic time
τ_c	time for a droplet to cool down from T_f to a temperature close enough to T_a, Equation (4.6)
τ_s	solidification time
τ_1	time for a droplet to cool down from T_0 to T_f, Equation (3.5)
τ_2	time for a droplet to lose all its latent heat of fusion, Equation (3.6)
τ_3	time for a droplet to cool down to from T_f to T_a, Equation (3.7)
ϕ	angle of an inclined pillar, Figure 4.5
ω	dimensionless temperature ratio, $(T - T_a)/(T_f - T_a)$

REFERENCES

Adamson, A. W. 1990 *Physical Chemistry of Surfaces*, 5th ed. New York: Wiley.

Aronson, R. B. 1993 So Rapid Prototyping Works. Now What? *Manufacturing Engineering* **111** No. 5, 37-42.

Ashley, S. 1991 Rapid prototyping systems. *Mechanical Engineering* **113**, No. 4, 34-43.

Bird, R. B., Stewart, W. E. and Lightfoot, E. N. 1960 *Transport Phenomena.* New York: Wiley.

Chandrasekhar, S. 1981 *Hydrodynamic and Hydromagnetic Stability*, ch. 12. New York: Dover.

Crank, J. 1984 *Free and Moving Boundary Problems.* Oxford: Clarendon.

de Gennes, P. G. 1985 Wetting: statics and dynamics. *Rev. Mod. Phys.*, **57**, No. 3, 827-863.

de Gennes, P. G., Hua, X and Levinson, P. 1990 Dynamics of wetting: local contact angles. *J. Fluid Mech.* **212**, 53-63.

de Gennes, P. G. 1990 Dynamics of Wetting. In *Liquids at Interfaces,* Ed. J. Charvolin, et al. 273-291. Amsterdam: North-Holland.

Dussan, E. B. 1979 On the spreading of liquids on solid surface: static and dynamic contact lines. *Ann. Rev. Fluid Mechanics* **11**, 371-400.

Gao, F. and Sonin, A. A. 1994 Precise Deposition of Molten Microdrops: the Physics of Digital Microfabrication. *Pro. R. Soc. Lond.* A **444**, 533-554.

Heinzl, J. and Hertz, C. H. 1985 Ink-Jet Printing. *Advances in Electronics and Electron Physics* **65**, 91-171.

Hill, J. M. and Kucera, A. 1983 Freezing a Saturated Liquid Inside a Sphere. *Int. J. Heat Mass Transfer* **26**, 1631-1637.

Hocking, L. M. 1991 Rival Contact-angle Models and the Spreading of Drops. *J. Fluid Mech.* **239**, 671-681.

Hoffman, R. L. 1975 A Study of the Advancing Interface. I. Interface Shape in Liquid-Gas Systems. *Journal of Colloid and Interface Science* **50**, No. 2, 228-241.

Lin, A. R. Solid Ink in the Ink Jet Printing Technology. Dataproducts Corporation, Brookfield, CT.

Lowan, A. N. 1945 On the Problem of Heat Conduction in a Semi-Infinite Radiating Wire. *Quarterly of Appl. Math.* **3**, 84-87.

Marcus, H. L. et al. 1993 *Proceedings of the Fourth Solid Freeform Fabrication Symposium.* Austin: The University of Texas at Austin.

Powers, J. M., Craig, R. G. and Peyton, F. A. 1969 Calorimetric Analysis of Commercial Dental Waxes. *J. Dent. Res.* **48**, 1165-1170.

Probstein, R. F. and Fassio, F. 1970 Dusty Hypersonic Flows. *AIAA J.* **8**, 772-779.

Prud'homme, M., Nguyen, T. H. and Nguyen, D. L. 1989 A Heat Transfer Analysis for Solidification of Slabs, Cylinders, and Spheres. *Journal of Heat Transfer* **111**, 699-705.

Reed Wax, Reading, MA. *Specifications.*

Riley, D. S., Smith, F. T. and Poots, G. 1974 The Inward Solidification of Spheres and Circular Cylinders. *Int. J. Heat Mass Transfer* **17**, 1507-1516.

Sonin, A. A. 1991 Controlled Microdrop Melt Deposition Processes: Prospects and Scaling Laws. Research Proposal submitted to (and funded by) NSF.

Tanner, L. H. 1979 The Spreading of Silicone Oil Drop on Horizontal Surfaces. *J. Phys. D: Appl. Phys.* **12**, 1473-1484.

Warth, A. H. 1956 *The Chemistry and Technology of Waxes* 2nd ed. New York: Reinhold.

Whitaker, S. 1972 Forced Convection Heat Transfer Correlations for Flow in Pipes, Past Flat Plates, Single Cylinders, Single Spheres, and Flow in Packed Beds and Tube Bundles. *AIChE J.* **18**, 361-371.

Yao, L. S. and Prusa, J. 1989 Melting and Freezing. *Advances in Heat Transfer* **19**, 1-95.

Appendix A

MEASUREMENT OF WAX SURFACE TENSION

The surface tension of candelilla wax (Dataproducts solid ink) was measured at different temperatures with the ring method. The tensiometer (Cenco 70535) was manufactured by Cenco Instrument Corporation. The solid ink, which was developed by Dataproducts Corporation for SI 480 solid ink printers, mainly contains candelilla wax and has a melting point of about 70°C. Figure A.1 shows the apparatus for measuring wax surface tension.

The tensiometer was calibrated before the measurement according to the calibration procedure described in the manual *Operating Instructions* provided by Cenco Instrument Corporation. The platinum ring and the crystal dish were ultrasonically cleaned with a cleaning solution (MICRO) manufactured by International Products Corporation.

The trial measurement of pure distilled water shows that the apparatus works well. The measured apparent surface tension P of pure distilled water at 25°C is 76.7 dyn cm^{-1}. In the operating instruments, the corrected surface tension σ is given by Equation (A.1)

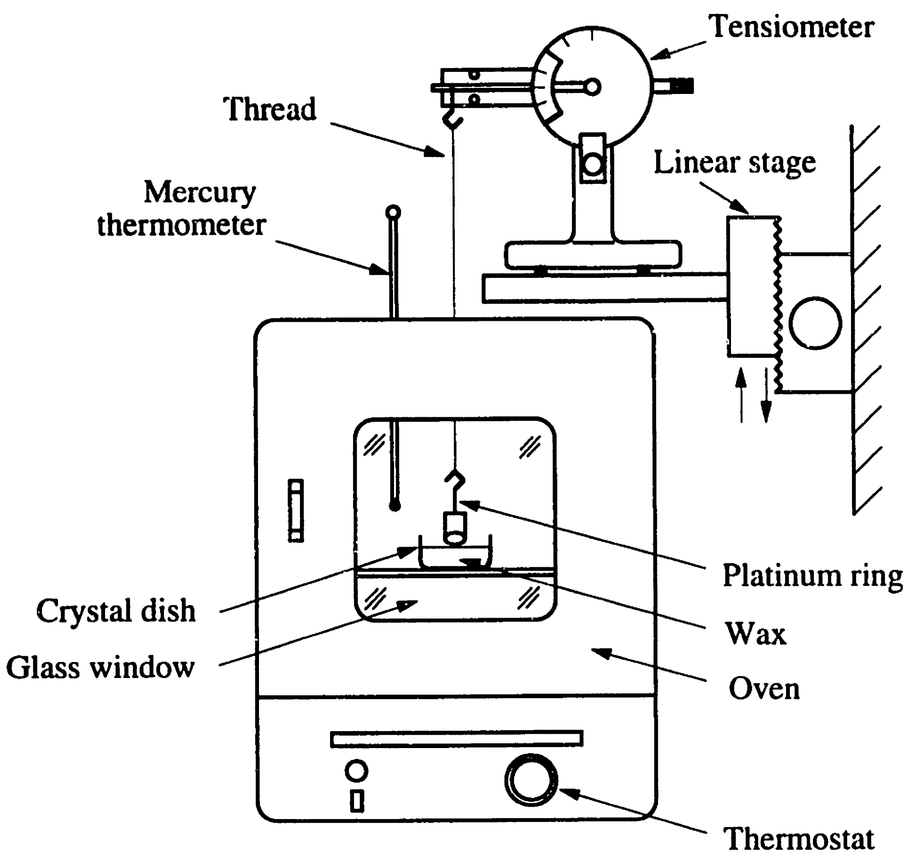

Figure A.1. Apparatus for measuring wax surface tension.

$$\sigma = FP, \tag{A.1}$$

where F is a correction factor which is determined by Equation (A.2) (Zuidema & Waters 1941)

$$(F - a)^2 = \frac{4b}{\pi^2} \frac{1}{R^2} \frac{P}{\rho_l - \rho_u} + C. \tag{A.2}$$

In Equation (A.2), ρ_l and ρ_u are densities of the lower and the upper phases respectively, $a = 0.7250$ and $b = 0.0009075$ are universal constants, $C = 0.04534 - 1.679\ (r/R)$, and R

and r are the radii of the ring and the wire of the ring respectively. A platinum-iridium ring (mean circumference = 6.000 cm, $R/r = 53.7488890$) is used in this case.

From Equation (A.2) we have $F = 0.9375$ for pure distilled water at 25°C, so the corrected surface tension is $\sigma = FP = 71.91$ dyn cm^{-1}. From Adamson (1990), $\sigma = 72.13$ dyn cm^{-1} for water at 25°C.

Before the first measurement, the wax was heated in the oven at 140°C for 90 minutes to allow the system to reach a state of thermal equilibrium. The surface tension of wax was measured at different temperature points by setting the thermostat. There was a period of at least 30 minutes between a new setting of the thermostat and the next measurement to allow the system to reach the thermal equilibrium state again. Table A.1 and Figure A.2 show the results of measurements.

Table A.1. *Measurement results*

T °C	P dyn cm^{-1}	ρ_u (air[a]) kg m^{-3}	ρ_l (wax[b]) kg m^{-3}	F	σ dyn cm^{-1}
138	26.2	0.855	836	0.888575	23.281
132	26.6	0.870	839	0.888824	23.465
126	27.1	0.885	842	0.889617	24.101
120	27.5	0.900	845	0.890057	24.477
115	27.8	0.913	848	0.890349	24.752
105	28.6	0.938	853	0.891258	25.490
94.5	29.4	0.961	858	0.892152	26.229
82.5	30.2	0.993	864	0.892982	26.968

[a] By interpolating the data from Roberson & Crowe (1990).
[b] By interpolating the data from Warth (1956).

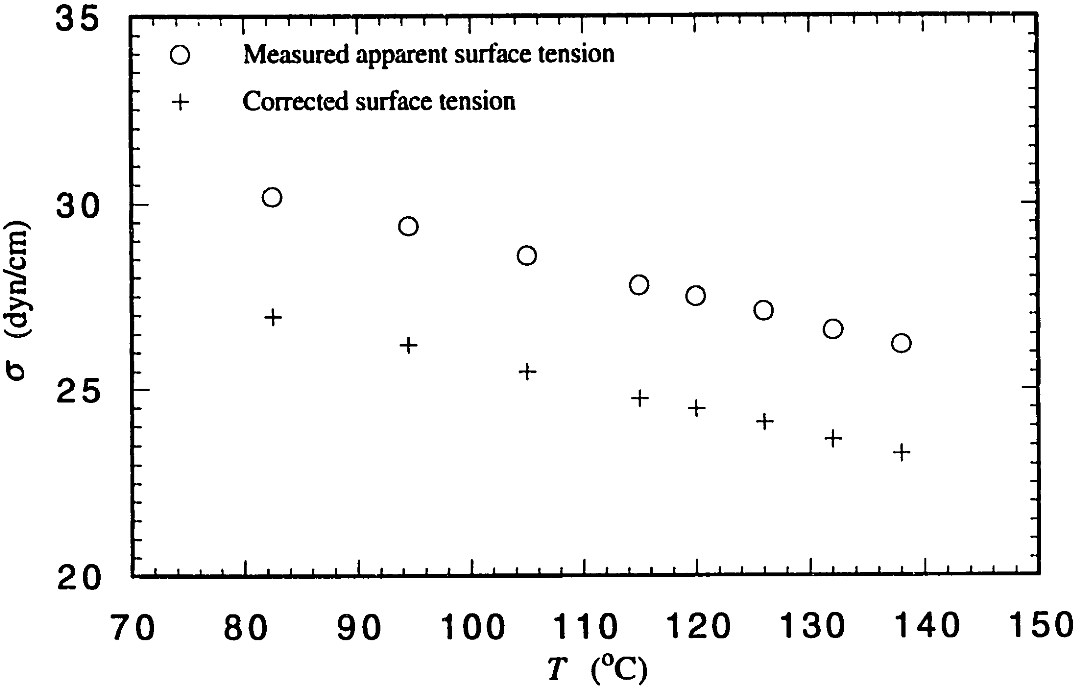

Figure A.2. Measurement results: surface tension σ versus temperature T.

NOMENCLATURE

a	universal constant, $a = 0.7250$
b	universal constant, $b = 0.0009075$
C	constant, $C = 0.04534 - 1.679\ (r/R)$
F	correction factor
P	apparent surface tension
R	radius of the ring

r	radius of the wire of the ring
T	temperature
ρ_l	density of the lower phase
ρ_u	density of the upper phase
σ	surface tension

REFERENCES

Adamson, A. W. 1990 *Physical Chemistry of Surfaces*, 5th ed. New York: Wiley.

Cenco Instruments Corp., Chicago. *Operating Instructions, Cat. Nos. 70535 and 70545 Tensiometers.*

Roberson, J. A., and Crowe, C. T. 1990 *Engineering Fluid Mechanics*, 4th ed. Boston: Houghton Mifflin.

Warth, A. H. 1956 *The Chemistry and Technology of Waxes*, 2nd ed. New York: Reinhold.

Zuidema, H. H. and Waters, G. W. 1941 Ring Method for the Determination of Interfacial Tension. *Ind. and Eng. Chem.* **13**, 312-313.

Appendix B

SPREADING OF LIQUID DROPLETS ON PLANAR SOLID SURFACES

Figure B.1 shows a droplet spreading on a planar solid surface. The droplet is taken to be small enough that the effects of gravity can be neglected.

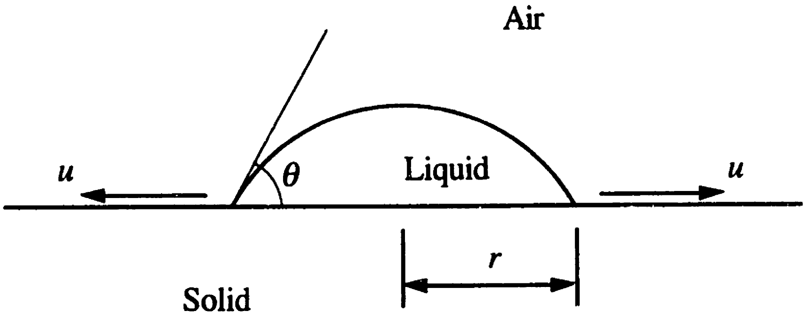

Figure B.1. A cross section of a droplet spreading on a planar solid surface (a macroscopic picture).

Assuming that the spreading droplet takes the shape of a spherical segment, we have

$$\frac{r^3}{V} = \frac{3}{\pi}\frac{\sin\theta(1+\cos\theta)}{(1-\cos\theta)(2+\cos\theta)}, \tag{B.1}$$

$$V = \frac{4}{3}\pi a^3, \tag{B.2}$$

where r is the radius of the wetted area, θ the apparent contact angle, V the constant volume of the spreading droplet, and a the radius of the spherical droplet.

Substitution of Equation (B.2) into Equation (B.1) yields

$$\left(\frac{r}{a}\right)^3 = 4\frac{\sin\theta(1+\cos\theta)}{(1-\cos\theta)(2+\cos\theta)}. \tag{B.3a}$$

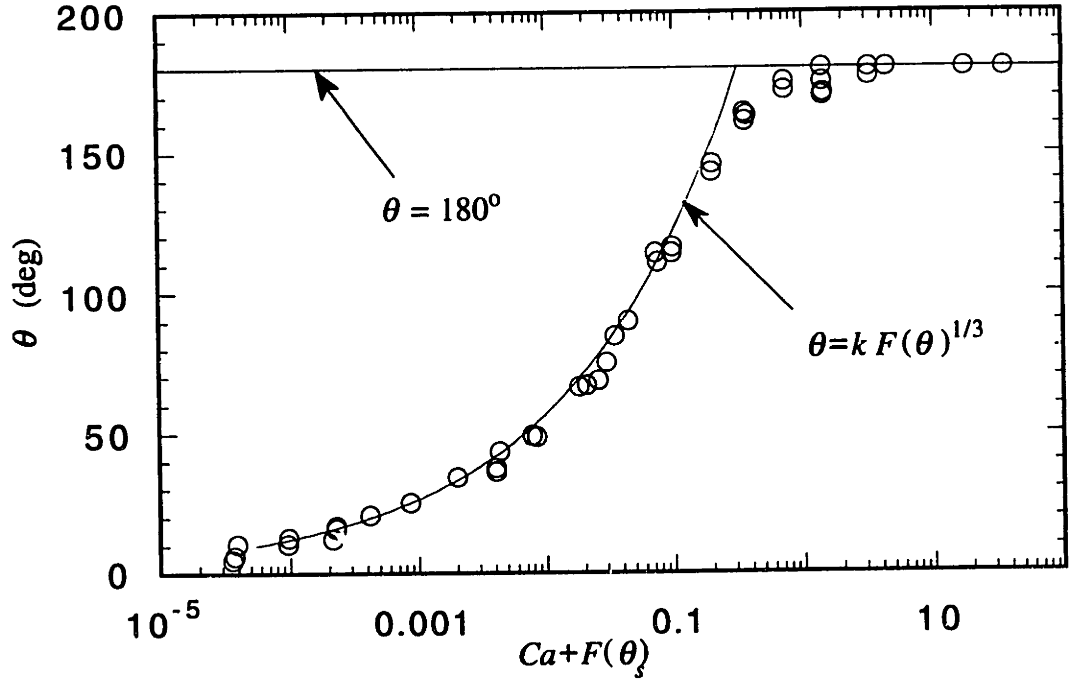

Figure B.2. Effect of flow on the apparent contact angle of an advancing liquid-air interface (Hoffman 1975).

Hoffman (1975) measured the apparent contact angle of an advancing liquid-air interface in a glass capillary. He plotted the apparent contact angle versus capillary number plus a shift factor and obtained a curve which correlated all the data. Figure B.2 shows Hoffman's results.

From Hoffman's results, we can write

$$\begin{aligned} F(\theta) &= Ca + F(\theta_S) \\ &= \frac{\mu u}{\sigma} + F(\theta_S), \end{aligned} \tag{B.4}$$

and at low $F(\theta)$

$$\begin{aligned} \theta &\approx k\, F(\theta)^{1/3} \\ &= k\left(\frac{\mu u}{\sigma} + F(\theta_S)\right)^{1/3}, \end{aligned} \tag{B.5}$$

where θ_S is the static contact angle, k a constant ($k \approx 263.19$ if the unit of θ is degree), $Ca = \mu u/\sigma$ the capillary number, $u = dr/dt$ the spreading velocity, μ the viscosity of the liquid, and σ the surface tension at the air-liquid interface. $F(\theta_S)$ is a shift factor, which is determined only by θ_S and is zero when θ_S is zero.

From Equation (B.5)

$$\frac{\theta^3}{k^3} = \frac{\mu u}{\sigma} + F(\theta_S). \tag{B.6}$$

The spreading velocity u is zero when θ is equal to θ_S, therefore

$$\frac{\theta_s^3}{k^3} = F(\theta_s)$$

and

$$\frac{\theta^3}{k^3} = \frac{\mu u}{\sigma} + \frac{\theta_s^3}{k^3}, \tag{B.7}$$

where $u = \mathrm{d}r/\mathrm{d}t$. Equation (B.7) can be rewritten as

$$k^3 \frac{\mu}{\sigma} \frac{\mathrm{d}r}{\mathrm{d}t} = \theta^3 - \theta_s^3. \tag{B.8a}$$

Now we have

$$\left(\frac{r}{a} \right)^3 = 4 \frac{\sin\theta(1 + \cos\theta)}{(1 - \cos\theta)(2 + \cos\theta)} \tag{B.3a}$$

and

$$k^3 \frac{\mu}{\sigma} \frac{\mathrm{d}r}{\mathrm{d}t} = \theta^3 - \theta_s^3, \tag{B.8a}$$

with the initial conditions: $\theta = \pi$ and $r = 0$ at $t = 0$. Let

$$t^* = \frac{t}{k^3 \frac{\mu}{\sigma} a}$$

and

$$r^* = \frac{r}{a}.$$

Equations (B.3a) and (B.8a) become

$$r^* = \left(4 \frac{\sin\theta(1 + \cos\theta)}{(1 - \cos\theta)(2 + \cos\theta)} \right)^{1/3}, \tag{B.3b}$$

$$\frac{dr^*}{dt^*} = \theta^3 - \theta_s^3, \tag{B.8b}$$

with the initial condition: $\theta = \pi$ and $r^* = 0$ at $t^* = 0$. Differentiating Equation (B.3b) gives $dr^*/dt^* = F(\theta, d\theta/dt^*)$. Using Equation (B.8b) to eliminate dr^*/dt^*, we obtain

$$\frac{d\theta}{dt^*} = -\left(\frac{1 + \cos\theta}{2}\right)^{2/3}\left(\frac{(1 - \cos\theta)(2 + \cos\theta)}{\sin\theta}\right)^{4/3}(\theta^3 - \theta_s^3), \tag{B.9}$$

with the initial conditions: $\theta = \pi$ at $t^* = 0$.

We obtained the apparent contact angle θ as a function of the dimensionless time t^* by solving Equation (B.9) with a fourth-order Runge-Kutta method, and then got the dimensionless velocity $u^*(= dr^*/dt^*)$ and the dimensionless radius of the wetted area r^* from Equation (B.8b) and Equation (B.3b) respectively. Figures B.3, B.4, and B.5 show these results.

The dimensionless spreading velocity u^* at large θ is much greater than that at small θ and approaches zero as θ approaches θ_s. In physical terms, the droplet spreads rapidly during the early stages, and then very slowly during the later stages. For the case of $\theta_s = 0$, the time for a droplet to reach the static state ($\theta = \theta_s = 0$) approaches infinity.

Figure B6 and Table B1 give the apparent contact angle θ at dimensionless characteristic time t_c^* for various θ_s. For a given θ_s, the characteristic time t_c^* is taken as the time for a droplet with zero θ_s to spread from $\theta = \pi$ to the given θ_s. For the case of zero θ_s, t_c^* is infinite. The differences between θ_s and θ at t_c^* decrease as the values of θ_s decrease.

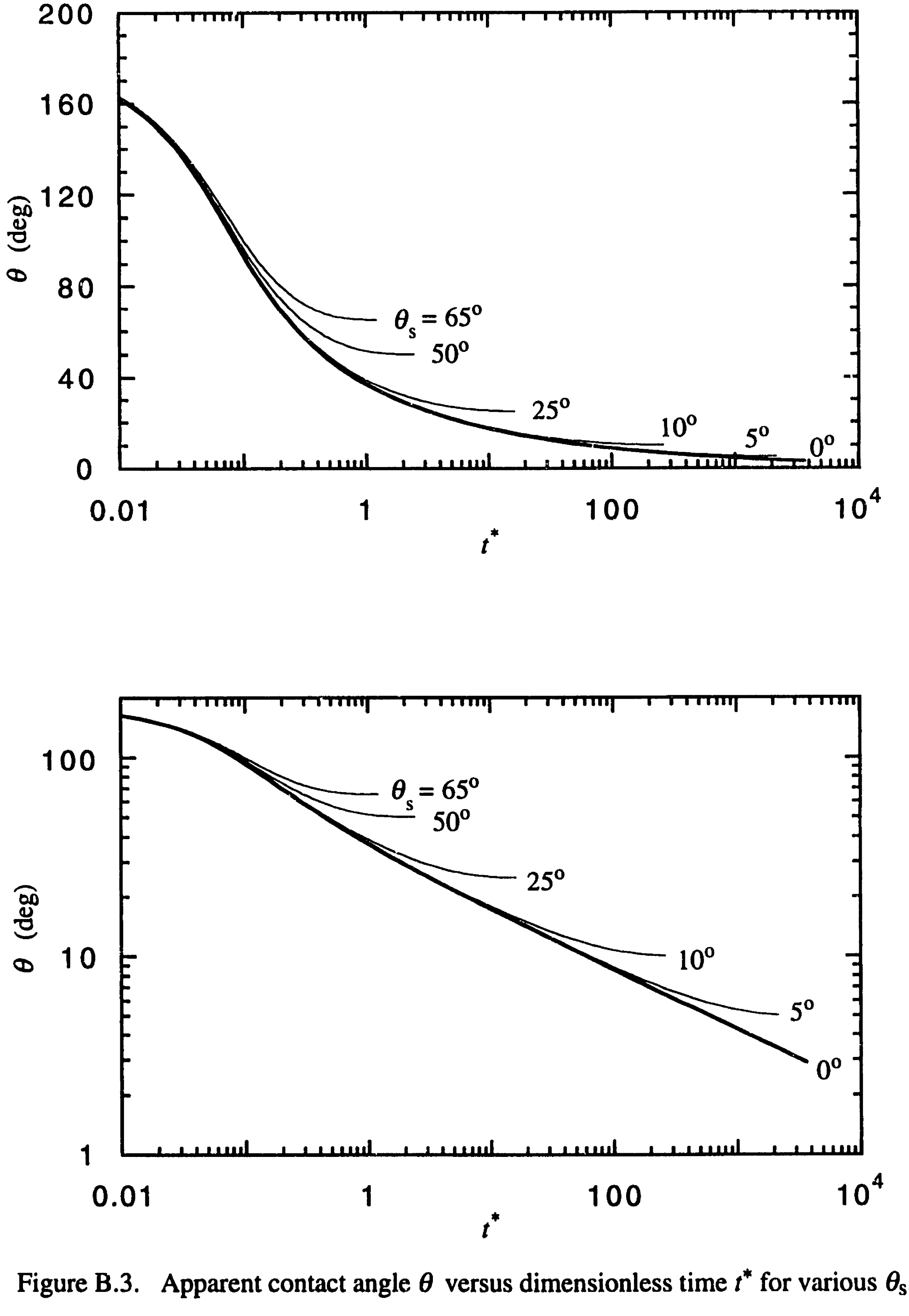

Figure B.3. Apparent contact angle θ versus dimensionless time t^* for various θ_S.

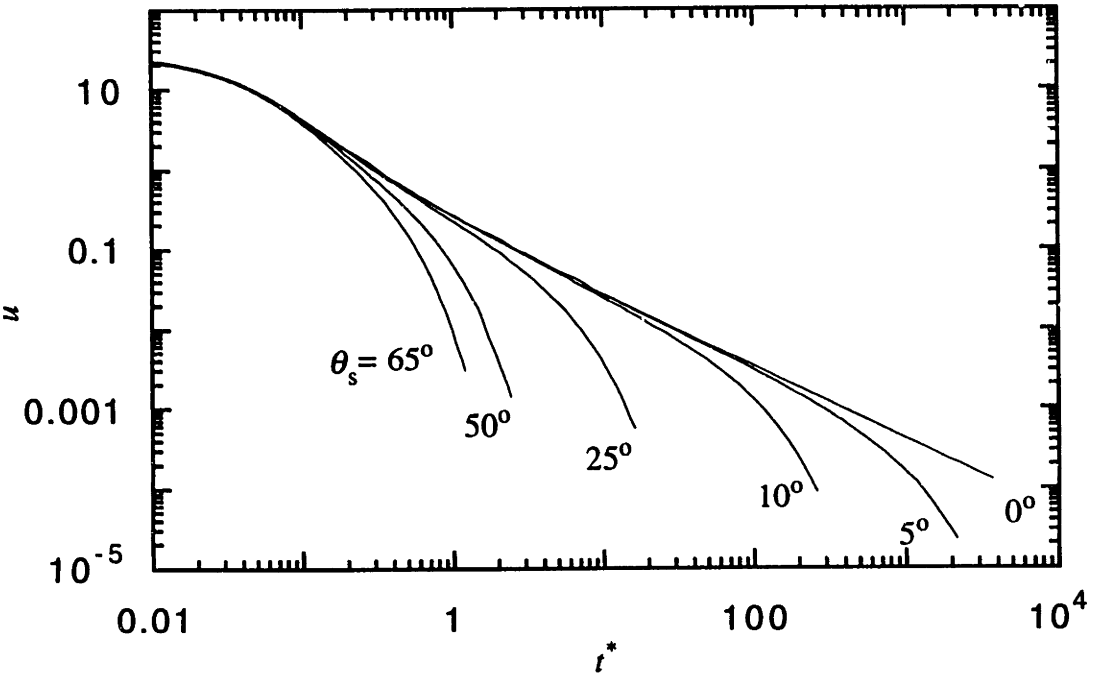

Figure B.4. Dimensionless velocity u^* versus dimensionless time t^* for various θ_S.

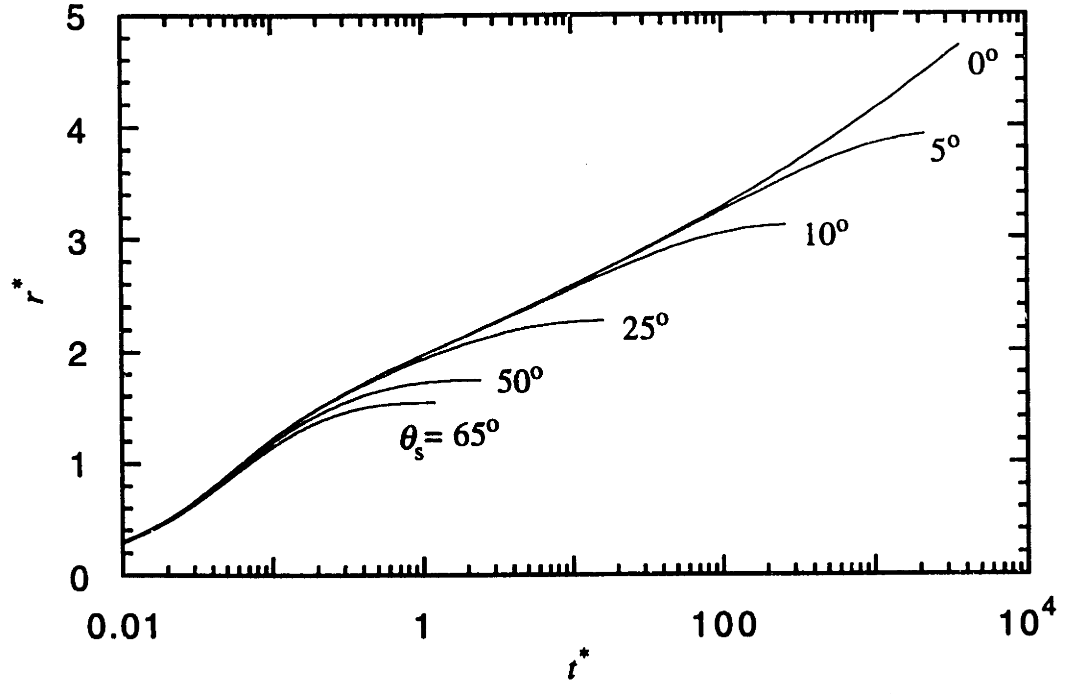

Figure B.5. Dimensionless radius r^* versus dimensionless time t^* for various θ_S.

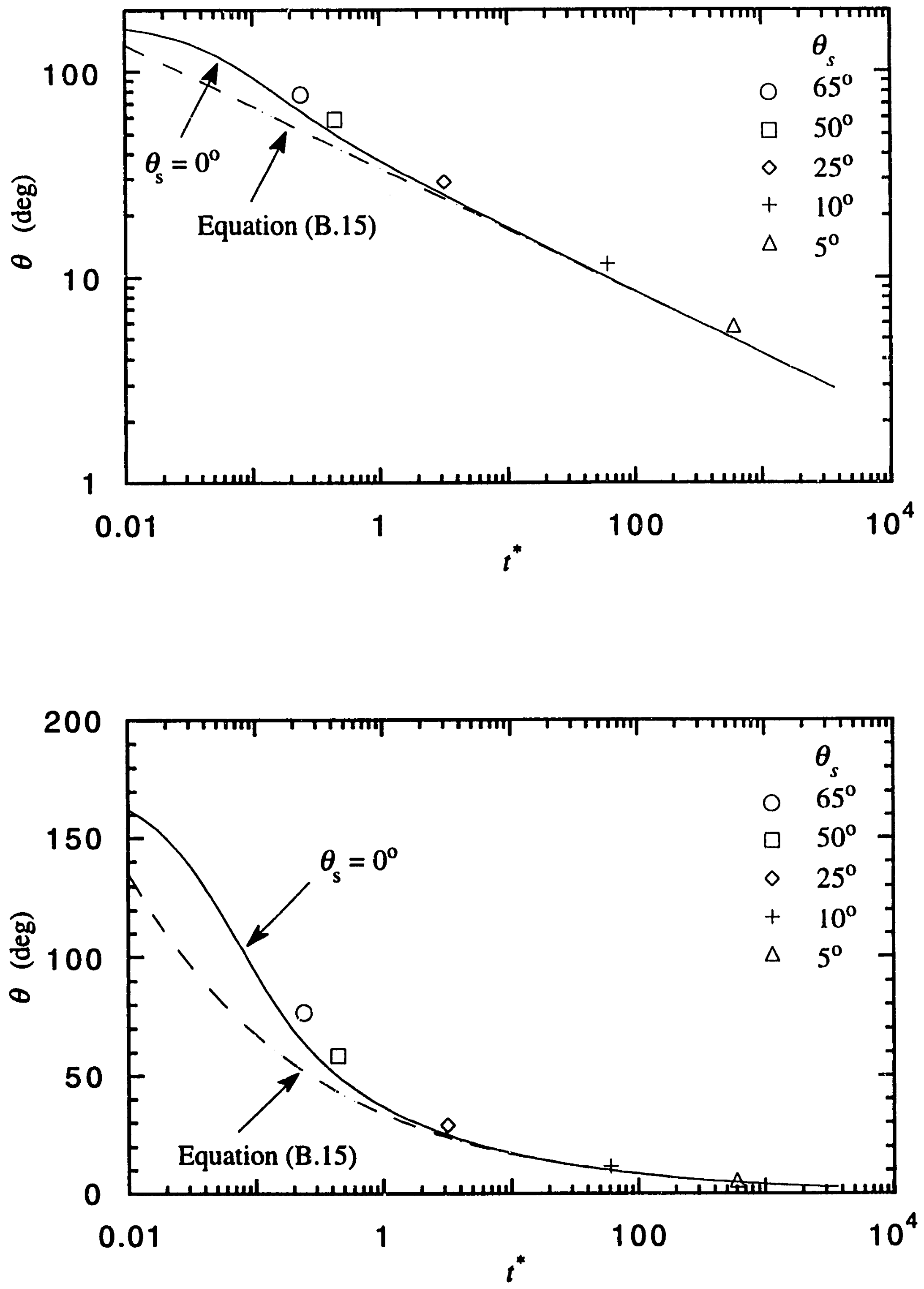

Figure B.6. Apparent contact angle θ at dimensionless characteristic time t^* for various θ_s.

Table B.1. *Apparent contact angle θ at dimensionless characteristic time $t_c{}^*$ for various θ_s*

θ_s (deg)	$t_c{}^*$	$\theta(t_c{}^*)$ (deg)	$\theta_s/\theta(t_c{}^*)$
0	∞	0	—
5	595.963	5.798	0.862
10	60.093	11.600	0.862
25	3.174	29.061	0.860
50	0.446	58.656	0.852
65	0.239	76.982	0.844

As mentioned above, the droplet spreads rapidly at the early stages, and then very slowly as time progresses. Consequently, we may consider only the late stages of spreading and assume that θ is small to get the relation between θ (or r) and the spreading time t for the case of zero θ_s.

For $\theta << 1$, $\sin\theta \approx \theta$ and $\cos\theta \approx 1 - \frac{\theta^2}{2}$. From Equation (B.3a), we have

$$\left(\frac{r}{a}\right)^3 \approx \frac{8}{\theta}\,\frac{\left(2 - \frac{\theta^2}{2}\right)}{\left(3 - \frac{\theta^2}{2}\right)} \approx \frac{16}{3\theta},$$

$$\theta \approx \frac{16}{3}\left(\frac{a}{r}\right)^3. \tag{B.10}$$

Substituting Equation (B.10) into Equation (B.8a) and noticing that θ_s is equal to zero, we get

$$\frac{(16/3)^3}{k^3} a^9 \frac{\sigma}{\mu} \mathrm{d}t \approx r^9 \, \mathrm{d}r. \tag{B.11}$$

Integrating Equation (B.11) gives

$$r \approx \left(\frac{10 * 16^3 \, a^9 \, \sigma}{3^3 \, k^3 \mu} \right)^{1/10} t^{1/10} \tag{B.12}$$

and

$$r^* \approx \left(\frac{10 * 16^3}{3^3} \right) t^{*1/10}. \tag{B.12a}$$

Equation (B.12) can be rewritten as

$$r \approx \left(\frac{10 * 16^3}{3^3 k^3} \right) \left(\frac{3}{4\pi} \right)^{3/10} V^{3/10} \left(\frac{\sigma \mathrm{t}}{\mu} \right)^{1/10}. \tag{B.12b}$$

Equation (B.12b) essentially has the same form as that given by de Gennes (1985).

From Equation (B.9), we have

$$\begin{aligned} \frac{\mathrm{d}\theta}{\mathrm{d}t^*} &\approx - \left(\frac{2 - \frac{\theta^2}{2}}{2} \right)^{2/3} \left(\frac{\frac{\theta^2}{2} (3 - \frac{\theta^2}{2})}{\theta} \right)^{4/3} \theta^3 \\ &\approx - \left(\frac{3}{2} \right)^{4/3} \theta^{4/3} \, \theta^3, \end{aligned}$$

$$dt^* \approx -\left(\frac{2}{3}\right)^{4/3} \theta^{-13/3}\, d\theta. \qquad \text{(B.13)}$$

Integrating Equation (B.13) gives

$$t^* \approx -\left(\frac{2}{3}\right)^{4/3} \int_{\theta_o}^{\theta(t^*)} \theta^{-13/3}\, d\theta$$

$$= \left(\frac{2}{3}\right)^{4/3} \left(\frac{3}{10}\right) (\theta^{-10/3} - \theta_o^{-10/3}).$$

For $\theta_o >> \theta$,

$$t^* \approx \left(\frac{2}{3}\right)^{4/3} \left(\frac{3}{10}\right) \theta^{-10/3} \qquad \text{(B.14)}$$

or

$$\theta \approx \left(\frac{\left(\frac{2}{3}\right)^{4/3} \left(\frac{3}{10}\right)}{t^*} \right)^{3/10}. \qquad \text{(B.15)}$$

From numerical results,

$t^* = 3260$ for $\theta = 3^{o}$

and from Equation (B.14),

$t^* = 3253$ for $\theta = 3^{o}$.

NOMENCLATURE

a	radius of the spherical droplet
Ca	capillary number, $Ca = \mu u/\sigma$
$F(\theta_s)$	shift factor
k	constant defined by Equation (B.5)
r	radius of the wetted area
r^*	dimensionless radius of the wetted area, $r^* = r/a$
t	time
t^*	dimensionless time, $t^* = t/(\mathrm{k}^3(\mu/\sigma)a)$
$t_c{}^*$	dimensionless characteristic time
u	spreading velocity, $u = \mathrm{d}r/\mathrm{d}t$
u^*	dimensionless spreading velocity, $u^* = \mathrm{d}r^*/\mathrm{d}t^*$
V	constant volume of the spreading droplet, $V = \frac{4}{3}\pi a^3$
θ	apparent contact angle
θ_s	static contact angle
μ	viscosity of the liquid
σ	surface tension at the gas-liquid interface

REFERENCES

de Gennes, P. G. 1985 Wetting: statics and dynamics. *Rev. Mod. Phys.*, **57**, No. 3, 827-863.

Hoffman, R. L. 1975 A Study of the Advancing Interface. I. Interface Shape in Liquid-Gas Systems. *J. Colloid Interface Sci.* **50**, No. 2, 228-241.

Appendix C

DATA

Table C.1. *Data for Figure 4.7*

The relationship between a pillar's angle ϕ and the horizontal center-to-center deposition spacing w, for $We < 6$.

	w (μm)	w/h	ϕ (deg)
Candelilla wax $T_\mathrm{o} = 90^\circ\mathrm{C}$ $T_\mathrm{a} = 36^\circ\mathrm{C}$ $h = 27\ \mu\mathrm{m}$	20	0.741	41.0
	20	0.741	38.0
	25	0.926	14.0
Microcrystalline wax $T_\mathrm{o} = 110^\circ\mathrm{C}$ $T_\mathrm{a} = 50^\circ\mathrm{C}$ $h = 28\ \mu\mathrm{m}$	10	0.357	68.5
	10	0.357	67.0
	15	0.536	54.5
	15	0.536	54.0
	20	0.714	41.5
	25	0.893	27.5

Table C.2. *Data for Figure 4.9*

Column radius R in the continuous solidification mode.

	Microcrystalline wax $T_o = 120^oC$ $T_a = 46^oC$	Candelilla wax $T_o = 90^oC$ $T_a = 33^oC$	Candelilla wax $T_o = 120^oC$ $T_a = 50^oC$
f (Hz)	R (mm)	R (mm)	R (mm)
100	0.067	0.062	0.119
200	0.098	0.088	0.228
400	0.150	0.134	0.362
500	0.186	0.166	0.445
750	0.228	-	-
1000	0.279	0.264	0.569

Table C.3. *Data for Figure 4.15*

Sweep deposition at high speed and high target temperature. Candelilla wax on plexiglas, $2a = 50.5$ µm, $U = 0.293$ m s^{-1}, $T_o = 90^oC$, $T_a = 58^oC$.

f (kHz)	$f(2a)/U$	W (µm)	$W/(2a)$
3.54	0.61	73.4	1.45
3.64	0.63	73.4	1.45
4.00	0.69	75.5	1.50
5.00	0.86	80.9	1.60
7.35	1.27	102.5	2.03
10.00	1.72	113.3	2.24
12.00	2.07	124.1	2.46
15.15	2.61	142.5	2.82
18.18	3.13	148.9	2.95

Table C.4. *Data for Figure 4.16*

Sweep deposition, low target temperature. Candelilla wax on plexiglas, $2a = 50.5\ \mu\text{m}$, $T_o = 90^{o}\text{C}$, $T_a = 45^{o}\text{C}$.

U (m s^{-1})	f (kHz)	$f(2a)/U$	W (μm)	$W/(2a)$
0.0275	0.470	0.86	63.2	1.25
	0.690	1.27	68.4	1.35
	0.935	1.72	66.3	1.31
	1.128	2.07	66.3	1.31
0.2930	5.000	0.86	63.2	1.25
	7.350	1.27	73.7	1.46
	10.000	1.72	86.3	1.71
	12.000	2.07	87.4	1.73

Table C.5. *Data for Figures 5.3 and 5.4*

Candelilla wax, $T_o = 90^{o}\text{C}$, $f = 10$ kHz, $2a = 50.5\ \mu\text{m}$.

N	D_{meas} (μm)		D_{meas}/D_{sphere}		θ (deg)	
	34°C	60°C	34°C	60°C	34°C	60°C
1	75.0	100.0	1.485	1.980	70.0	36.7
3	87.5	145.0	1.201	1.991	95.9	36.2
6	127.5	175.0	1.389	1.907	78.3	40.4
10	150.0	210.0	1.379	1.930	79.3	39.2
15	175.0	240.0	1.405	1.927	76.9	39.3
20	192.5	265.0	1.404	1.933	77.0	39.0
30	202.5	312.5	1.291	1.992	87.2	36.1
50	215.0	362.5	1.156	1.949	101.5	38.2
75	235.0	415.0	1.104	1.949	109.8	38.2
100	245.0	455.0	1.045	1.941	124.0	38.6
125	265.0	495.0	1.050	1.960	122.6	37.6
150	275.0	535.0	1.025	1.994	132.4	36.0
175	290.0	565.0	1.027	2.000	131.5	35.7
200	300.0	587.5	1.016	1.989	137.8	36.2
225	315.0	-	1.026	-	132.0	-
250	327.5	-	1.030	-	130.2	-
300	342.5	-	1.013	-	140.0	-
350	360.0	-	1.012	-	141.2	-
400	375.0	-	1.008	-	145.0	-
500	402.5	-	1.004	-	150.2	-
600	430.0	-	1.010	-	143.1	-
700	450.0	-	1.004	-	151.4	-
800	470.0	-	1.003	-	153.8	-
900	490.0	-	1.005	-	148.9	-
1000	510.0	-	1.010	-	142.7	-

Table C.6. *Data for Figures 5.9 and 5.10*

Candelilla wax, $T_0 = 90^{o}$C, f = 15 kHz, $2a$ = 53.25 μm.

N	D_{meas} (μm)		D_{meas}/D_{sphere}		θ (deg)	
	33°C	60°C	33°C	60°C	33°C	60°C
1	70.0	110.0	1.315	2.066	85.0	32.8
3	92.5	150.0	1.204	1.953	95.6	38.0
6	122.5	195.0	1.266	2.015	89.4	35.0
10	127.5	225.0	1.111	1.961	108.4	37.6
15	150.0	250.0	1.142	1.904	103.4	40.6
20	187.5	270.0	1.297	1.868	86.6	42.6
30	225.0	325.0	1.360	1.964	81.0	37.4
50	250.0	390.0	1.274	1.988	88.7	36.3
75	255.0	440.0	1.136	1.960	104.4	37.7
100	275.0	487.5	1.113	1.972	108.2	37.0
125	300.0	525.0	1.127	1.972	105.8	37.1
150	340.0	560.0	1.202	1.979	95.9	36.7
175	310.0	600.0	1.041	2.014	125.6	35.0
200	330.0	615.0	1.060	1.975	119.6	36.9
225	335.0	640.0	1.034	1.976	128.0	36.9
250	340.0	652.5	1.014	1.945	139.5	38.4
300	360.0	702.5	1.010	1.971	142.7	37.1
350	385.0	740.0	1.026	1.972	131.8	37.1
400	395.0	792.5	1.007	2.020	146.3	34.8
500	425.0	837.5	1.006	1.982	148.0	36.6
600	450.0	890.0	1.002	1.982	155.6	36.6
700	520.0	945.0	1.100	1.999	110.5	35.8
800	495.0	1000.0	1.001	2.023	157.7	34.7
900	510.0	1052.5	0.992	2.047	179.8	33.6
1000	535.0	1040.0	1.005	1.953	149.4	38.0
1200	570.0	1112.5	1.007	1.966	145.6	37.4
1400	595.0	1162.5	1.000	1.952	179.8	38.1
1600	630.0	1170.0	1.012	1.879	141.2	42.0
1800	652,5	1220.0	1.007	1.883	145.6	41.7
2000	677.5	1245.0	1.010	1.856	142.8	43.3
2500	722.5	1307.5	1.000	1.809	179.8	46.0
3000	767.5	1332.5	0.999	1.735	179.8	50.8

Table C.7. *Data for Figure 5.11*

Candelilla wax, $T_o = 115^oC$, $T_t = 60^oC$, $f = 10$ kHz, $2a = 57.5$ µm.

N	D_{meas} (µm)	θ (deg)
1	115.0	35.7
3	167.5	34.8
6	210.0	35.3
10	250.0	34.9
15	285.0	35.3
20	310.0	36.4
30	362.5	34.4
50	440.0	32.3
75	502.5	32.5
100	550.0	33.0
125	597.5	32.2
150	642.5	31.2
175	647.5	35.1
200	700.0	32.1
225	725.0	32.5
250	770.0	30.3
300	827.5	29.4
350	870.0	29.5
400	892.5	31.1
500	955.0	31.6
600	1017.5	31.4
700	1070.0	31.5
800	1130.0	30.7
900	1165.0	31.4
1000	1220.0	30.5
1200	1315.0	29.3
1400	1342.5	31.9
1600	1377.5	33.5
1800	1460.0	31.9
2000	1502.5	32.4
2500	1632.5	31.7
3000	1697.5	33.6
4000	1905.0	31.9
5000	1980.0	35.1
6000	2025.0	38.8
8000	2200.0	40.1

Table C.8. *Data for Figures 5.12, 5.13, and 5.14*

Candelilla wax, T_o = 115°C, f = 10 kHz, $2a$ = 57.5 μm.

	D_{meas} (μm)					
N	T_t = 36°C	T_t = 45°C	T_t = 50°C	T_t = 55°C	T_t = 60°C	T_t = 66°C
50	355.0	350.0	370.0	390.0	440.0	560.0
100	380.0	410.0	435.0	490.0	550.0	742.5
200	505.0	500.0	512.5	610.0	700.0	-
500	672.5	650.0	635.0	805.0	955.0	1270.0
1000	-	772.5	-	1000.0	1220.0	1485.0
2000	-	950.0	-	1245.0	1502.5	1820.0

	D_{meas}/D_{meas}					
N	T_t = 36°C	T_t = 45°C	T_t = 50°C	T_t = 55°C	T_t = 60°C	T_t = 66°C
50	1.676	1.652	1.747	1.841	2.077	2.644
100	1.424	1.536	1.630	1.836	2.061	2.782
200	1.502	1.487	1.524	1.814	2.082	-
500	1.474	1.424	1.391	1.764	2.093	2.783
1000	-	1.344	-	1.739	2.122	2.583
2000	-	1.311	-	1.719	2.074	2.512

	θ (deg)					
N	T_t = 36°C	T_t = 45°C	T_t = 50°C	T_t = 55°C	T_t = 60°C	T_t = 66°C
50	54.9	56.7	50.0	44.1	32.3	16.3
100	75.3	65.7	58.3	44.4	33.0	14.0
200	68.6	69.8	66.7	45.7	32.1	-
500	71.0	75.2	78.1	48.9	31.6	14.0
1000	-	82.4	-	50.5	30.5	17.5
2000	-	85.3	-	51.9	32.4	18.9

Table C.9. *Data for Figure 5.15*

Microcrystalline wax, T_0 = 115°C , f = 10 kHz, $2a$ = 48 µm.

	θ (deg)			
T_t (°C)	N = 10	N = 100	N = 200	N = 400
80.5	23.8	25.4	26.1	29.4
75.0	30.3	33.8	33.5	33.5
70.0	41.6	49.8	-	-
60.0	50.4	57.7	-	-

Table C.10. *Data for Figure 5.21*

Candelilla wax, T_0 = 90°C, f = 10 kHz, $2a$ = 50.5 µm.

	D_{meas} (µm)					
	Thin gold film			Glass surface		
N	T_t = 36°C	T_t = 44°C	T_t = 60°C	T_t = 36°C	T_t = 44°C	T_t = 60°C
10	160.0	185.0	272.5	155.0	175.0	240.0
20	200.0	235.0	342.5	202.5	230.0	300.0
50	215.0	305.0	460.0	215.0	305.0	395.0

	θ (deg)					
	Thin gold film			Glass surface		
N	T_t = 36°C	T_t = 44°C	T_t = 60°C	T_t = 36°C	T_t = 44°C	T_t = 60°C
10	71.2	53.2	19.1	75.2	60.0	27.4
20	72.2	52.2	19.2	70.6	54.8	28.0
50	101.5	57.6	19.8	101.5	57.6	30.4